

**The Pennsylvania State University**

**The Graduate School**

**College of Engineering**

**MODELING, OPTIMAL DESIGN, SHAPE ESTIMATION AND WORKSPACE**

**ANALYSIS OF SOFT ROBOTIC MANIPULATORS**

A Dissertation in

Mechanical Engineering

by

Deepak Trivedi

© 2010 Deepak Trivedi

Submitted in Partial Fulfillment

of the Requirements

for the Degree of

Doctor of Philosophy

August 2010

The dissertation of Deepak Trivedi was reviewed and approved\* by the following:

Christopher D. Rahn  
Professor of Mechanical Engineering  
Dissertation Advisor  
Chair of Committee

Mary Frecker  
Professor of Mechanical Engineering

George A. Lesieutre  
Professor of Aerospace Engineering

Eric Mockensturm  
Professor of Mechanical Engineering

Karen A. Thole  
Professor of Mechanical Engineering  
Head of the Department of Mechanical and Nuclear Engineering

\*Signatures are on file in the Graduate School.

# Abstract

Traditional robot manipulators have rigid links and can manipulate objects only using their specialized end effectors. They encounter difficulties operating in unstructured and highly congested environments. Several animal organs such as elephant trunks, mammal and lizard tongues, and octopus arms address this problem by not having any rigid components. These muscular hydrostats are composed of natural muscles and connective tissue. Animal muscle is soft material with large strain, moderate stress, high efficiency, fast response time, high power/weight ratio and long lifetime, capabilities that conventional actuators do not possess. Researchers have been inspired by biology to design, build and test soft robotic manipulators based on electro-active polymers and pneumatic muscles. The unusual compliance and redundant degrees of freedom of these manipulators are essential for applications requiring delicate manipulation in cluttered and/or unstructured environments. With no hard parts, these robots can squeeze through tiny spaces and manipulate objects of widely-varying sizes. A key challenge in the design and control of soft robotic manipulators is the development of accurate models that predict the shape of the arm given the loading and actuation inputs. Existing models make

several assumptions about the material properties, loading conditions and kinematics of these manipulators and are not sufficiently accurate under in real world situations. The first contribution of this thesis is the development of geometrically exact models that describe the dynamics of soft robotic manipulators that can be used in design, sensing, stability analysis, and control. The manipulator is modeled using Cosserat rod theory and takes into account the effect of finite shear, curvature and extension, and material nonlinearities. The model is validated on the OctArm V manipulator. Parametric studies are done with the model to gain an understanding of the mechanics of soft robotic manipulators, providing insight into the optimal design of pneumatic and hydraulic soft manipulators. Theoretically, soft robots have infinite degrees of freedom (dof), but the number of sensors and actuators are limited. This complicates shape estimation and control of soft robotic manipulators. The second contribution of this thesis is the development of three novel methods of shape estimation for soft robotic manipulators based on the geometrically exact model. The first method uses load cells mounted at the base of the manipulator and the second method makes use of cable encoders running through the length of the manipulator. The third method uses inclinometers mounted at the end of each section of the manipulator. Using simulation and experiments these methods are compared for the accuracy of endpoint position estimation for unloaded and loaded OctArm VI.

OctArm-type soft robotic manipulators are complex and difficult to design and fabricate. The third major contribution of this thesis is a simpler, cost effective design for a pneumatic air muscle based soft robotic manipulator in which the actuators for the distal section extend from the base to the tip of the arm, thereby simplifying the pneumatic design and eliminating the need for complex manifolds. We compare the workspace and

dexterity of this new continuous tube design with the OctArm manipulator and conclude that although the two designs have comparable workspace area, the OctArm workspace has better dexterity characteristics.

# Table of Contents

<b>List of Figures</b>	<b>ix</b>
<b>List of Tables</b>	<b>xiv</b>
<b>Acknowledgments</b>	<b>xv</b>
<b>Chapter 1</b>	
<b>Introduction</b>	<b>1</b>
1.1 Biological Inspiration . . . . .	6
1.1.1 Hydrostatic Skeletons and Muscular Hydrostats . . . . .	6
1.1.2 Soft active plant structures . . . . .	12
1.2 State of the Art in Soft Robotics . . . . .	13
1.2.1 Hard robots with soft capabilities . . . . .	13
1.2.2 Soft EAP Robots . . . . .	14
1.2.3 Soft PAM Robots . . . . .	18
1.2.4 OctArm VI . . . . .	19
1.2.5 Modeling . . . . .	23
1.2.6 Control . . . . .	26
1.2.7 Path Planning . . . . .	30
1.3 Challenges . . . . .	33
1.4 Problem statement and research objective . . . . .	36
1.5 Organization of this Thesis . . . . .	37
<b>Chapter 2</b>	
<b>Modeling of Soft Manipulators</b>	<b>39</b>
2.1 Previous research . . . . .	40
2.1.1 Soft Actuator modeling . . . . .	40

2.1.2	Manipulator modeling	42
2.2	Soft actuator model	44
2.3	Manipulator Model	47
2.3.1	Manipulator kinematics	47
2.3.1.1	Planar case	49
2.3.2	Manipulator dynamics	49
2.3.2.1	Planar case	54
2.4	Experimental validation	56
2.5	Conclusions	59
<b>Chapter 3</b>		
	<b>Model-based design optimization</b>	<b>62</b>
3.1	Dexterity Template	63
3.2	Problem formulation	65
3.3	Optimization Method	66
3.4	Optimization Test Cases	68
3.4.1	Fixed Aspect Ratio Case	68
3.4.2	Fixed Tube Diameter	69
3.4.3	Base Diameter Ratio	71
3.4.4	Effect of number of sections	72
3.4.5	Effect of tube stiffness	73
3.5	Conclusions	74
<b>Chapter 4</b>		
	<b>Model-based shape estimation</b>	<b>76</b>
4.1	Introduction	76
4.2	Shape Estimation Techniques	78
4.2.1	Shape Estimation using Load Cells	79
4.2.2	Shape Estimation using Encoders	82
4.2.3	Shape Estimation using Inclinometers	87
4.3	Simulation results	89
4.4	Experimental validation	93
4.5	Conclusions	96
<b>Chapter 5</b>		
	<b>Dexterity and Workspace Analysis</b>	<b>98</b>
5.1	Introduction	98
5.1.1	Manipulator mechanics	101
5.2	Manipulability Analysis	105
5.3	Results	105

5.3.1	Workspace . . . . .	105
5.3.2	Dexterity . . . . .	107
5.4	Conclusions . . . . .	108
<b>Chapter 6</b>		
	<b>Conclusions</b>	<b>112</b>
6.1	Future Work . . . . .	114
<b>Appendix A</b>		
	<b>Matlab code</b>	<b>116</b>
A.1	Actuator model . . . . .	116
A.2	Spatial model . . . . .	117
A.2.1	Main script . . . . .	117
A.2.2	Differential equations . . . . .	119
A.2.3	Boundary conditions . . . . .	119
A.3	Planar model . . . . .	120
A.3.1	Main script . . . . .	120
A.3.2	Differential equations . . . . .	120
A.3.3	Boundary conditions . . . . .	121
<b>Appendix B</b>		
	<b>Test cases</b>	<b>122</b>
B.1	Test case 1: Fixed overall diameter . . . . .	122
B.2	Test case 2: Fixed tube diameter . . . . .	123
B.3	Test case 4: Fixed gripping radius . . . . .	123
B.4	Test case 5: Compromised dexterity . . . . .	124
<b>Appendix C</b>		
	<b>Constants</b>	<b>128</b>
<b>Bibliography</b>		<b>132</b>

# List of Figures

1.1	Capabilities of hard and soft robots. . . . .	2
1.2	Gravitational loading on a soft robot manipulator causes downward deflection (a), actuators bend the structure upward (b) and net displacement has zero tip position but nonzero shape (c). . . . .	6
1.3	Examples of hydroskeletons and muscular hydrostats: (a) tube feet in starfish, (b) octopus arms, (c) colonial anemone, (d) mammalian tongue, (e) squid, (f) elephant trunk, (g) echinoid, (h) <i>Illex illecebrosus</i> (i) inchworm, and (j) snail feet. . . . .	9
1.4	Diagram of the arm of <i>Octopus</i> showing three-dimensional arrangement of muscle fibers and connective tissue fibers. AN, Axial nerve cord; AR, artery; CM, circumferential muscle layer; CT, connective tissue; DCT, dermal connective tissue; EP, epidermis; IN, intramuscular nerve; LM, longitudinal muscle fibers; OME; external oblique muscle layer; OMI, internal oblique muscle layer; OMM, median oblique muscle layer; SU, sucker; TM, transverse muscle fibers; TR, trabeculae; V, vein. . . . .	11
1.5	A schematic of open (a) and closed (b) stomata in plant cells caused by osmotic pressurization. . . . .	12
1.6	Elephant trunk manipulator . . . . .	15
1.7	A starfish gel robot that turns over [1]. . . . .	17
1.8	Pneumatic Air Muscle actuators with a mesh angle of less than $54^{\circ}44'$ contract on pressurization (left), with a mesh angle of $54^{\circ}44'$ neither extend or contract (middle), and of greater than $54^{\circ}44'$ extend on pressurization (right). . . . .	17
1.9	OctArm VI: (a) Semi-transparent 3D view of arm; (b) Close-up photograph of base; (c) Close-up, semi-transparent view of first section; (d) Photograph of complete arm [2]. . . . .	20
1.10	OctArm VI mounted on a mobile base (TALON), reaching around a ball. . . . .	21

1.11	Soft robotic manipulator modeled using the Cosserat rod approach, with the backbone position ( $\mathbf{r}$ ) and orientation ( $\mathbf{d}_1, \mathbf{d}_2, \mathbf{d}_3$ ) parametrized by a single variable $s$ . The manipulator is acted upon by distributed force ( $\mathbf{f}$ ) and discrete forces ( $\mathbf{F}$ ) and moments ( $\mathbf{M}$ ).	24
1.12	Body/Caudal fin propulsion (BCF) modes used for swimming robots.	28
1.13	Path planning for reaching a cancer in the small intestine from the oral cavity.	31
2.1	OctArm V in a maximally curved configuration.	40
2.2	Extensor air muscle actuators extend when pressurized as the wind angle $\alpha$ approaches $54^\circ 44'$ from above.	41
2.3	Cross-sectional view of six and three extensor manipulator sections showing three independent control channels (blue, red, and yellow).	54
2.4	Comparison of experimental (solid) and theoretical (dash-dotted) extension of pneumatic air muscles with applied pressure for (a) $A_t/A = 0.373$ , $\alpha = 65^\circ$ (O), $A_t/A = 0.195$ , $\alpha = 71^\circ$ ( $\Delta$ ); (b) $A_t/A = 1.126$ , $\alpha = 78^\circ$ (O), $A_t/A = 0.682$ , $\alpha = 76^\circ$ ( $\Delta$ ).	58
2.5	Experimental (solid) and constant curvature model (dotted), infinite shear modulus model (dash-dotted), and full order model (dashed) backbone curves for horizontal (left) and vertical (right) base orientations: (a) good, (b) fair, and (c) poor agreement between full order model and experiment.	59
2.6	Average tip position error between models and experiments (64 test cases) versus actuation pressure in: (a) vertical and (b) horizontal base orientation for constant curvature ( $\Delta$ ), infinite shear modulus (O) and full order ( $\square$ ) models.	60
2.7	OctArm V workspace with self-weight (main), without loading (top inset), and with self weight and a 0.25 kg payload (bottom inset) in vertical base orientation.	60
2.8	OctArm V workspace with self-weight (main), without loading (top inset), and with self weight and a 0.25 kg payload (bottom inset) in horizontal base orientation.	61
3.1	Soft robotic manipulator model. The load capacity is defined as the maximum load that the arm can lift to $y = 0$ at the test pressure $p_{test}$ .	64
3.2	Sections 1, 2, and 3 of a three section robot are designed to have 360, 180, and 120 degree wrap angles, respectively, to provide the desired dexterity.	64
3.3	Base section configurations for (a) fixed tube diameter ratio and (b) fixed base diameter ratio.	69

3.4	Load capacity versus arm length for optimal pneumatic two section (solid), three section (dashed), four section (dash-dotted) and five section (dotted) arms for a fixed tube diameter ratio. . . . .	71
3.5	Load capacity versus arm length for optimal hydraulic two section (solid), three section (dashed), four section (dash-dotted) and five section (dotted) arms, for a fixed tube diameter ratio. . . . .	72
3.6	Hydraulic test case showing load capacity (triangles) and tube thickness (circles) as a function of number of sections. . . . .	73
3.7	Load capacity (dashed) and tube thickness (solid) for the optimal three section hydraulic arm versus Young's modulus. . . . .	74
4.1	Schematic showing the use of a base-mounted load cell for shape sensing of a three section soft robotic manipulator in planar operation. An inclinometer is also mounted on the base. . . . .	93
4.2	Schematic showing the use of cable encoders (–) for shape sensing of a three section soft robotic manipulator in planar operation. An inclinometer is also mounted on the base. . . . .	93
4.3	Schematic showing the use inclinometers for shape sensing of a three section soft robotic manipulator in planar operation. If the weight of the tip payload is known, an inclinometer at the tip is not required. . . . .	94
4.4	Error in manipulator tip position estimation averaged (RMS) over 64 configurations in the horizontal base orientation using cable encoders with a constant curvature model (dash-dotted), cable encoders with the full model (solid) and the load cell method (dashed). The inset shows details of the tip position estimation error for the cable encoder method with full model (solid) and the load cell method (dashed). The area representing one standard deviation around the average error is shaded. . . . .	94
4.5	Error in manipulator tip position estimation averaged (RMS) over 64 configurations in the vertical base orientation using cable encoders with a constant curvature model (dash-dotted), cable encoders with the full model (solid) and the load cell method (dashed). The inset shows details of the tip position estimation error for the cable encoder method with full model (solid) and the load cell method (dashed). The area representing one standard deviation around the average error is shaded. . . . .	95

4.6	Average error in tip position estimation for the inclinometer method (circles), cable encoder method (asterisks) and the load cell method (triangles) without payload (a) and with a payload of 10 N (right). For the hinged boundary condition in absence of payload, shape estimation without sensing coincides with the load cell method. In presence of payload (b), shape estimation without sensing (asterisks) shows high error if the payload weight is unknown. . . . .	96
5.1	Continuous Tube (CT) manipulator: (a) 3D schematic (b) Photograph of fabricated arm. . . . .	101
5.2	Cross-sectional view of the (a) six- and (b) three- extensor sections in the OctArm manipulator and the base section of the CT manipulator (c), showing three independent control channels in red, yellow and blue. The three-tube section of the continuous tube manipulator is identical to (c) with tubes 4,5 and 6 removed. . . . .	102
5.3	Model for a two-section soft robotic manipulator. . . . .	102
5.4	Theoretical (left) and experimental (right) workspace for the OctArm (top) and CT (bottom) manipulators: Endpoint positions (red dots) and workspace density contours (points /cm <sup>2</sup> ). . . . .	108
5.5	Dexterity measures for the OctArm (left) and continuous-tube (CT) (right) manipulators: (a) minimum singular value, $\sigma_2$ (10 <sup>-8</sup> m/Pa), (b) maximum singular value $\sigma_1$ (10 <sup>-6</sup> m/Pa), (c) manipulability, $\sqrt{\sigma_1 \sigma_2}$ (10 <sup>-8</sup> m/Pa), (d) isotropy, $\sqrt{\frac{\sigma_1 \sigma_2}{\sigma_1 + \sigma_2}}$ and (e) condition number, $\frac{\sigma_1}{\sigma_2}$ . . . . .	110
5.6	Dexterous workspace area fraction versus dexterity threshold for the OctArm (solid) and CT (dashed) manipulators. . . . .	111
B.1	Load capacity versus last section length for optimal hydraulic two section (solid), three section (dashed), four section (dash-dotted) and five section (dotted) arms. . . . .	124
B.2	Load capacity versus last section length for optimal pneumatic two section (solid), three section (dashed), four section (dash-dotted) and five section (dotted) arms. . . . .	125
B.3	Load capacity versus arm length for optimal hydraulic two section (solid), three section (dashed), four section (dash-dotted) and five section (dotted) arms for the case of fixed overall diameter. . . . .	125
B.4	Load capacity versus arm length for optimal hydraulic two section (solid), three section (dashed), four section (dash-dotted) and five section (dotted) arms for the case of fixed overall diameter, and a last section bending of 180 degrees. . . . .	126

B.5	Load capacity versus arm length for optimal pneumatic two section (solid), three section (dashed), four section (dash-dotted) and five section (dotted) arms for an overall diameter/length ratio of 0.09. . . . .	126
B.6	Load capacity versus arm length for optimal hydraulic two section (solid), three section (dashed), four section (dash-dotted) and five section (dotted) arms for an overall diameter/length ratio of 0.09. . . . .	127

# List of Tables

1.1	Strengths and weaknesses of hard and soft robots. . . . .	4
2.1	Parameters of OctArm V . . . . .	57
2.2	Mean values of manipulator tip position over the workspace. . . . .	58
3.1	Design parameters for pneumatic and hydraulic soft robot manipulators	68
4.1	Summary of the shape estimation methods for a three section manipulator in planar operation . . . . .	79
4.2	Design parameters for the OctArm VI manipulator . . . . .	89
4.3	Sensor resolution values for experimental validation . . . . .	90
4.4	Configurations with minimum and maximum tip position estimation errors for horizontal orientation. . . . .	91
4.5	Configurations with minimum and maximum tip position estimation errors for vertical orientation. . . . .	91
5.1	End section moments and moments of inertia for the OctArm and CT manipulators. . . . .	103

# Acknowledgments

I would like to express my sincere gratitude to my advisor, Dr. Christopher Rahn for giving me the opportunity to work with him, and for his valuable and insightful guidance throughout this work. His support and encouragement, in academic as well as non-academic matters, during my graduate studies at Penn State made the whole experience highly supportive and educational. Without his timely advice and direction it is impossible to complete this work.

I would like to thank the wonderful committee members Dr. Mary Frecker, Dr. Eric Mockensturm, and Dr. George Lesieutre for taking time of their busy schedules and providing valuable suggestions.

I would like to thank the Biodynotics team members for their great team work. I am also thankful to labmates and colleagues Hareesh Reddy, Amir Lotfi, Haiyu Zhao, Arun Rajamani, Kiron Mateti, Thomas Levard, Paul Diglio, Ying Shi, Mark Zheng, Githin Prasad, Lloyd Scarborough, Matthew Pattom, Lijun Jiang, Ailin Liu, Suyi Li, Arash Mahdavi, Raghavan Balaji and Jianping Guo for their support. I would like to thank my loving parents and sister for encouragement.

## Introduction

Over the last ten years, researchers have developed soft robots that provide new capabilities relative to traditional, hard robots. Hard robots are typically used in well defined environments where they repetitively perform a prescribed motion with great precision. This capability is exploited in many successful applications, primarily in manufacturing. These robots are designed to be stiff so that vibration and deformation of the structure and drivetrain do not reduce the accuracy of movement.

Soft robots, on the other hand, generate little resistance to compressive forces. These robots have the potential to work in unstructured environments, conform to obstacles, and provide high dexterity. Applications include personal robots that interact with people without causing injury, service and painting robots that need high dexterity to reach confined spaces, and defense and rescue robots that operate in unstructured environments.

Soft and hard robots use different mechanisms to enable dexterous mobility (see

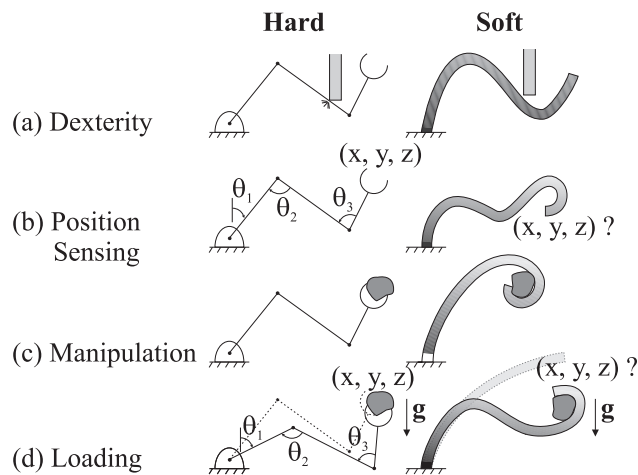


**Figure 1.1.** Capabilities of hard and soft robots.

Figure 1.1(a)). Hard robots have multiple flexible joints connected by stiff links. Each joint is flexible in one rotary or translational direction to provide a degree of freedom of robot motion. The combined motion of all the degrees of freedom sweeps out the workspace or the locus of points that the tip position can attain. Unlike hard robots that have isolated flexible joints in an overall hard structure, soft robots deform continuously throughout their structure. Thus, soft robots have distributed deformation with theoretically an infinite number of degrees of freedom. This leads to a hyper-redundant configuration space wherein the robot tip can attain every point in the 3D workspace with an infinite number of robot shapes or configurations.

The finite, controllable degrees of freedom of a soft robot are dictated by the actuators. Hard robots have an actuator, typically an electric motor, for every joint. The actuators of soft robots are typically integrated into and distributed throughout the structure. Often, the actuators make up most of the structure. This dual actuator/structure

functionality prevents the use of many traditional hard actuators such as electric motors in soft robots. The deformation resulting from activation of an actuator is defined by the actuation mechanism and strain and the actuator size, shape and location in the structure. Soft robots fall into a class of systems that are termed “under-actuated” because, unlike hard robots, there is not an actuator for every degree of freedom. Other degrees of freedom may be influenced by the actuators but many degrees of freedom will not be controllable.

Sensing and controlling the shape of a soft robot is challenging. Their structure is a continuum, so exact measurement of the shape and tip position is difficult. Deciding what to measure and how to use the measurements to control mobility is challenging. Hard robots measure the position of each joint with a high resolution encoder as shown in Figure 1.1(b). Assuming a rigid robot, the joint positions can be processed by the forward kinematics to accurately determine the shape and tip position of the robot. Similarly, the inverse kinematics can often be used to determine the joint positions that provide a desired tip position. The joint positions measured by the encoders are compared to the desired positions calculated from the inverse kinematics and the actuators then servo the errors to zero. This servo action is typically quite fast and forces the joints to stiffly track their desired positions.

Soft robots interact with the environment differently than their hard counterparts. The environment applies loads to the structure either through distributed loading (*e.g.*, gravity) or by contact. In a hard robot, Figure 1.1(c) shows that loading causes the soft

**Table 1.1.** Strengths and weaknesses of hard and soft robots.

	Strength	Weaknesses
<b>Hard Robots</b>	<ul style="list-style-type: none"> <li>• High accuracy</li> <li>• High load capacity</li> <li>• Easy controllability</li> <li>• Easy path planning</li> <li>• Easy end effector position sensing</li> </ul>	<ul style="list-style-type: none"> <li>• Low dexterity</li> <li>• Dangerous</li> <li>• Designed for structured environments</li> <li>• Collide with obstacles</li> <li>• Limited dexterity</li> <li>• Bulky</li> </ul>
<b>Soft Robots</b>	<ul style="list-style-type: none"> <li>• High dexterity</li> <li>• Safer</li> <li>• Work in unstructured environments</li> <li>• Manipulate objects of different sizes</li> <li>• Conform to obstacles</li> <li>• High reachability and manipulability</li> </ul>	<ul style="list-style-type: none"> <li>• Low accuracy</li> <li>• Low load capacity</li> <li>• Difficult to control</li> <li>• Complex path planning</li> <li>• Difficult end effector position sensing</li> </ul>

joints to change position while the rigid links remain straight. The encoders measure the position change and the controller can either compensate for the loading or understand that the robot has contacted the surroundings. In either case, the shape and tip position can be exactly determined. Gravity and contact loading cause continuous deformation in a soft robot that may not be observable or controllable from the limited sensors or actuators, respectively.

Contact and conformation with the surrounding environment play an important role in the mobility of soft robots. Soft robot arms, for example, use whole arm manipulation to grasp and handle objects of varying size as shown in Figure 1.1(d). The arm wraps around the object and a tight grasp and high friction contact enables the arm to lift the object. Hard robot arms grasp and handle objects with a specialized end effector that is typically designed for a specific size and type of object. Soft robots can locomote using a variety of gaits with a large portion of their structure in ground contact at any instant in time. Hard robots use separate legs, tracks, and wheels to contact the ground and enable locomotion.

Figure 1.2 shows how a soft robot arm deforms under combined gravitational loading and actuation. Hard robots can servo the arm to any shape if the links are sufficiently stiff and the load is sufficiently low. The actuators on a soft robot arm often apply a moment or torque at the tip of the arm. For small displacements, this tip moment causes the arm to bend upward with a quadratic shape. In a gravitational environment, self-weight bends the arm downward with a cubic shape. The tip moment can be adjusted to lift the tip to horizontal but the arm will have a nonzero shape associated with the difference between the quadratic and cubic shapes. Similarly, if a sensor is employed that measures the moment at the base of this example soft robot arm, one cannot differentiate between a point load at the tip and a distributed load. These loadings, however, produce markedly different arm shapes.

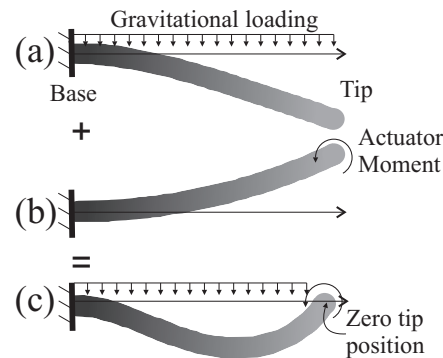


**Figure 1.2.** Gravitational loading on a soft robot manipulator causes downward deflection (a), actuators bend the structure upward (b) and net displacement has zero tip position but nonzero shape (c).

## 1.1 Biological Inspiration

There are many examples in nature of mobile structures made from soft materials. Muscular hydrostats such as elephant trunks, mammal and lizard tongues, and octopus arms are soft structures that can bend, extend, and twist. Fiber reinforcement in soft plant cell walls enables the cell to change shape when pressurized. Mimicry of these complex structures is neither necessary nor practical to the development of soft robots. Fundamental understanding of the morphology and functionality of soft structures in nature, however, increases insight and can lead to new design concepts in soft robotics. The natural world demonstrates the potential capabilities of soft robots.

### 1.1.1 Hydrostatic Skeletons and Muscular Hydrostats

Animals such as worms and sea anemones lack the rigid jointed skeletons that are found, for instance, in the vertebrates (*e.g.*, mammals, birds, and reptiles) and arthropods (*e.g.*,

insects and crabs). Instead, these soft-bodied animals depend on a “hydrostatic skeleton” for support [3, 4, 5, 6]. Hydrostatic skeletons are typically cylindrical, fluid-filled cavities surrounded by a muscular wall that is reinforced with connective tissue fibers. The fluid is usually a liquid (essentially water) and thus resists significant volume change. Thus, if muscle fibers in the wall contract to decrease one of the dimensions, another dimension must increase. By arranging the musculature so that all dimensions can be actively controlled, a diverse array of movements and shape change can be produced. Force transmission is thus provided not by rigid links, but instead by pressure in the enclosed fluid. This simple principle serves as the basis of support and movement in a diverse group of soft-bodied animals. Hydrostatic skeletal support may also be important in organisms that typically rely on rigid skeletons. For example, crabs rely on hydrostatic skeletal support after they have shed their exoskeleton during molting and before the newly formed cuticle has hardened [7, 8] and hydrostatic pressure under the skin of sharks may provide a means of transmitting force to the tail [9].

In addition to large fluid-filled spaces and muscle fibers arranged in multiple orientations, the walls of most hydrostatic skeletons are reinforced with connective tissue fibers (most commonly the protein collagen) arranged as continuous parallel sheets of fibers that wrap the animal in both left- and right-handed helical arrays. Such “crossed-fiber helical connective tissue arrays” provide reinforcement for the walls and allow both smooth bending and change in length [10, 11]. The fiber angle, the angle that the fibers make with the long axis, has been shown to control and limit shape change in a variety

of worm-like animals [12, 13] and also in hydraulic structures, such as the tube feet of echinoderms (starfish, sea urchins, brittlestars, sea cucumbers) [14].

Kier [15] introduced the term “muscular hydrostat” to describe a group of soft animal structures that lack the large fluid-filled cavities that characterize the hydrostatic skeletal support systems of other soft-bodied animals. Examples of muscular hydrostats include the arms of octopuses, the arms and tentacles of squid, many tongues, the elephant trunk, and a variety of invertebrate structures (see Figure 1.3). These structures are typically capable of diverse and complex movement and are unusual because the musculature generates both the force for movement and also provides skeletal support. Support and movement are achieved in a similar way to conventional hydrostatic skeletons by exploiting the near incompressibility of muscle at physiological pressures and by arranging the musculature to control all three dimensions. The morphology and biomechanics of several muscular hydrostats have been examined, including squid arms and tentacles [15], squid and cuttlefish fins [16], chambered nautilus tentacles [17] octopus suckers [18], chameleon tongue [19], microhylid frog tongue [20], human tongue [21], and African pig-nosed frog [22].

Muscles and reinforcing connective tissue play an important role in the functionality of muscular hydrostats. Animal muscle is particularly well suited to soft actuation. [23] summarize the range of performance metrics of muscle, including the maximum force production at constant length, length dependence of force production, the rate at which force can be generated and velocity dependence of force production. Muscles, while all

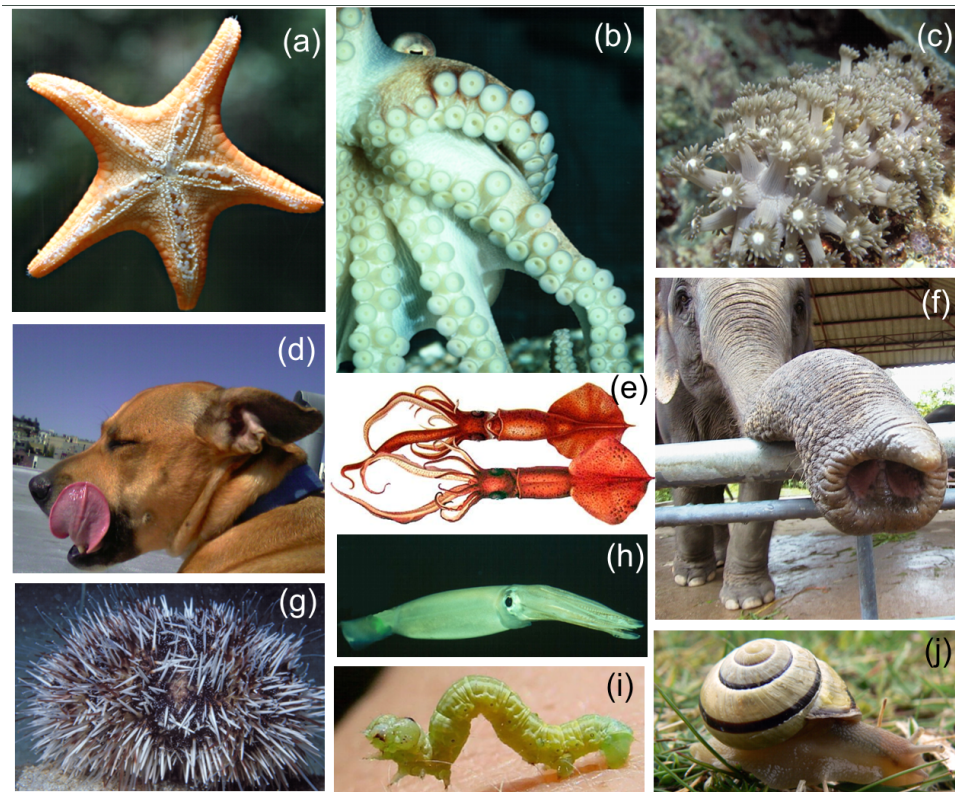


**Figure 1.3.** Examples of hydroskeletons and muscular hydrostats: (a) tube feet in starfish, (b) octopus arms, (c) colonial anemone, (d) mammalian tongue, (e) squid, (f) elephant trunk, (g) echinoid, (h) *Illex illecebrosus* (i) inchworm, and (j) snail feet.

being contractile, have wide variability in characteristics among different species and even among different muscles in the same animal [24]. For instance, the extensor musculature of the squid tentacle contracts at a peak velocity of approximately 15 lengths per second and shows a peak stress of approximately  $130 \text{ mN mm}^{-2}$ , while the analogous musculature in the arms of squid (responsible for support of the arms) contracts at only 1.5 lengths per second but shows a peak stress of approximately  $470 \text{ mN mm}^{-2}$  [25]. And although the extensor musculature of the tentacles operates over a range of strain of less than 30%, the retractor musculature of the tentacles operates over a range of strain of greater than 80% [26]. As there are limited strain amplification mechanisms

in soft structures, high strain is often required for high mobility. Inactivated muscle can be easily extensible and allow large deformation with limited stress. When activated, however, the stress can be large to enable the structure to do significant work on the environment. This variable stress capability of animal muscle gives muscular hydrostats unique dexterity and load bearing capabilities.

As an example of a sophisticated muscular hydrostat, Figure 1.4 shows the morphology of an octopus arm [27]. Layers of muscle with different orientations wrap around the central nerve cord. Fibers of the core of transverse musculature (TM) are oriented in the radial direction and interleave with the next two layers of oblique musculature (OM) and longitudinal musculature (LM), that are helically wound around the arm and aligned along the axis of the arm, respectively. Two layers of oblique musculature separated by a layer of longitudinal musculature surround the arm just under the external skin. The oblique muscle fiber layers are wound in both the clockwise (CW) and counter clockwise (CCW) directions. The muscle layers are integrated with both discrete layers of connective tissue and with networks of connective tissue fibers in the musculature. Contraction of the longitudinal muscle fibers causes the arm to shorten. Contraction of the transverse muscle fibers acts antagonistically to the longitudinal muscle fibers to cause arm extension. Simultaneous contraction of the transverse and longitudinal muscle fibers increases the flexural stiffness of the arm, allowing it to bear loads. If the longitudinal muscle fibers are not uniformly contracted around the circumference, the arm bends in the softest direction. Thus, activating the longitudinal and transverse mus-

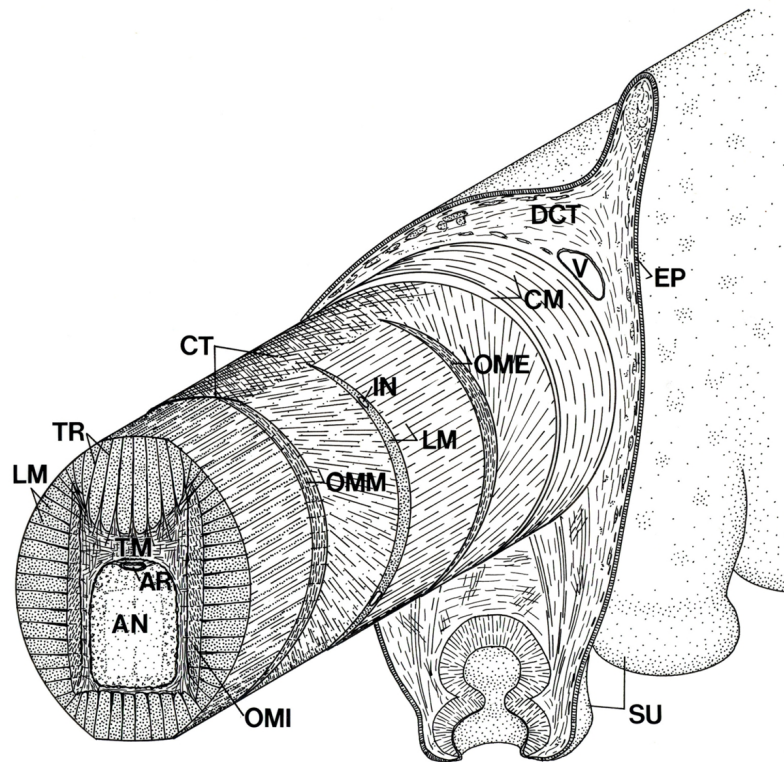


**Figure 1.4.** Diagram of the arm of *Octopus* showing three-dimensional arrangement of muscle fibers and connective tissue fibers. AN, Axial nerve cord; AR, artery; CM, circumferential muscle layer; CT, connective tissue; DCT, dermal connective tissue; EP, epidermis; IN, intra-muscular nerve; LM, longitudinal muscle fibers; OME; external oblique muscle layer; OMI, internal oblique muscle layer; OMM, median oblique muscle layer; SU, sucker; TM, transverse muscle fibers; TR, trabeculae; V, vein.

cle fibers along the length and around the circumference of the arm causes the arm to bend in complex shapes. Activation of the CW and CCW oblique muscle fiber layers twists the arm in the CCW and CW directions, respectively. Thus, this carefully constructed structure of soft active material and connective tissue can produce large and complex extension, bending, and twisting motions.

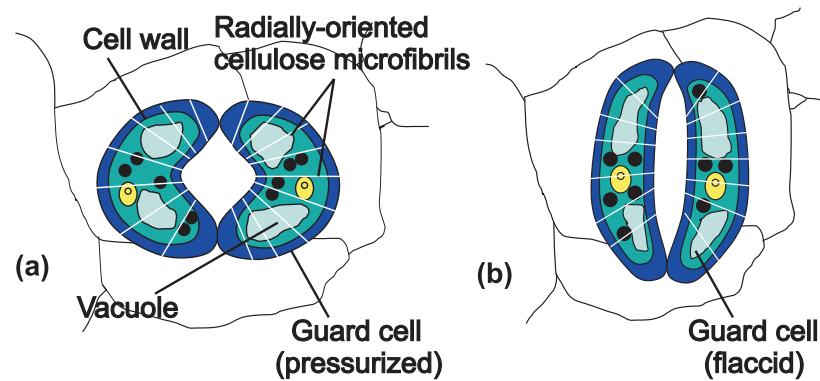


**Figure 1.5.** A schematic of open (a) and closed (b) stomata in plant cells caused by osmotic pressurization.

### 1.1.2 Soft active plant structures

In many plants, the soft cell walls are reinforced by stiff fibrillar networks. A variety of osmotic processes pressurize the cell in response to different stimuli (*e.g.*, light or pressure), leading to plant movement. The fibers are oriented to ensure that the cell deforms in a specific direction when pressurized. The guard cell shown in Figure 1.5, for example, controls aspiration in plant leaves, thereby limiting water loss [28]. The microfibrils are wound around the circumference of the cell at an angle to the curved longitudinal axis. When pressurized by osmosis, the guard cells deform to open the stoma and allow gas exchange to take place. If large numbers of cells are aligned in a plant structure they can cause macroscopic changes in shape. This mechanism is responsible for phototropism or sun tracking [29] and the large and fast deformation of the Venus fly trap and Mimosa plants [30, 31].

## **1.2 State of the Art in Soft Robotics**

Inspired by the outstanding capabilities of soft animal and plant structures, researchers have developed hard robots that mimic soft structures and soft robots that use electroactive polymer (EAP) and pneumatic artificial muscle (PAM) actuators. The octopus arm and guard cell indicate the potential for soft mobile structures but significant challenges remain in the development of soft robots and specifically the areas of active materials, electromechanical design, modeling for optimization and control, and fabrication. This section describes some of the most interesting examples of soft terrestrial and aquatic robots and manipulators that have been built and experimentally tested in the last 20 years.

### **1.2.1 Hard robots with soft capabilities**

Robotics researchers have developed a variety of terrestrial (wheeled, tracked, crawling, and legged) and aquatic (swimming) robots and manipulators that employ primarily rigid materials but achieve flexibility that is reminiscent of biological structures. Notable examples of hard robots that are inspired by soft structures found in nature include crawling and swimming robots and trunk-like manipulators. Crawling robots use undulatory locomotion based on the coupling between the robot deformations and the ground [32]. Examples of crawling robots include snake-like climbing robots [33] and snake robots [34]. Swimming robots that mimic the continuous motion of fish using a rigid linkage include the thunniform robots called RoboTuna I and II [35], the AQUA Project

[36], Essex robot fish [37], a Micro Underwater Vehicle [38], an amphibious snake-like robot [39] and the Boxybot fish that can dive, move forwards and backwards, swim on its side and spin [40]. These robots do not provide the more efficient and noiseless continuous motion of a soft, flexible swimming body [41]. There are many legged robots with rigid structures that use electric/magnetic, piezoactive or thermal (Shape Memory Alloy) actuation [42].

Trunk-like manipulators have been built using rigid structures and electric motors with cable tendons for actuation. Takanobu *et al.* [43] develop a multi-d.o.f. robot based on the tongue. Cieslak *et al.* [44] develop an elastic manipulator using cable tendon actuators. Hannan and Walker [45] develop a 4-section ‘elephant trunk’ manipulator with sections actuated by a hybrid cable and spring servo system (see Figure 1.6). OCRobotics builds trunk-like commercial robots called “snake-arm robots” [45] also using cable tendon actuators with alternating rigid and soft disks to form a bendable backbone.

### **1.2.2 Soft EAP Robots**

Electroactive polymers [46, 47] have many characteristics, including low weight, fracture tolerance, pliability, and relatively large actuation strain that make them especially suitable for soft robots [48]. EAPs can be broadly classified into electronic EAPs (dielectric elastomers, electrostrictive graft elastomers, electrostrictive paper, electroviscoelastic polymers, ferroelectric polymers, and liquid crystal elastomers) and ionic



**Figure 1.6.** Elephant trunk manipulator

EAPs (carbon nanotubes, conductive polymers, electrorheological fluids, ionic polymer gels, and ionic polymer metallic composites) [23]. In general, ionic EAPs operate at low voltage but require constant hydration and produce low stress, limiting their applications. On the other hand, electronic EAPs produce relatively large strains, respond quickly, and are relatively efficient, but often require high actuation voltages [23].

Pelrine *et al.* [49] conclude that dielectric elastomers [50, 51] are closest to animal muscles based on criteria of strain, actuation pressure, density, efficiency and speed. Interesting applications of dielectric elastomers in soft robotics include a lightweight six-legged robot [52], a series of legged robots called MERbots [53] that use multifunctional electroelastomer rolls and lightweight robots with actuators that mimic the longitudinal muscles of earthworms for locomotion [54]. A hyper-redundant digital manipulator

driven by embedded dielectric polymer actuators can perform precise discrete motions without the need for sensing and feedback control [55].

A review of conducting polymers actuators is provided in [56]. Lin *et al.* [57] develop a tortoise-like flexible microrobot that can crawl and swim underwater using four legs actuated by Ionic Conducting Polymer Film (ICPF). Guo *et al.* [41] develop a 45 mm long fish-like underwater microrobot using ICPF actuators made from perfluoro-sulfonic acid polymer films that drive a pair of tails with fins. Speeds from 0 to over 5 mm/s can be obtained by the changing frequency and amplitude of the input voltage from 0.1 Hz to 5 Hz and 0.5 V to 10 V, respectively. Microgrippers and other actuated devices have been fabricated using conjugated polymers [58]. Alici *et al.* [59, 60] develop a gripper that can lift objects up to 50 times the total weight of the polymer actuators.

Ionic polymer-metal composites are a popular material for use in soft robots [61, 62, 63]. Successful applications include wormlike robots [64, 65] that imitate the traveling wave observed in undulatory locomotion, an underwater propulsion robot that uses the IPMC as a fin to generate forward impelling force [66], fish-like vehicles [67, 41, 68, 69, 70], a ciliary based 8-legged walking microrobot [71], and a multi-DOF micromanipulator [72].

Electroactive polymer gels [56] have been used to fabricate a hand with gel fingers [73] and gel robots [1]. The gel robots are made entirely of electroactive polymer gel

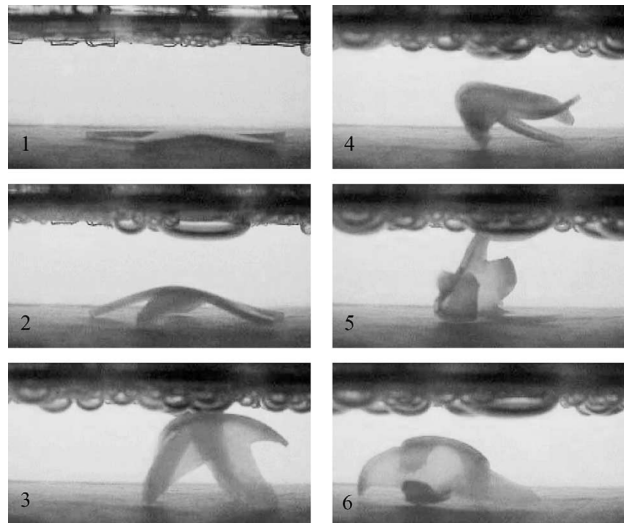


**Figure 1.7.** A starfish gel robot that turns over [1].

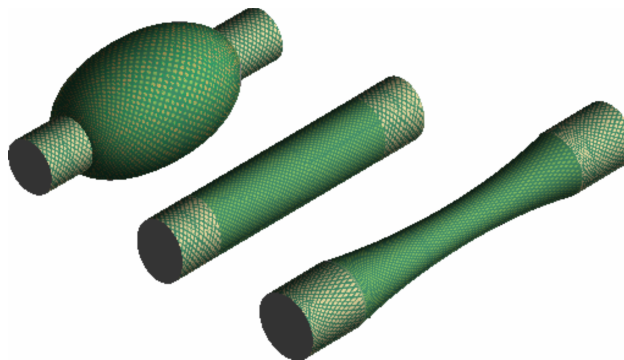


**Figure 1.8.** Pneumatic Air Muscle actuators with a mesh angle of less than  $54^{\circ}44'$  contract on pressurization (left), with a mesh angle of  $54^{\circ}44'$  neither extend or contract (middle), and of greater than  $54^{\circ}44'$  extend on pressurization (right).

that changes shape under spatially varying electric fields. Figure 1.7 shows a starfish gel robot that turns over upon application of electric fields. Osamu *et al.* [74] develop a ciliary motion actuator using self-oscillating gel.

### 1.2.3 Soft PAM Robots

Pneumatic Artificial Muscles (PAMs) (Figure 1.8) are pneumatic actuators that consist of a thin, flexible, tubular membrane with fiber reinforcement [75]. Braided and netted PAMs have high and low density fiber mesh, respectively. The fibers can either be embedded in the wall of the actuator or applied as a braided sleeve on the outside of the tube. The well known McKibben muscles have braided, embedded fibers [76]. Several other designs for PAMs have been patented [77, 78, 79, 80, 81]). The maximum contraction strain is approximately 57%. The blocking force, however, can be extremely large due to the leveraging of the radial pressure through the braided fibers. Pritts and Rahn [82] introduce extensor actuators where large wind angle (above  $54^{\circ}44'$  - defined as the angle relative to the longitudinal axis) causes the actuator to extend instead of contract upon pressurization as in the previous PAMs. Extensor actuators provide large extensional strain (200% for a wind angle of  $78^{\circ}$ ) but low extensional force. Additionally, they are prone to buckling instabilities under compressional axial loading.

PAMs have been used to make trunk-like soft robotic manipulators. Kinetic Sciences Inc. Immega *et al.* [83], for example, develop a tentacular robot, powered by a hybrid system of pneumatic bellows and electric motors. It can extend, contract, and bend in six d.o.fs. using tendons threaded through cable guides. Simaan *et al.* [84] develop a manipulator for minimally invasive surgery of the throat, composed of a base disk, an end disk, several spacer disks, four super-elastic backbone tubes, and three push-pull actuators. Suzumori *et al.* [85] develop a pneumatically and hydraulically

cally driven flexible microactuator made of fiber-reinforced rubber. The actuator has three internal chambers, each with a separate control valve. When the internal pressure in the three chambers is increased equally, the actuator stretches in the axial direction. When the pressure of only one of the chambers is increased, the actuator bends in a direction opposite to the pressurized chamber. Wilson *et al.* [86] build a flexible four section robotic arm manipulator made up of orthotropic polyurethane tubes that bend when pressurized. Tsukagoshi *et al.* [87] develop the Active Hose, an elephant trunk type manipulator based on a wound tube actuator consisting of a spiral tube surrounding the backbone like a coil. Festo's Bionic Learning Network [88] designs a swimming robot called Airacuda using pneumatic muscles made of rubber reinforced with aramid fiber. The robot has two muscles that are alternately pressurized to bend the tail and drive the fish forward. Suzumori *et al.* [89] develop a soft-bodied manta swimming robot using an optimal pneumatic actuator cross-section and a new prototyping method.

#### **1.2.4 OctArm VI**

OctArm VI [2] is the latest in a series of soft robotic manipulators designed using air muscle extensors. Fig. 1.9(a) shows a partially transparent 3D view of the entire arm with a photograph of one of the two fabricated arms shown below in Fig. 1.9(d). The extensors are connected together in groups of three and six to create three independently actuated sections. Figure 2.3 shows cross sections of the three actuator configuration used in the third section and the six actuator configuration used in the first two sections.

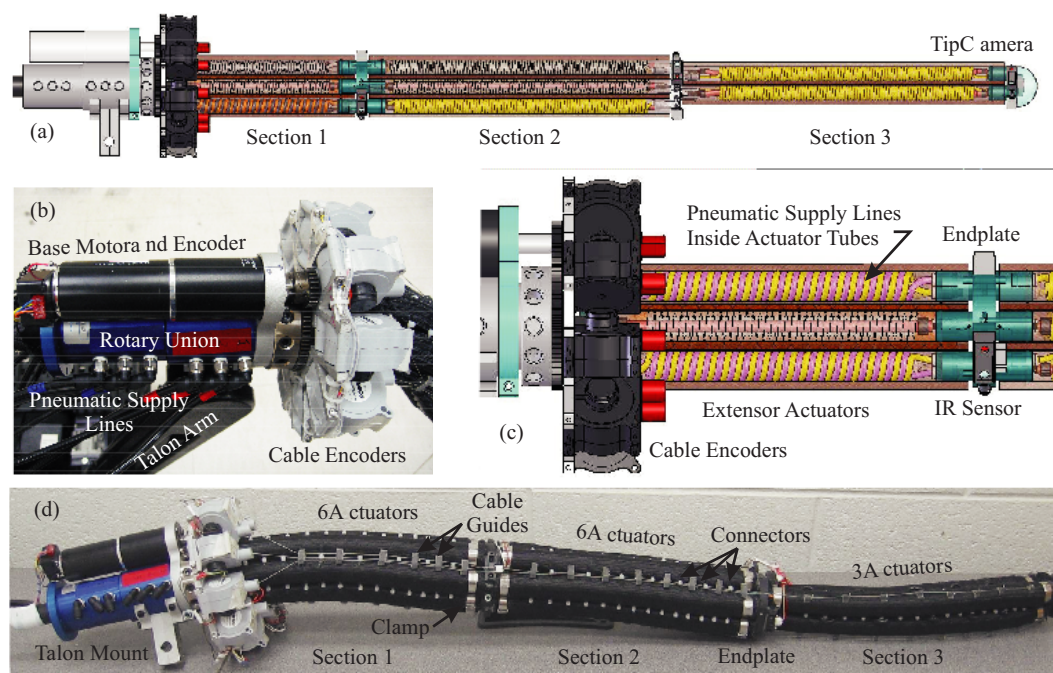


**Figure 1.9.** OctArm VI: (a) Semi-transparent 3D view of arm; (b) Close-up photograph of base; (c) Close-up, semi-transparent view of first section; (d) Photograph of complete arm [2].

Each actuator in the three extensor section can be actuated independently, giving the three control channels shown in blue, red, and yellow. Pairs of actuators in the six actuator sections are actuated together, again forming the three control channels shown in Fig. 2.3. The sections can bend around the  $x$  and  $y$  axes and extend along the  $z$  axis when pressure is applied to each control channel and the corresponding extensors change length. The three sections are connected in series and can be actuated independently through tubing that connects to pressure control valves on the mobile base (Talon), providing nine degrees of freedom. The manipulator is mounted on a rotational base (See Fig. 1.9(b)) that provides continuous 360 degree rotation with pneumatic and electrical passthroughs. The rotary base is attached to the two degree of freedom Talon

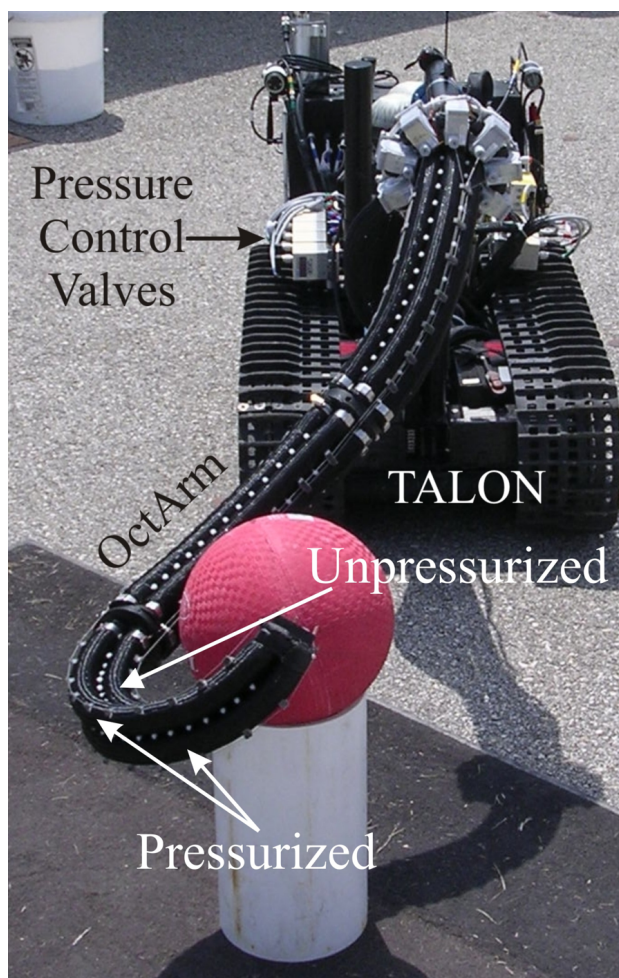


**Figure 1.10.** OctArm VI mounted on a mobile base (TALON), reaching around a ball.

arm, resulting in a total of twelve degrees of freedom. This provides the ability shown in Figure 1.10 to wrap the arm around objects.

The air delivery system of OctArm VI is complicated by the tight packaging requirements, high pressure and loading, and rotary base. Endplates connect adjacent sections and include air passageways, tubing connectors, and barbed fittings that attach the extensor actuators using low profile clamps. CNC machining enables the design of geometrically complex endplates (See Fig. 1.9(c)) with integrated fittings, axially-

aligned actuators, and interior air passages.

An innovative packaging design wherein the pneumatic supply tubes are routed within the actuators is used. In the first section, nine coiled air tubes pass through the six actuators with three actuators each having two coiled air tubes. Three of these supply air to the actuators in section 2. One is provided as an additional air supply at the second endplate for supplemental pneumatic actuators (*e.g.* suction cups). Five continue on through the six actuators in section 2. Three of these supply air to the actuators in section three, one provides auxiliary air to the third endplate, and the last airline passes through an actuator in section 3 to provide auxiliary air to the tip endplate.

Cable encoders and a base rotary encoder provide full sensing of all OctArm degrees of freedom (See Fig. 1.9(b)). The cable encoders are mounted behind the base endplate. The encoder in the sensor counts the rotations of the drum on which the cables are wound. The cable encoder wires thread through cable guides and connect to one of the three endplates. Three cable encoders measure the length of the extensors in section 1, three measure the extensor lengths of section 1 plus section 2, and the last three measure the total lengths along each extensor group. Thus, all nine degrees of freedom are measured. Additional actuators include three infrared range sensors mounted on each endplate and a CMOS camera mounted at the tip. The wiring harness is pigtailed so that it can sustain the large arm elongation ( $> 60\%$ ).

Large initial wind angles ( $\alpha$ ) in the extensor actuators result in large extensions under applied pressure. Thus, we fabricate the arm with the largest possible initial

mesh angle. This is limited by the interference between the two families of fibers to approximately  $78^\circ$ . The initial length,  $L$ , outer radius,  $R_o$ , inner radius  $R_i$ , and the tube elastic modulus,  $E$ , are other important design parameters for the extensors. In OctArm VI, the same tubes and meshes are used in all three sections for ease of design and fabrication.

### 1.2.5 Modeling

The structural mechanics of soft actuators and manipulators, natural as well as artificial, is complicated due to both material and geometric nonlinearities. Researchers develop biomechanical models that predict the behavior of several soft animal appendages. Skierczynski *et al.* [90] develop a model of the hydrostatic leech skeleton to predict the shape of and internal pressure within the animal in response to motor neuron activity. Liang *et al.* [91] present an explicit finite element simulation scheme for biological muscular hydrostats. Yekutieli *et al.* [92] derive a 2D dynamic multisegment lumped parameter model of the octopus arm and use it to explore movement control strategies. Van Leeuwen *et al.* [26] present a forward dynamics model of tentacle extension in squid to predict the changing geometry of the tentacle and the pressure, stress and kinetic energy distributions. Biomechanical models for tongue movements [21, 93, 94], caterpillar locomotion [95] and elephant trunks [96] have also been developed.

Modeling of soft robotic manipulators combines large deformation constitutive models of the active materials that form the manipulator, with nonlinear kinematics of the

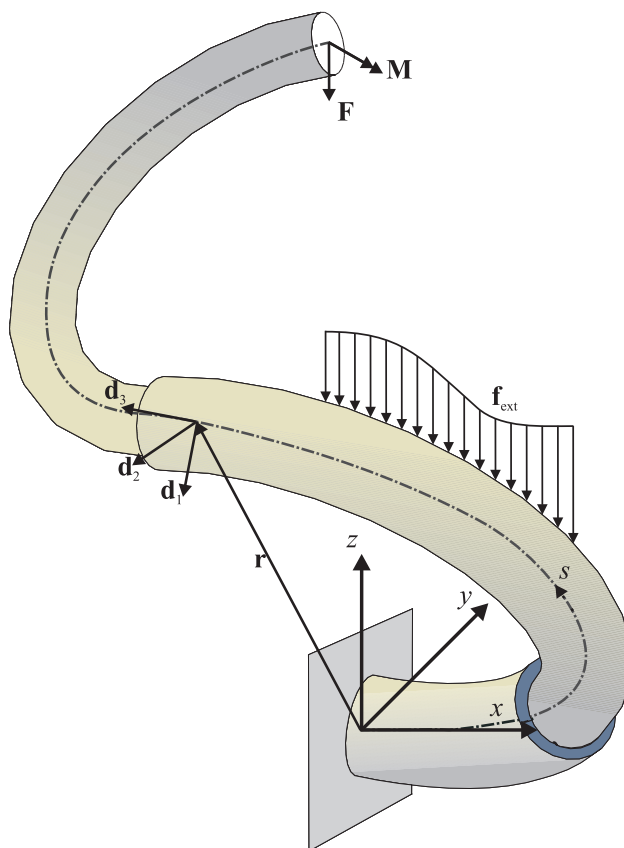


**Figure 1.11.** Soft robotic manipulator modeled using the Cosserat rod approach, with the backbone position ( $\mathbf{r}$ ) and orientation ( $\mathbf{d}_1$ ,  $\mathbf{d}_2$ ,  $\mathbf{d}_3$ ) parameterized by a single variable  $s$ . The manipulator is acted upon by distributed force ( $\mathbf{f}$ ) and discrete forces ( $\mathbf{F}$ ) and moments ( $\mathbf{M}$ ).

manipulator. Constitutive relations for active materials vary widely but general models for the kinematics of soft robotics can be described using, for example, spatially varying quaternions [97]. Soft robotic manipulators are kinematically similar to hyper-redundant manipulators with extremely large d.o.fs., so models that approximate continuum manipulators by finite d.o.f. hyper-redundant manipulators may be appropriate. In this approach, the accuracy and computational cost are proportional to the number of d.o.fs. [98]. Many researchers [98, 99, 100] take the opposite approach by using a continuum approach to approximate the dynamics of hyper-redundant manipulators.

For instance, [101] and Mochiyama *et al.* [102, 103] approximate the kinematics and dynamics of manipulators with hyper d.o.fs. using a continuum backbone curve and the Frenet-Serret formulas. However, for numerical simulation, they approximate the backbone curve by a serial chain of rigid bodies with a large number of degrees of freedom. Previous researchers account for the geometric nonlinearities by assuming fixed shapes for robot backbone curves. Hirose *et al.* [104] gives a planar model for snake robots based on a serpenoid backbone curve. Hannan and Walker [105] assume that each section of an elephant trunk manipulator bends into a circular arc with constant curvature and an inextensible backbone Hannan and Walker [106, 107, 108]. Similarly, Nakabo *et al.* [62] use the constant curvature assumption to study the kinematics of a snake-like swimming robot. This assumption makes it possible to formulate the forward manipulator kinematics that relate the position of the manipulator tip to the inputs using a Denavit-Hartenberg formulation that fits a conceptual “virtual” rigid-link robot to the continuum backbone. Recent work by [109] extends this approach by removing the assumption of an inextensible backbone. These methods rely, however, on the assumption of constant curvature which is valid only when there are no external loads (including self-weight) on the manipulator. Gravagne and Rahn [110] study large deflection dynamics for planar continuum robots including the effects of actuator torques but without distributed loading. Self-weight and other loading can cause significant deviations from constant curvature, leading to large tip position error. Tatlicioglu *et al.* [111] extend the model include the effects of potential energy. Trivedi *et al.* [97] de-

velop a model for trunk-like robots using the Cosserat-rod approach, taking into account extension and shear (see Figure 1.11). [112], use geometrically exact beam theory and the Newton-Euler technique to predict control torques of an eel-like robot as a function of expected internal deformations of an eel's body.

Complexity makes material model development difficult for soft EAP robots [47]. Many researchers [1, 113] have developed models to predict the performance of particular EAP actuators. Madden *et al.* [114] compile an online database of experimental methods and results (mechanical, electrical, chemical and other properties) for EAP-based actuators to facilitate actuator selection for design.

### **1.2.6 Control**

To achieve point-to-point limb movements, the animal nervous system generates a sequence of motor commands that move the limb toward the target. In muscular hydrostats, this process is complicated because of the virtually infinite number of degrees of freedom [115]. Reducing the number of d.o.fs. through coordination is a key problem in motor control of hyper-redundant limbs. Gutfreund [116] study octopus arm movements to identify general principles of control. They conclude that the octopus actuates its arm for locomotion, reaching for objects, or searching by a wave-like propagation of arm stiffening that travels from the base of the arm toward the tip. The region of stiffening tends to move within a plane in a slightly curved path connecting the center of the animal's body with the target location. The authors propose that this

strategy reduces the immense redundancy of the octopus arm movements and hence simplifies motor control. Sumbre *et al.* [117] conclude that octopuses use strategies similar to vertebrates for transferring an object from one place to another. The octopus temporarily configures its arm into a stiffened, articulated, quasi-jointed structure based on three dynamic joints. Rotational movements around these joints brings the object to the mouth. Kinematic invariants in octopus arm motion exist at the joint level rather than at the end-effector level, suggesting intrinsic control coordination. This indicates that a kinematically constrained articulated limb may provide an optimal solution for precise point-to-point movements [118].

Yekutieli *et al.* [92] show that a simple command producing a wave of muscle activation moving at a constant velocity is sufficient to replicate the natural reaching movements of octopus arms with similar kinematic features. Sumbre *et al.* [115] show experimentally that the basic motor program for voluntary movement of octopus arm is embedded within the neural circuitry of the arm itself. Such peripheral motor programs represent considerable simplification in the motor control of these appendages.

Accurate control of soft robots requires model-based prediction of the set of possible configurations. Wormlike robots employ sequential control input from “tail” to “head,” resulting in successive bending of the body to create the traveling wave observed in natural undulatory motion. Cellular neural networks (CNNs) create central pattern generators (CPGs) that propagate the travelling wave for locomotion control [64]. Each CNN cell is a nonlinear oscillator that is coupled to the other oscillators and controls an

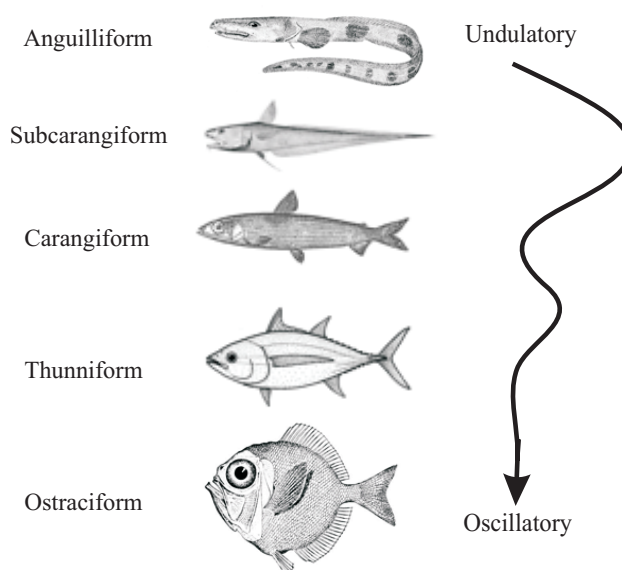


**Figure 1.12.** Body/Caudal fin propulsion (BCF) modes used for swimming robots.

actuator, acting as a motor neuron of the CPG.

Swimming robots often mimic fish dynamics for locomotion, using, for example, body/caudal fin propulsion (see Figure 1.12). Tadpole [68] and eel [69, 70] robots use undulatory anguilliform locomotion. Anguilliform locomotion is found in some long, slender fish like eels, in which the whole body is displaced laterally, and there is little increase in the amplitude of the flexion wave as it passes along the body. The swimming robot of Guo and Fukuda [41] emulates carangiform locomotion, where movement is restricted to the rear of the body and tail. RoboTuna [35] uses thunniform locomotion for high-speed and long-distance swimming, where the lateral movement is in the tail and the region connecting the main body to the tail. Laurent *et al.* [119] have shown theoretically that robot fish should use undulatory motion rather than oscillatory motion (*e.g.*, ostraciiform locomotion [120]) to obtain best performance. McIsaac *et*

*al.* [121] present a dynamic model of anguilliform swimming for eel-like swimming robots. Swimming gaits for forward and sideways swimming, turning and for following circular paths, are developed using perturbation analysis.

The IPMC based robot developed by Kim and Ryu [71] is an example of a soft robot that locomotes on the ground using ciliary-motion. In each cycle, the front legs and the rear legs are alternately pushed downward and folded upward.

A motor scheme for the control of a single-joint robot arm actuated by McKibben artificial muscles is proposed by Eskiizmirliler *et al.* [122]. In this approach, classical control elements of the cybernetic circuit are replaced by artificial neural network modules having an architecture based on the connectivity of the cerebellar cortex, and whose functioning is regulated by reinforcement learning. After learning, the model accurately pilots the movements of the robot arm, both in velocity and position.

Chitrakaran *et al.* [123] and Hannan and Walker [124] propose the use of an external camera for shape estimation and set-point regulation of soft robotic arms. To simplify the inverse kinematics, Gravagne and Walker [125] propose mapping infinite-dimensional arm configuration space to the finite-dimensional actuator space using natural and wavelet decompositions. They use manipulability and force ellipsoids [126] to analyze the directional dependence of motion and force-exerting capabilities of soft robotic manipulators. Gravagne and Walker [127] show that under the assumption that distributed damping exists on the backbone of a soft robotic manipulator, a PD plus

feed-forward controller can exponentially regulate the manipulator configuration. Braganza and Dowson [128] present a combination of conventional controller with neural network-based learning for OctArm-type manipulators. Gravagne *et al.* [129, 130] formulate a vibration-damping setpoint controller. Otake *et al.* [131] simplify the inverse dynamics of gel robots by selection of a central point on the robot and controlling the trajectory of that point.

### 1.2.7 Path Planning

Path planning for soft robots involves deforming soft appendages to conform to the environment or navigate through confined spaces. Most higher animals navigate using cognitive maps based on current perceptions, memorized events, and expected consequences [132]. An enhanced navigation strategy can dramatically improve the locomotive capabilities of an organism. In soft biological appendages, path planning is complicated by the fact that multiple appendage shapes can achieve the same tip position and orientation. The processes by which animals choose simple paths are not well understood [133]. It has been proposed [134, 135, 136] that those paths are chosen that balance motor command amplitude and endpoint tracking, leading to smooth and direct paths involving minimal motor commands and endpoint error.

Several researchers have attacked the problem of path planning for deformable objects such as routing a soft surgical tool into the small intestine as shown in Figure 1.13. Conru [137] uses a genetic algorithm to find near optimal routes for cables but does not

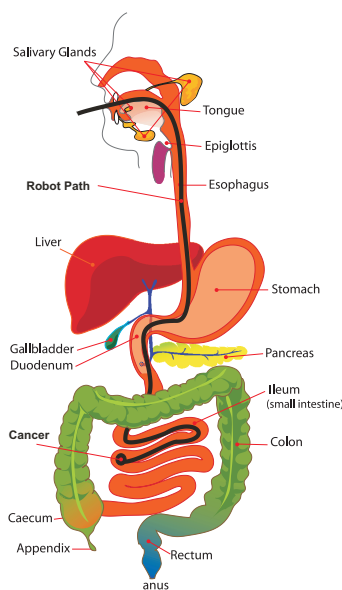


**Figure 1.13.** Path planning for reaching a cancer in the small intestine from the oral cavity.

include constraints imposed by the physical characteristics of the cable or the environment. Several researchers use a probabilistic roadmap (PRM) strategy for path planning of deformable objects [138, 139, 140]. In this approach, a large number of initial configurations are randomly generated and collision free configurations with low energy are retained as roadmap nodes. Once a dense roadmap has been generated, the planner can answer queries by connecting initial and final configurations by searching a path. Holleman [138] and Lamiroux [139] present a probabilistic roadmap planner capable of finding paths in an obstacle field using a low degree Bezier surface patch and an approximate energy function that penalizes deformation. Guibas [140] describes an improved probabilistic algorithm for a surface patch using the medial axis of the workspace to guide the random sampling. Prior to path planning, the medial axis of the workspace is computed and the flexible object is fitted at random points along the medial axis. The

energy of all generated configurations is minimized and the planner connects them with low-energy quasi-static paths along the probabilistic roadmap.

Anshelevich [141] presents a path planning algorithm for deformable volumes such as pipes and cables that uses a lumped-parameter model. This approach imposes constraints on the deformation to reduce complexity and does not work on general deformable objects. Bayazit [142] computes an approximate path and then refines the path by applying geometric-based free-form deformation to the robot. The approximate path can penetrate obstacles. The refined path is deformed to resolve any collisions. Gayle and Lin [143] present a motion planning algorithm for simple closed robots that computes an approximate path between the initial and final configurations using the probabilistic roadmap method. Constraint-based planning is applied to make appropriate path adjustments and corrections to compute a collision-free path. The algorithm takes into account geometric constraints like non-penetration and physical constraints like volume preservation. In [144], a fast algorithm for collision detection between a deformable robot and fixed obstacles is used for path planning for a flexible robot in complex environments. The algorithm handles complex deformable models composed of tens of thousands of polygons.

Moll [145] approach path planning as a constrained minimization problem, where the planner is restricted to configurations that correspond to minimal-energy curves. The path planner computes paths from one minimal-energy curve to another such that all intermediate curves are also minimal-energy curves.

## 1.3 Challenges

The continued advancement of soft robotics depends on the development of novel soft sensors and actuators, soft robot designs with mobility and strength, models that enable design optimization and control, and fabrication techniques that organically grow active soft structures and interconnections. Active materials currently available for use in soft robotic manipulators have shortcomings that make their commercial use impractical. For instance, PAMs have a short fatigue life (~10,000 cycles) [46], most ionic EAPs can work only in aqueous media [47], conjugated polymers and ionic polymer-metal composites have short lifecycles due to creep and material degradation [61], electroactive polymer gels require very high voltage for actuation (up to 150MV/m) [56], and most actuators made of EAPs are not significantly scalable. New active materials are needed that provide the strain, stress, and speed for this challenging application. Materials research alone, however, will not produce material in sufficient quantities to develop macro-scale actuators. Material science and engineering is required to produce bulk quantities of high quality active material and to reliably fabricate high performance actuators and sensors.

With novel actuators available to the robot designer, new soft robots can, in principle, be designed that provide outstanding mobility, strength, and reliability. The design process, however, is complicated due to several competing and difficult to define design objectives. For example, there is often a trade-off between providing sufficient dexterity and maximizing load capacity, both of which are design objectives for soft robotic ma-

nipulators [2, 146]. There are many definitions of dexterity and load capacity and the final design may depend significantly on these definitions. Although soft manipulators are capable of performing a wide variety of tasks because of their flexibility, designing a manipulator that performs optimally for an entire range of tasks is a complicated problem.

To enable rapid virtual prototyping of soft robots, accurate physical models are needed. The design can be optimized prior to fabrication and accurately controlled based on these models. The underlying materials, geometry and actuators are nonlinear due to large strain and displacement and distributed due to the soft structure, complicating model development. Development of models that accurately simulate the operation of these robots based on the actuation inputs is a challenging multiphysics problem that can involve simultaneous analysis of solid and fluid mechanics, kinematics, electromechanics, thermodynamics and chemical kinetics of the processes involved. A greater understanding of these phenomena would facilitate the development of accurate models and lead to better design and control.

Sensing and controlling the shape and motion of soft robots is another problem that must be addressed rigorously. Soft robots theoretically have infinite degrees of freedom, but the number of sensors and actuators in any practical soft robot is finite. Therefore, many degrees of freedom of soft robots are not directly observable and/or controllable. Inverse dynamics models will be useful in the development of reliable feedforward control systems for soft robots.

An important issue in practice is user and operator interfaces for soft robots. User interfaces for soft robots are in their infancy. Soft robot structure and movements are quite different from those of humans, and human operators often become confused and disoriented. Although there has been some insightful early work in the area for soft manipulators, [147] there is a strong need for more focused efforts in human factors, as well as hardware and software design of operator feedback and input devices for soft robots.

The path planning approaches available for soft robots suffer from serious limitations, which make their practical use difficult at this time. Probabilistic methods tend to be computationally expensive because they require the generation of points in the configuration space, which grows exponentially with degrees of freedom. Available methods do not take into account the constraints imposed by the physical properties of the robots. Most planners work only in specific cases, and do not work on general deformable objects. Integrating motion planning with control and sensing is also an open problem.

Grasping objects using whole arm manipulation requires the grasp to be stable so that the arm does not undergo sudden changes in shape and drop the manipulated object. Robust path planning and control algorithms must ensure the stability of all intermediate configurations of the manipulator along the prescribed path. Extensive literature exists for grasp synthesis and stability analysis of rigid-link robots that contact objects only at finite points [148, 149, 150, 151, 152, 153, 154]. Stable grasp synthesis for highly com-

pliant and continuously deformable soft manipulators, however, will require solutions to many untouched and challenging design, control, and planning problems [155].

Fabrication of soft robots also poses several challenges. Traditional rigid connectors (*e.g.*, metallic fasteners) and electrodes cannot be used with soft structures so new ways to connect actuators both mechanically and electrically must be developed. The biologically inspiring examples in the plant and animal worlds have amazing fabrication systems that organically grow, repair, and maintain the structure, including interconnections. The development of novel fabrication methods that can replicate these dynamic biological processes would be a paradigm-shifting breakthrough in soft robotics.

## **1.4 Problem statement and research objective**

The objective of this research is to accurately model and understand the dynamics of soft robotic manipulators and to use this knowledge to generate rules for design and stable operation, workspace analysis, and to develop algorithms for shape estimation. At present, researchers use a constant curvature model for design and control of soft robotic manipulators. Experimental and theoretical results show that self-weight and other loading can cause significant deviations from constant curvature, leading to large tip position error. The mechanics of soft robotic manipulators is significantly affected by large extension, bending, shear and torsion so both material and geometric nonlinearities are important. Existing models for soft pneumatic extensors are either too simplistic to

give accurate results for large deformations and displacements, or are too complicated to be practically useful. Hence, they cannot be directly used with any dynamics model without compromising accuracy significantly. In absence of accurate models, design of these manipulators remains a trial and error process, and their control and stable operation ad hoc.

This thesis presents an approach for modeling the dynamics of soft robotic manipulators that incorporates the effect of material nonlinearities and distributed and payload weight and is geometrically exact for the large curvature, shear, torsion and extension. To take into account the material nonlinearities, we develop a simplified model for soft actuators using the work-energy principle that incorporates the nonlinearity of the membrane material and the mesh angle change. We use this model to generate optimal design taking into account the tradeoff between load capacity and flexibility. Shape estimation methods based on the model are developed and experimentally validated. The model is also used to analyze dexterity and manipulability of two designs of soft robotic manipulators. The workspaces of two designs of soft robotic manipulators are analyzed and compared.

## **1.5 Organization of this Thesis**

This thesis is organized as follows. In Chapter 2, the dynamic model of soft robotic manipulators is presented. In Chapter 3, this model is used for optimal design of pneumatic and hydraulic robotic manipulators. In Chapter 4, develops three methods for shape es-

timation for soft robotic manipulators based on the model, and Chapter 5 presents dexterity and manipulability analysis for two designs of soft robotic manipulators. Finally, Chapter 6 summarizes the conclusions of this research.

## Modeling of Soft Manipulators

This chapter derives a dynamic model for the OctArm soft robotic manipulator. First, previous research on modeling of pneumatic extensors and soft robotic manipulators is reviewed. Second, new models for pneumatic extensors and soft robotic manipulators are presented. Finally, the model is experimentally validated.

The structural mechanics of soft robot manipulators is complicated due to large extension, bending, shear and torsion so both material and geometric nonlinearities are important. This chapter presents a new approach for modeling the dynamics of soft robotic manipulators that incorporates the effect of material nonlinearities and distributed and payload weight and is geometrically exact for the large curvature, shear, torsion and extension that often occur in these manipulators. To take into account the material nonlinearities, we develop a simplified model for soft actuators using the work-energy principle that incorporates the nonlinearity of the membrane material and the mesh angle change. The dynamics of the manipulator is modeled using the special Cosserat

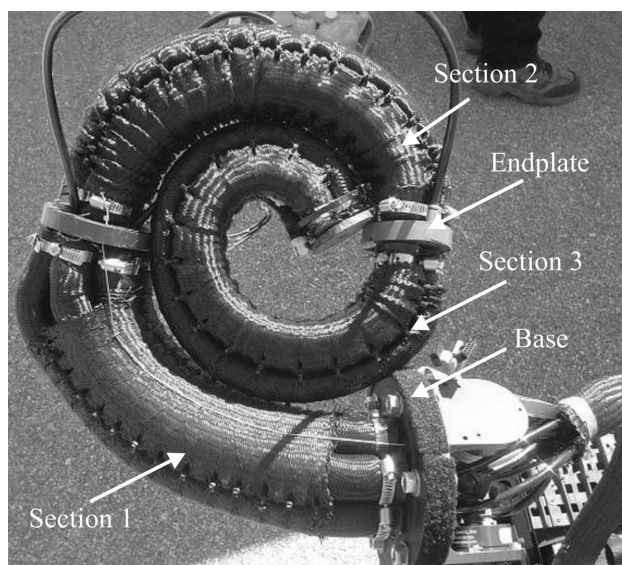


**Figure 2.1.** OctArm V in a maximally curved configuration.

theory of rods. The model is validated experimentally on the OctArm V manipulator (see Fig. 2.1), showing less than 5% average error for a wide range of actuation pressures and base orientations as compared to almost 50% average error for the constant curvature model previously used by researchers. Workspace plots generated from the model show the significant effects of self-weight on the OctArm V manipulator.

## 2.1 Previous research

### 2.1.1 Soft Actuator modeling

The actuators used in OctArm V (see Fig. 2.2) are closely related to McKibben actuators because both operate via pressurization of rubber tubes encased in a braided mesh sleeve. Many researchers have developed models for McKibben actuators using the

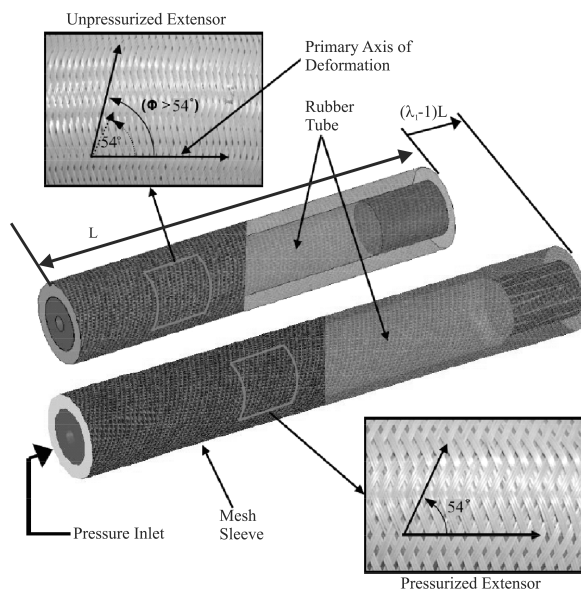


**Figure 2.2.** Extensor air muscle actuators extend when pressurized as the wind angle  $\alpha$  approaches  $54^\circ 44'$  from above.

work-energy principle. The most basic of these models assume the actuation process to be isobaric, the cylinder to be thin, and the deformation to be uniaxial, so that there is no deviation from the cylindrical initial shape. The pneumatic pressure extends the actuator length and contracts the actuator diameter. Constraints imposed by the fiber mesh are approximated using the pantograph opening principle [156]. Enhancements and corrections to this approach include incorporation of end distortion [157], friction between the mesh and the membrane [158] and fatigue characteristics [159]. These linear models, however, are only accurate for small deformations and cannot be used for applications involving large strain.

Another approach for actuator modeling involves calculating stresses in the membrane and the mesh from the applied pressure. Liu and Rahn [160] developed a fiber-

reinforced model for McKibben actuators by solving the force equilibrium equations. This model can predict the deformed actuator shape given the initial shape and the pressure and axial force inputs. Shan and Bakis [161] further refine the model to include the effects of extensible fibers. Reese *et al.* [162], use a nonlinear finite element formulation to model the anisotropically hyperelastic material behavior of fiber-reinforced pneumatic membranes. Bertetto and Ruggiu [163], use a commercial nonlinear finite element code to model a McKibben muscle as a Mooney Rivlin rubber tube and a linear tension bar element to incorporate the effects of the mesh. Although these models agree well with experimental results, they are too complicated to be incorporated into the manipulator model because they are computationally intensive.

### **2.1.2 Manipulator modeling**

The structural mechanics of continuum manipulators is complicated due to large extension and bending so both material and geometric nonlinearities are important. These manipulators are kinematically similar to hyper-redundant manipulators with extremely large degrees of freedom. Models that approximate continuum manipulators by finite d.o.f. hyper-redundant manipulators have been proposed. In this approach, accuracy and computational cost are proportional to the number of degrees of freedom used [98]. Many researchers [98], [99], [100] have followed the opposite approach: using a continuum approach to approximate the dynamics of hyper redundant manipulators. For instance, Mochiyama and Suzuki [101] have studied the kinematics and dynamics

of manipulators with hyper degrees of freedom by approximating them to continuum structures and using the Frenet-Serret formulas. However, for numerical simulation, they again approximate the robot backbone as a serial chain of rigid bodies with a large number of degrees of freedom. Previous researchers have also accounted for the geometric nonlinearities by assuming fixed shapes for robot backbone curves. Hirose [104] gives a planar model for snake robots based on a serpenoid curve. Hannan and Walker [107] assume that each section of the manipulator bends into a circular arc with constant curvature and an inextensible backbone. This assumption makes it possible to formulate the forward manipulator kinematics relating the position of the tip of the manipulator to the pressure inputs using a Denavit-Hartenberg formulation that fits a conceptual “virtual” rigid-link robot to the continuum backbone. Recent work by Jones and Walker [109][164] extends this approach by removing the assumption of an inextensible backbone. These methods rely, however, on the assumption of constant curvature which is valid only in cases when there are no external loads (including self-weight) on the manipulator. Gravagne *et al.* [110] study large deflection dynamics for planar continuum robots including the effects of actuator torques but without distributed loading. Self-weight and other loading can cause significant deviations from constant curvature, leading to large tip position error. Boyer *et al.*, [112], use the geometrically exact beam theory and the Newton-Euler technique to predict control torques of an eel-like robot as a function of expected internal deformations of an eel’s body.

## 2.2 Soft actuator model

Soft extensor actuators are the basic building blocks of the OctArm soft robotic manipulators. We develop a simplified model for these actuators using the work-energy principle that incorporates the nonlinearity of the membrane material and the mesh angle change. We assume that an internal pressure  $p$  is provided either pneumatically or hydraulically and the tube behaves as a Neo-Hookean solid. The strain energy per unit volume of the actuator can be expressed as a function of the first invariant of the Cauchy Green strain tensor,

$$I_1 = \lambda_1^2 + \lambda_2^2 + \lambda_3^2 \quad (2.1)$$

and the Young's modulus  $E$  as follows

$$u = \frac{E}{6}(I_1 - 3), \quad (2.2)$$

where  $\lambda_1$ ,  $\lambda_2$  and  $\lambda_3$  are the Cauchy Green strains. Incompressibility of the rubber implies [160]

$$\lambda_1^2 \cos^2 \alpha + \lambda_2^2 \sin^2 \alpha = 1. \quad (2.3)$$

Inextensibility of the fibers means

$$\lambda_3 = \frac{1}{\lambda_1 \lambda_2}. \quad (2.4)$$

The internal volume of the actuator,  $V$ , and the volume occupied by rubber,  $V_t$ , are

$$V = \pi L R_i^2 \lambda_1 \lambda_2^2, \quad V_t = A_t L, \quad (2.5)$$

where  $A_t = \pi(R_o^2 - R_i^2)$ . The total strain energy of the actuator and the work done by pressure,  $p$  are, respectively,

$$U = uV_t, \quad W = pV. \quad (2.6)$$

Using the principle of virtual work,

$$\delta U + \delta W = 0 \quad (2.7)$$

with

$$\delta U = \frac{EV_t}{6} \left( \begin{array}{l} 2\lambda_1 - 2\frac{\lambda_1 \cos^2 \alpha}{\sin^2 \alpha} - 2\frac{\sin^2 \alpha}{\lambda_1^3 (1 - \lambda_1^2 \cos^2 \alpha)} \\ + 2\frac{\sin^2 \alpha \cos^2 \alpha}{\lambda_1 (1 - \lambda_1^2 \cos^2 \alpha)^2} \end{array} \right) \delta \lambda_1 \quad (2.8)$$

and

$$\delta W = \left( p\pi R_i^2 L - 2\frac{p\pi R_i^2 L \lambda_1 \cos^2 \alpha}{\sqrt{1 - \lambda_1^2 \cos^2 \alpha} \sin \alpha} \right) \delta \lambda_1. \quad (2.9)$$

Eq. (2.7) is solved for pressure,

$$p = \frac{E \begin{pmatrix} \lambda_1^8 \cos^4 \alpha \cos 2\alpha - 2\lambda_1^6 \cos^2 \alpha \cos 2\alpha \\ + \lambda_1^4 \cos 2\alpha + 2\lambda_1^2 \cos^2 \alpha \cos 2\alpha \\ - \cos 2\alpha - 2\lambda_1^2 \cos^6 \alpha + \cos^4 \alpha \end{pmatrix} A_t}{3\lambda_1^3 (1 - 5\lambda_1^2 \cos^2 \alpha + 7\lambda_1^4 \cos^4 \alpha - 3\lambda_1^6 \cos^6 \alpha) A}. \quad (2.10)$$

This equation is numerically inverted (See Appendix A) to solve for  $\lambda_1$  given  $p$ . To maintain the nonlinear stress/strain relationship in Eq. (2.10) while using the linear material model discussed in the next section, we determine an equivalent axial force generated by internal pressurization of the tube,

$$F_i = EA_t \Delta\lambda_i, \quad i = I, II, III, \quad (2.11)$$

where

$$\Delta\lambda_i = (\lambda_{1,i} - 1), \quad i = I, II, III. \quad (2.12)$$

$\lambda_{1,i}$  is the axial strain of the *I*, *II* or *III* actuator groups as shown in Fig. 2.3.

## 2.3 Manipulator Model

### 2.3.1 Manipulator kinematics

Fig. 1.11 shows the displacement of the actuator backbone curve is defined by three vector-valued functions

$$\mathbf{r}(s,t) = x(s,t)\mathbf{i} + y(s,t)\mathbf{j} + z(s,t)\mathbf{k}, \quad \mathbf{d}_1(s,t), \mathbf{d}_2(s,t) \in \mathfrak{R}^3 \quad (2.13)$$

where orthonormal unit vectors  $\mathbf{d}_1(s,t)$  and  $\mathbf{d}_2(s,t)$  define the plane of the cross-section and  $\mathbf{r}(s,t)$  is the position of the material point on the axis with coordinate  $s$  at time  $t$  [165]. We set a third vector,  $\mathbf{d}_3(s,t)$  orthonormal to  $\mathbf{d}_1$  and  $\mathbf{d}_2$ , such that

$$\mathbf{d}_3 \equiv \mathbf{d}_1 \times \mathbf{d}_2. \quad (2.14)$$

The *director* vectors  $\{\mathbf{d}_k(s,t)\}$  form a right-handed orthonormal basis for  $\mathfrak{R}^3$ . Thus, there exist vector-valued functions  $\mathbf{u}$  and  $\mathbf{w}$  such that

$$\mathbf{d}_{k,s} \equiv \mathbf{u} \times \mathbf{d}_k, \quad \mathbf{d}_{k,t} \equiv \mathbf{w} \times \mathbf{d}_k, \quad (2.15)$$

where comma subscripts indicate partial differentiation. We decompose  $\mathbf{u}$ ,  $\mathbf{w}$  and the spatial derivative of vector  $\mathbf{r}$  with respect to this basis as

$$\mathbf{r}_{,s} = v_k \mathbf{d}_k, \quad \mathbf{u} = u_k \mathbf{d}_k, \quad \mathbf{w} = w_k \mathbf{d}_k, \quad (2.16)$$

where  $v_1$  and  $v_2$  are related to the components of shear strain of the backbone,  $v_3$  is a measure of axial strain,  $u_1$  and  $u_2$  are curvatures along  $\mathbf{d}_1$  and  $\mathbf{d}_2$ ,  $u_3$  is the torsion, and  $w_k$  denote the angular velocities along the three axes. The geometrical boundary conditions at the manipulator base ( $s = 0$ ) are

$$\mathbf{r}(0,t) = \mathbf{0}, \mathbf{d}_1(0,t) = \mathbf{d}_{10}, \mathbf{d}_2(0,t) = \mathbf{d}_{20}. \quad (2.17)$$

The director vectors are expressed as functions of quaternions. Using Eq. (2.16), the spatial derivatives of the Cartesian coordinates are related to the quaternions and strains

$$\begin{aligned} x_{,s} = & v_1(\beta_0^2 + \beta_1^2 - \beta_2^2 - \beta_3^2) + 2v_2(\beta_1\beta_2 - \beta_0\beta_3) \\ & + 2v_3(\beta_1\beta_3 + \beta_0\beta_2), \end{aligned} \quad (2.18)$$

$$\begin{aligned} y_{,s} = & 2v_1(\beta_1\beta_2 + \beta_0\beta_3) + v_2(\beta_0^2 - \beta_1^2 + \beta_2^2 - \beta_3^2) \\ & + 2v_3(\beta_2\beta_3 - \beta_0\beta_1), \end{aligned} \quad (2.19)$$

$$\begin{aligned} z_{,s} = & 2v_1(\beta_1\beta_3 - \beta_0\beta_2) + 2v_2(\beta_2\beta_3 + \beta_0\beta_1) \\ & + v_3(\beta_0^2 - \beta_1^2 - \beta_2^2 + \beta_3^2). \end{aligned} \quad (2.20)$$

Using Eq. (2.15), the spatial derivatives of the quaternions are related to the curvatures

$$2\beta_{0,s} = -\beta_1u_1 - \beta_2u_2 - \beta_3u_3, \quad (2.21)$$

$$2\beta_{1,s} = \beta_0u_1 - \beta_3u_2 + \beta_2u_3, \quad (2.22)$$

$$2\beta_{2,s} = \beta_3 u_1 + \beta_0 u_2 - \beta_1 u_3, \quad (2.23)$$

$$2\beta_{3,s} = -\beta_2 u_1 + \beta_1 u_2 + \beta_0 u_3. \quad (2.24)$$

### 2.3.1.1 Planar case

For planar motion (Fig. 3.1), we express the director vectors in terms of the cross section rotation angle  $\theta$ . Eqs. (2.18)-(2.20) simplify to

$$x_{,s} = v \cos \theta - \eta \sin \theta \quad (2.25)$$

and

$$y_{,s} = v \sin \theta + \eta \cos \theta. \quad (2.26)$$

where  $\eta = v_1$  and  $v = v_3$ . Eqs. (2.21)-(2.24) simplify to

$$\theta_{,s} = \mu. \quad (2.27)$$

where  $\mu = u_2$ .

## 2.3.2 Manipulator dynamics

The equilibrium equations for the pressurized manipulator sections are derived using Cosserat rod theory [165]. The equations of motion for each section of the manipulator

are

$$(\mathbf{n} - F_{ex}\mathbf{d}_3)_{,s} + \mathbf{f} = \rho A_t \mathbf{r}_{,tt} \quad (2.28)$$

$$\mathbf{m}_{,s} + \mathbf{r}_{,s} \times \mathbf{n} + \mathbf{l} = \mathbf{J}\mathbf{w}_{,t} \quad (2.29)$$

where  $\mathbf{f}$  is the external distributed load,  $\rho$  is the density of manipulator material,  $\mathbf{J}$  is the tensor of the second mass moments of inertia of the actuator cross section, and  $F_{ex}$  results from internal pressurization [166]. The stress ( $\mathbf{n}$ ) and moment ( $\mathbf{m}$ ) resultants are assumed to be proportional to strain and curvature respectively,

$$m_i = C_i u_i, \quad i = 1, 2, 3, \quad (2.30)$$

$$n_i = D_i v_i, \quad i = 1, 2, \quad n_3 = D_3(v_3 - 1), \quad (2.31)$$

where  $C_1 = EI_1, C_2 = EI_2, C_3 = GJ, D_1 = D_2 = GA_T$  and  $D_3 = EA_T$ . The principal components of the inertia tensor along  $\mathbf{d}_1, \mathbf{d}_2$  and  $\mathbf{d}_3$ , respectively, are

$$I_1 = I_2 = J/2 = N_t (I + A_t R_o^2/2) \quad (2.32)$$

and the total cross-section area  $A_T$  is

$$A_T = N_t A_t \quad (2.33)$$

where  $N_t$  is the number of extensors in the section.  $G$  is the shear modulus of the tube material. As  $G \rightarrow \infty$ , the shear deformation becomes negligible and the model reduces to an Euler-Bernoulli form.

In this research, we consider only static solutions to Eqs. (2.28)-(2.29), so  $\mathbf{r}_{,tt} = \mathbf{w}_{,t} = \mathbf{w} = 0$ . Eqs. (2.28)-(2.29) are decomposed with respect to the directors, and nondimensionalized using  $s^* = \frac{s}{L}$  and  $u^* = Lu$  to obtain the equations governing the curvatures, torsion and strains

$$u_{1,s} = \frac{(-\gamma_3 v_2 v_3 + \gamma_3 v_2 + k_2 u_2 u_3 - k_3 u_3 u_2 + v_3 \gamma_2 v_2)}{(k_1)}, \quad (2.34)$$

$$u_{2,s} = \frac{-(\gamma_1 v_3 v_1 - \gamma_3 v_1 v_3 - k_3 u_3 u_1 + k_1 u_1 u_3 + v_1 \gamma_3)}{(k_2)}, \quad (2.35)$$

$$u_{3,s} = \frac{(-\gamma_2 v_1 v_2 + \gamma_1 v_2 v_1 + k_1 u_1 u_2 - k_2 u_2 u_1)}{(k_3)}, \quad (2.36)$$

$$v_{1,s} = \frac{\begin{pmatrix} \gamma_3 u_2 - f_1 + \gamma_2 v_2 u_3 \\ -\gamma_3 u_2 v_3 + \pi u_2 \end{pmatrix}}{\gamma_1}, \quad (2.37)$$

$$v_{2,s} = -\frac{\begin{pmatrix} \gamma_1 v_1 u_3 + f_2 - \gamma_3 u_1 v_3 \\ +\gamma_3 u_1 + \pi u_1 \end{pmatrix}}{\gamma_2}, \quad (2.38)$$

$$v_{3,s} = \frac{(-\gamma_2 v_2 u_1 - f_3 + \gamma_1 v_1 u_2)}{\gamma_3}, \quad (2.39)$$

where

$$k_i = \frac{C_i}{L^2 D_1}, \gamma_i = D_i/D_1, \quad (2.40)$$

$$f_i = \rho A_t \mathbf{g} \cdot \mathbf{d}_i, \pi = \frac{F_{ex} \gamma_3}{D_3 k_1}, \quad (2.41)$$

and gravitational self-weight is assumed to be the only distributed external loading with  $\mathbf{g} = g\mathbf{j}$ , where  $g$  is the acceleration due to gravity. The following jump conditions hold across the section junctions

$$u_i(s^-) = \frac{u_i(s^+) \left(1 - \frac{\varepsilon_i}{2}\right) - M_i}{1 + \frac{\varepsilon_i}{2}}, \quad i = 1, 2, 3, \quad (2.42)$$

$$v_i(s^-) = \left(\frac{1 - \frac{\zeta}{2}}{1 + \frac{\zeta}{2}}\right) v_i(s^+), \quad i = 1, 2, \quad (2.43)$$

$$v_3(s^-) = \frac{v_3(s^+) \left(1 - \frac{\zeta}{2}\right) + \zeta}{1 + \frac{\zeta}{2}}, \quad (2.44)$$

where

$$\varepsilon_i = \frac{2(C_i(s^+) - C_i(s^-))}{C_i(s^+) + C_i(s^-)}, \quad (2.45)$$

$$\zeta_i = \frac{2(D_i(s^+) - D_i(s^-))}{D_i(s^+) + D_i(s^-)}. \quad (2.46)$$

The actuators apply a concentrated force and moment at the end of each section

$$F_{ex} = F_I + F_{II} + F_{III}, \quad (2.47)$$

and

$$\mathbf{M} = (F_I \mathbf{r}_I + F_{II} \mathbf{r}_{II} + F_{III} \mathbf{r}_{III}) \times \mathbf{d}_3(L) \quad (2.48)$$

where, the forces are defined in Eq. (2.11), and

$$\mathbf{r}_I = \delta_{N_t} \mathbf{d}_2(L), \quad (2.49)$$

$$\mathbf{r}_{II} = -\delta_{N_t} \left( \frac{\sqrt{3}}{2} \mathbf{d}_1(L) + \frac{1}{2} \mathbf{d}_2(L) \right), \quad (2.50)$$

$$\mathbf{r}_{III} = -\delta_{N_t} \left( \frac{\sqrt{3}}{2} \mathbf{d}_1(L) - \frac{1}{2} \mathbf{d}_2(L) \right), \quad (2.51)$$

with

$$\delta_{N_t} = \frac{R_o}{\sin(\pi/N_t)}. \quad (2.52)$$

Substitution of Eqs. (2.49)-(2.51) into Eq. (2.48) yields

$$\mathbf{M} = D_3 \delta_{N_t} \begin{pmatrix} (\Delta\lambda_{III} - \Delta\lambda_{II}) \mathbf{d}_1(L) + \\ (\Delta\lambda_{II} + \Delta\lambda_{III} - 2\Delta\lambda_I) \mathbf{d}_2(L) \end{pmatrix}. \quad (2.53)$$

The total point force at the end of each section is

$$\mathbf{F} = F_{ex} \mathbf{d}_3 + W \mathbf{g}, \quad (2.54)$$

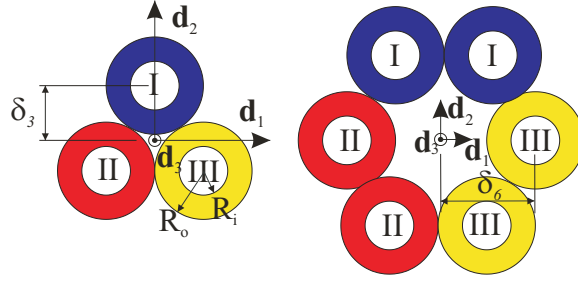


**Figure 2.3.** Cross-sectional view of six and three extensor manipulator sections showing three independent control channels (blue, red, and yellow).

where  $W$  is the weight of the section endplates and any additional loading.

### 2.3.2.1 Planar case

The manipulator can be operated in a plane by applying the same pressure to the control channels  $II$  and  $III$  so  $\Delta\lambda_{III} = \Delta\lambda_{II}$ . In this case, the nondimensional equilibrium equations simplify to

$$v_{,s} = \frac{1}{\gamma_3} \mu \eta + f_3, \quad (2.55)$$

$$\eta_{,s} = \gamma_3 \mu (\eta - 1) + k_1 \mu \pi - f_1, \quad (2.56)$$

$$\mu_{,s} = \frac{1}{k_1} (\gamma_3 - 1) \eta v - \frac{\gamma_3}{k_1} \eta - \pi \eta. \quad (2.57)$$

At section junctions, Eq. (2.42) for  $i = 2$ , Eq. (2.43) for  $i = 1$ , and Eq. (2.44) hold.

These jump conditions are related to the applied axial and transverse forces applied at the end of the section  $i$ ,  $F_{ia}$  and  $F_{ib}$  respectively, as follows,

$$\frac{D_{3,i-1}}{L_{i-1}} v_{i-1}^+ - \frac{D_{3,i}}{L_i} v_i^- = F_{ia}, \quad (2.58)$$

$$\frac{D_{1,i-1}}{L_{i-1}}\eta_{i-1}^+ - \frac{D_{1,i}}{L_i}\eta_i^- = F_{ib}, \quad (2.59)$$

$$\frac{C_{i-1}}{L_{i-1}^2}\mu_{i-1}^+ - \frac{C_i}{L_i^2}\mu_i^- = M_i, \quad (2.60)$$

$$(2.61)$$

where,  $v_i^+$ ,  $\eta_i^+$  and  $\mu_i^+$  are the values of  $v$ ,  $\eta$  and  $\mu$  at the end of section  $i$  respectively and  $v_i^-$ ,  $\eta_i^-$  and  $\mu_i^-$  are the values of  $v$ ,  $\eta$  and  $\mu$  at the beginning of section  $i$  respectively. The axial and transverse forces are

$$F_{ia} = D_3(\lambda_{II,i} + \lambda_{I,i} - 2) + W \sin \theta_i^+, \quad (2.62)$$

and

$$F_{ib} = -W \cos \theta_i^+, \quad (2.63)$$

respectively, where  $\theta_i^+$  is the value of  $\theta$  at the end of section  $i$ . The applied moment at the end of the section  $i$  is

$$M_i = D_3 \delta_{N_i} (\lambda_{II,i} - \lambda_{I,i}), \quad (2.64)$$

where  $\lambda_{II,i}$  and  $\lambda_{I,i}$  are the principal axial stretches, calculated from Eq. (2.10) for the double and single and control channels, respectively.  $L_i$  is the actuator length for section  $i$ . The free boundary condition at the end of the arm completes the set of equations.

## 2.4 Experimental validation

Fig. 2.4 shows the theoretically predicted and experimentally measured extension of four extensors with different area ratios and initial wind angles, for pressures ranging from 0 to 100 psi. The actuators are made from natural rubber tubing and Technoflex PET mesh. The theory from Eq. (2.10) overpredicts the measured actuator extension in Fig. 2.4. This is due to two effects. First, the mesh is not perfectly tight on the tube and the actuator does not extend until the pressure is sufficiently high to ensure that the tube is in contact with the mesh. Second, the model neglects friction between the mesh and the tube. These effects are also responsible for the small hysteresis.

The planar manipulator model is validated using the OctArm V manipulator and the parameters in Table 2.1.

The arm is actuated at pressures ranging from 30 to 90 psi in steps of 10 psi. Control channels *II* and *III* are actuated simultaneously to achieve planar motion. For each actuation pressure, there are 64 on/off permutations of the six actuator inputs. For each permutation at each pressure, the manipulator is photographed and the shape and tip position and measured. The experimental tip position measurement is compared to the constant curvature, infinite shear-stiffness, and full order models. The experiment is performed in both horizontal and vertical base orientation.

Fig. 2.5 shows example shape comparisons between the experiment and the three models. The constant curvature model neglects self-weight, causing poor agreement with the experimental results in most cases. Including self-weight vastly improves the

**Table 2.1.** Parameters of OctArm V

Section Number	Parameter	Value
1	$L$	25 cm
	$N_t$	6
2	$L$	28 cm
	$N_t$	3
3	$L$	30 cm
	$N_t$	3
1,2,3	$R_o$	14.0 mm
	$R_i$	9.3 mm
	$\rho$	1500 kg/m <sup>3</sup>
	$E$	2 MPa
	$G$	0.4 MPa
	$\alpha$	78°

model. The results are further improved by taking into account the shear strains, as is done in the full order model. The full order model outperforms the infinite shear stiffness and constant curvature models. The agreement between the full order model and the experiment however, also depends on the pressurization scenario. The examples shown in Fig. 2.5 vary from good (a) to fair (b) to poor (c) agreement for both vertical and horizontal base orientations.

Fig. 2.6 plots the average error for all three models over the 64 permutations versus pressure for horizontal and vertical base orientation. These plots show that the model accuracy increases from the constant curvature model (tip error  $\approx 60$  cm  $\approx L/2$ ), to the infinite shear stiffness model (tip error  $\approx 10$  cm  $\approx L/10$ ) to the full order model (tip error  $\approx 5$  cm  $\approx L/20$ ) for both base orientations.

The workspaces shown in Figs. 2.7 and 2.8 are generated by plotting tip position of the manipulator for all 117,649 permutations of input pressure ranging from 0 to 100 psi

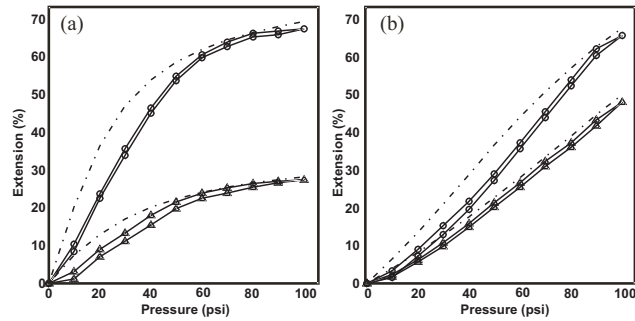


**Figure 2.4.** Comparison of experimental (solid) and theoretical (dash-dotted) extension of pneumatic air muscles with applied pressure for (a)  $A_t/A = 0.373$ ,  $\alpha = 65^\circ$  (O),  $A_t/A = 0.195$ ,  $\alpha = 71^\circ$  ( $\Delta$ ); (b)  $A_t/A = 1.126$ ,  $\alpha = 78^\circ$  (O),  $A_t/A = 0.682$ ,  $\alpha = 76^\circ$  ( $\Delta$ ).

(7 steps) on the six control channels. Fig. 2.7 shows the workspace for the manipulator with a vertical base orientation. The top inset shows a fairly uniform cardioid distribution without gravitational loading. The main figure shows that gravitational loading reduces the reachability above the horizontal axis. Adding a 0.25 kg load to the tip results in even lower reachability above the horizontal axis as shown in the workspace plot in the bottom inset. Fig. 2.8 shows the horizontal base orientation case. Without gravitational loading the top inset is simply the top inset of Fig. 2.7 rotated by  $90^\circ$ . Gravitational loading and added weight shown in the main plot and the bottom inset, respectively, lower the workspace. Table 2.2 shows that the mean values of the vertical tip position over the entire workspace shift down by 0.248 m, 0.351 m and 0.445 m due to gravitational loading at  $0^\circ$ ,  $45^\circ$  and  $90^\circ$  respectively.

**Table 2.2.** Mean values of manipulator tip position over the workspace.

Base Orientation	Const. curvature	Full order	Difference
$0^\circ$	-0.485	-0.733	0.248
$45^\circ$	-0.343	-0.694	0.351
$90^\circ$	0	-0.445	0.445

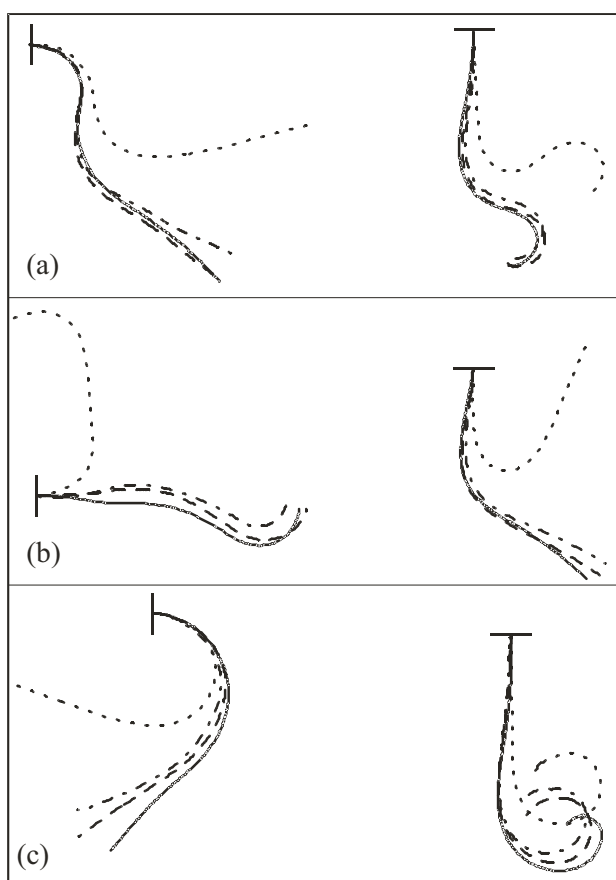


**Figure 2.5.** Experimental (solid) and constant curvature model (dotted), infinite shear modulus model (dash-dotted), and full order model (dashed) backbone curves for horizontal (left) and vertical (right) base orientations: (a) good, (b) fair, and (c) poor agreement between full order model and experiment.

## 2.5 Conclusions

The constant-curvature models used by previous researchers to predict the shape of soft robot manipulators can be quite inaccurate due to their neglect of gravitational loading.

The nonlinear extension actuator and Cosserat rod models presented in this paper are an order of magnitude more accurate than the constant curvature model for the OctArm V manipulator. Gravitational loading significantly lowers the manipulator workspace,

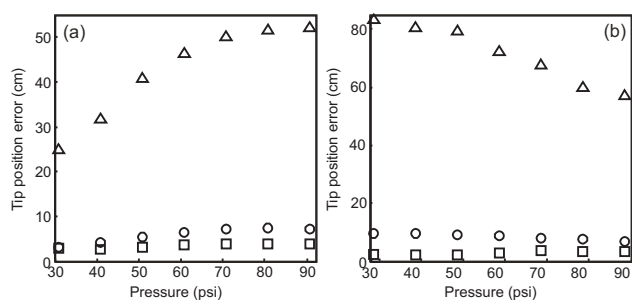


**Figure 2.6.** Average tip position error between models and experiments (64 test cases) versus actuation pressure in: (a) vertical and (b) horizontal base orientation for constant curvature ( $\Delta$ ), infinite shear modulus (O) and full order ( $\square$ ) models.

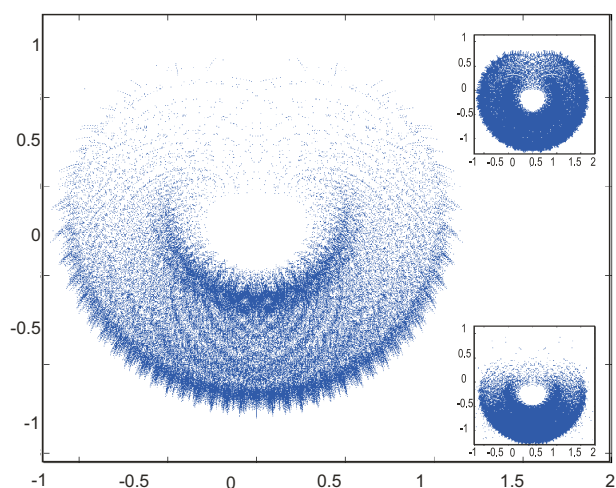


**Figure 2.7.** OctArm V workspace with self-weight (main), without loading (top inset), and with self weight and a 0.25 kg payload (bottom inset) in vertical base orientation.

especially with added payload weight. Further improving the match between theory and experiment can best be achieved by improving the OctArm fabrication process. In particular, the model is very sensitive to wind angle, which varies within each actuator and from actuator to actuator.

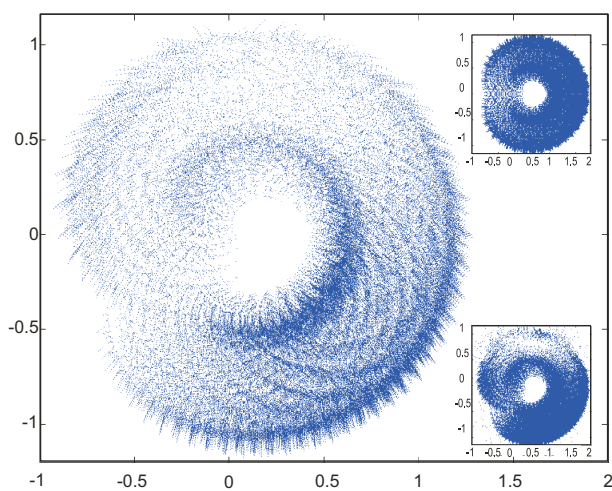


**Figure 2.8.** OctArm V workspace with self-weight (main), without loading (top inset), and with self weight and a 0.25 kg payload (bottom inset) in horizontal base orientation.

## Model-based design optimization

The design objectives for soft robotic manipulators are to provide a certain level of dexterity while maximizing load capacity for a given maximum pressure  $p_{\max}$ . The load capacity ( $W$ ) of the arm is defined as the heaviest load on the arm tip that an arm with  $90^\circ$  base orientation can bring to horizontal by pressurization at a test pressure  $p_{\text{test}}$ , as shown in Fig. 3.1. The test pressure is chosen to provide sufficient lift but not be so large as to cause numerical problems in the solver. In practice, the design complexity and air consumption also play a role in arm design.

Design of OctArm soft robotic manipulators requires specification of the extensor actuators and the configuration and number of sections. The design parameters for the extensor actuators are the outer diameter  $R_o$ , thickness  $t$ , length  $L$ , and initial mesh angle  $\alpha$ . We assume that all of the extensors in the manipulator use the same tubes ( $R_o$ ,  $t$ ) and meshes ( $\alpha$ ) for ease of fabrication. The initial mesh angle is chosen to be the maximum possible using the OctArm fabrication process ( $\alpha = 78^\circ$  for all cases in this analysis).

We restrict our optimization to sections with 3, 6, 9, or 12 actuators and all actuators in a given section centered about vertices of a regular polygon and touching each other (see Fig. 3.3). Thus we have  $2 + N$  continuous variables for the extensor actuators ( $R_o, t, L_1, \dots, L_N$ ) and  $N$  discrete variables for the actuator configuration in each section. The design variables are written in vector form as

$$\mathbf{x} = [R_o, t, L_1, L_2, \dots, L_N, N_{t,1}, N_{t,2}, \dots, N_{t,N}]^T. \quad (3.1)$$

### 3.1 Dexterity Template

Based on the ability of the robot to manipulate objects of different sizes, we propose the dexterity template shown in Fig. 3.2. In this template, the distal section is assumed to wrap completely around an object for a wrap angle of  $360^\circ$ . The third and second sections together are designed to wrap completely around a bigger object, resulting in a  $180^\circ$  wrap requirement for section 2. Finally, the proximal or base section works with the two other sections to completely wrap around an even larger object, requiring  $120^\circ$  of wrap angle for section 1. The general formula for the wrap angles  $\Theta_i$  of an  $N$  section robot is

$$\Theta_i = \frac{360^\circ}{N - i + 1}. \quad (3.2)$$

If we know all of the extensor parameters except the length and the section configurations, then we can calculate the section lengths required to provide the wrap angle

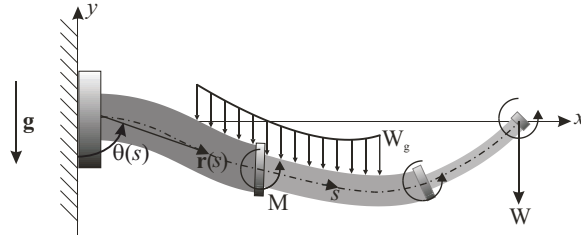


**Figure 3.1.** Soft robotic manipulator model. The load capacity is defined as the maximum load that the arm can lift to  $y = 0$  at the test pressure  $p_{test}$ .

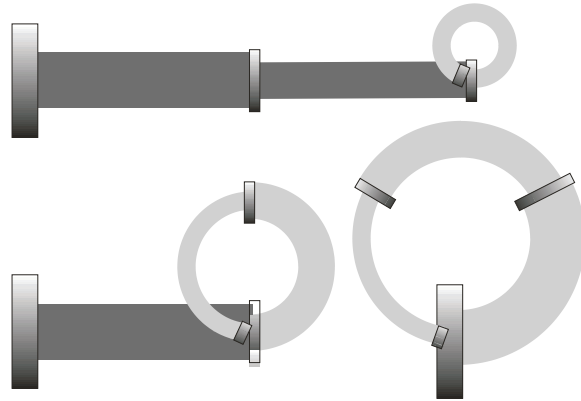


**Figure 3.2.** Sections 1, 2, and 3 of a three section robot are designed to have 360, 180, and 120 degree wrap angles, respectively, to provide the desired dexterity.

conditions given by Eq. (3.2) as follows

$$L_i = \frac{\Theta_i}{M_{i,max}/EI_i}, \quad (3.3)$$

where  $M_{i,max}$  is the actuating moment at a pressure  $p_{max}$  calculated from Eqs. (2.64) and (2.10). Transverse forces due to gravity can increase or decrease the wrap angle depending on the arm configuration so loading effects are neglected in the length calculation to reduce the complexity of the optimization. The overall length of the manipulator,  $L$ , is typically known, so tube thickness  $t$  and section lengths  $L_i$  are constrained by Eq. (3.3).

## 3.2 Problem formulation

The objective of design optimization is to maximize the load capacity,  $W$ , while meeting certain design constraints pertaining to dexterity (see Section 4.1), tube outer diameter ( $R_o$ ) and thickness ( $t$ ). In order to have the desired workspace, the manipulator is required to have total length  $L$ . Symmetrical operation in 3D actuation is achieved by restricting the number of actuators in each section to multiples of 3, *i.e.*, 3, 6, 9 or 12.

The objective function for the optimization problem can be thus formulated as

$$\text{minimize } f(\mathbf{x}) = -W, \quad (3.4)$$

subject to the inequality constraints

$$R_o = x_1 < R_{o,\max}, \quad (3.5)$$

$$-R_o = -x_1 < -R_{o,\min}, \quad (3.6)$$

$$-t = -x_2 < 0, \quad (3.7)$$

and the equality constraints

$$y(1; \mathbf{x}, W) = 0, \quad (3.8)$$

$$\sum_{i=3}^{N+2} x_i - L = 0, \quad (3.9)$$

$$x_{i+2} - \frac{\Theta_i}{M_{i,\max}/EI_i} = 0, \quad i = 1..N, \quad (3.10)$$

where  $y(1; \mathbf{x}, W)$ , the vertical location of the manipulator tip, is obtained by solving Eq. (2.26) and the stiffness

$$EI_i = x_{N+i+2} \frac{\pi}{2} \left( \begin{array}{l} \frac{1}{2} \left( x_1^4 - (x_1 - x_2)^4 \right) + \\ x_1^2 \left( x_1^2 - (x_1 - x_2)^2 \right) \end{array} \right) \quad (3.11)$$

subject to

$$x_{N+i+2} \in \{3, 6, 9, 12\}, \quad i = 1..N \quad (3.12)$$

Solving Eqs. (3.9)-(3.10) leaves only the outer radius  $x_1$  and the actuator configurations  $x_{N+i+2}$  as independent variables for the search algorithm.

### 3.3 Optimization Method

The design variables  $N_{t,i}$  govern the the number of tubes in each section. The presence of these discrete variables rule out the use of gradient-based methods for optimization and suggests the use of genetic algorithms. The internal and external radii are continuous variables, but commercial availability of only certain tube diameters implies that these are also discrete variables. Thus, a genetic algorithm is used to search for the outer radius and actuator configuration that maximize arm load capacity. To determine load capacity, we fully actuate the two actuator control channels of each section to a test pressure  $p_{test}$ . This is typically lower than the maximum pressure because application of the maximum test pressure causes severely nonlinear behavior and the algorithm has

convergence problems.

After extensive testing of the optimization algorithm with a variety of model parameters, it is found that the optimal designs have several common features that can be used to simplify the optimization process. For a given number of sections, overall length, tube material, and dexterity template, the tube thickness and section lengths are calculated using Eqs. (3.3) and (3.9). The only variables that remain to be optimized are the tube diameter and the actuator configurations in each section. We notice that constraints on maximum outer tube diameter and minimum tube thickness are always active, so optimal designs have thin-walled tubes. This thin-walled tube solution has minimal weight with maximal stiffness and moment so the load capacity is maximized. The solution suggests that we can fix the outer diameter to its maximum practical value in one of the following ways: fixed arm diameter, fixed tube diameter, fixed aspect ratio, and fixed gripping radius. This assignment effectively eliminates tube diameter as a variable, and the optimization problem can be solved by an exhaustive search in the design space, which contains  $2^{N-1}$  candidate solutions associated with the tube configurations. In the following, we examine the fixed aspect ratio case in detail. Results from the other cases can be found in Appendix B.

The nondimensional Eqs. (2.55)-(2.57) show that the internal pressure is everywhere divided by the Young's modulus. Thus, if we find an optimal design for a given test pressure and Young's modulus then any arm that has the same  $p_{\max}/E$  ratio will have the same design. The load capacity will be larger, however, for the design with larger

**Table 3.1.** Design parameters for pneumatic and hydraulic soft robot manipulators

<b>Design Parameter</b>	<b>Pneumatic Design</b>	<b>Hydraulic Design</b>
$E$	1.2 MPa	12 MPa
$\rho$	1500 kg/m <sup>3</sup>	1500 kg/m <sup>3</sup>
$\alpha$	78°	78°
$R_o$	15 mm	15 mm
$L$	1 m	1 m
$p_{test}$	0.14 MPa	1.4 MPa
$p_{max}$	0.7 MPa	7 MPa
$\beta$	0.09	0.09

$p_{max}$ .

### 3.4 Optimization Test Cases

To study the optimal design of soft robotic manipulators, we choose the pneumatic and hydraulic test cases shown in Table 3.1 with various constraints applied to the design, as described in this section. The effect of number of sections and the stiffness of the tube material is also studied.

#### 3.4.1 Fixed Aspect Ratio Case

In this case, either the tube diameter is proportional to the length,  $R_o = \beta L$ , or the base diameter  $R_b = \beta L$ . Fig. 3.3 shows example base configurations for these two cases. If the tube diameter is constrained then the base diameter depends upon configuration as shown in Fig. 3.3(a). If the base diameter is constrained, then the tube diameter changes based on the base section configuration (see Fig. 3.3(b)).

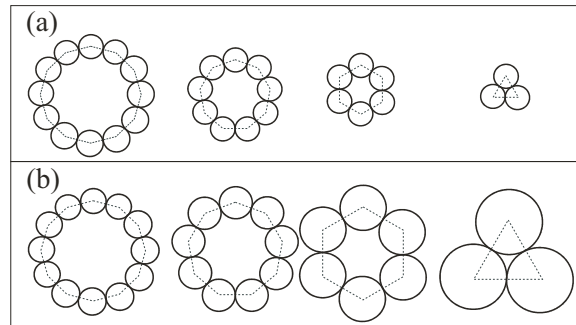


**Figure 3.3.** Base section configurations for (a) fixed tube diameter ratio and (b) fixed base diameter ratio.

The pneumatic system is based on OctArm VI and uses natural rubber tubing, the maximum mesh angle, and a maximum pressure typical of pneumatic systems. The hydraulic test case has the same parameters as the pneumatic case except an order of magnitude higher tubing stiffness (silicone) and maximum pressure are used. In addition, hydraulic tubes are filled with water ( $\rho = 1000\text{kg/m}^3$ ), adding to the arm weight. The test pressure in both cases is taken as 20% of the maximum pressure. Note that the  $p_{\max}/E$  ratios are the same for both the hydraulic and pneumatic systems so the optimal tube thickness and actuator configurations will be similar. The optimal designs will not be identical, however, due to the added self-weight of water in the hydraulic design.

### 3.4.2 Fixed Tube Diameter

If the ratio between tube diameter and manipulator length is fixed, the load capacity of the manipulator first increases with length and then decreases, as shown in Fig. 3.4. The optimal design represents a trade-off between actuating moment and load moment arm. For small arm lengths, the actuating moment given by Eq. (2.64) and the bending

moment due to self-weight are small. As the manipulator is scaled up the actuating moment grows faster than the load moment arm. For lengths greater than optimal, however, the long moment arm outweighs the actuation moment. As the number of sections increases from two to five, the optimal length and load capacity increase from 1.1 m to 2.0 m and 50 N to 190 N respectively.

The inset plots in Figs. 3.4 and 3.5 show the shape of the optimal arms at different lengths. The tubes in the arm all have the same diameter, so the overall section diameter depends on the actuator configuration. Considering the three section arm (dash-dotted curve), short arms have sections with twelve actuators each (12-12-12). The configuration changes from (12-12-12) to (12-12-9) to (12-12-6) to (12-9-6) to (12-9-3) as the length increases. The load capacity peaks at 90 N for a length of 1.4 m and a configuration of (12-12-9). Note that this is the load capacity at the test pressure, 20% of the maximum pressure, so the actual load capacity can be much larger. At lengths above 2.25 m, the arm can no longer hold its own weight.

Figure 3.5 shows a similar trend with the hydraulic test case except the optimal arm lengths are longer and the load capacities are higher. The optimal configuration has 12 tubes in all sections for short length, and become increasingly tapered as the length increases. For example, a 5-section hydraulic actuator of length 3 m has a configuration of 12-12-9-9-6. Hydraulic arms can also be longer than pneumatic arms and have a positive load capacity.

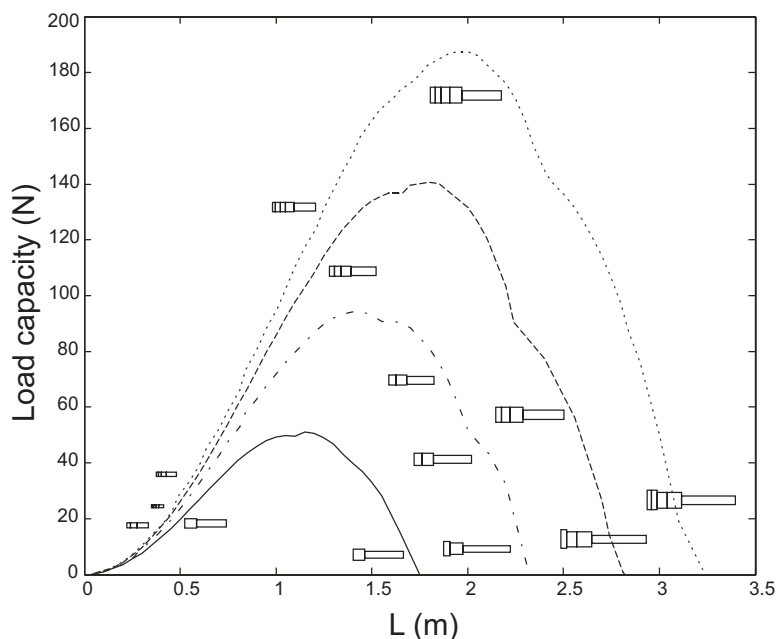


**Figure 3.4.** Load capacity versus arm length for optimal pneumatic two section (solid), three section (dashed), four section (dash-dotted) and five section (dotted) arms for a fixed tube diameter ratio.

### 3.4.3 Base Diameter Ratio

If the base diameter is constrained, the overall load capacity trends remain the same (see Figs. B.5-B.6). However, the optimal solutions have 3 tubes in all sections for short length. At longer lengths, there is a transition to (6-6-...-6-3) in the hydraulic case. In the pneumatic case, this transition does not occur. However, at lengths near the optimal, the load capacity of the (6-...-6-3) configuration is close to that of (3-3-...-3) configurations. For example, for three sections, the optimal solution has a configuration of (3-3-3), with a length of 0.8 m, and a load capacity of 1.2 N. A (6-6-3) configuration with the same length has a load capacity of about 1 N. However, the (3-3-3) configuration requires pressurization of 1.75 liters of internal volume, compared to the 1.01

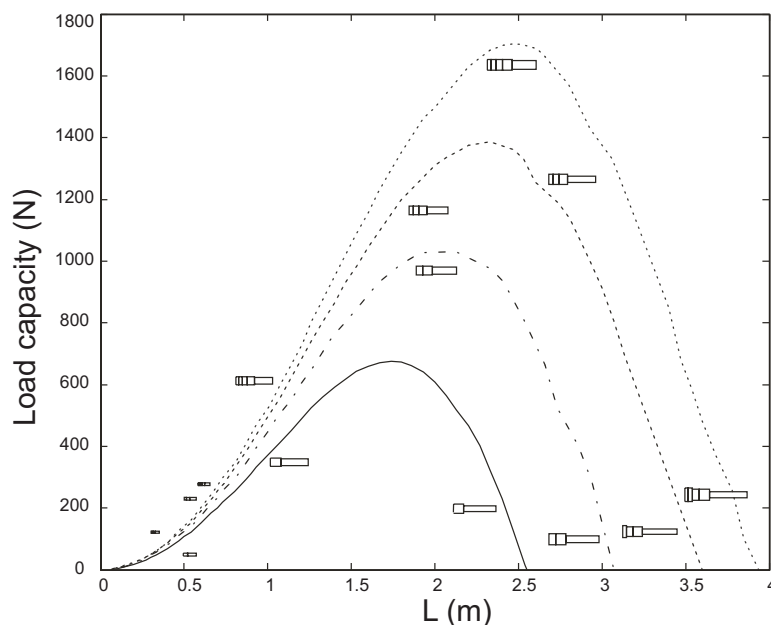


**Figure 3.5.** Load capacity versus arm length for optimal hydraulic two section (solid), three section (dashed), four section (dash-dotted) and five section (dotted) arms, for a fixed tube diameter ratio.

liters of internal volume of the (6-6-3) design. The reduced volume results in less air pumping and higher energy efficiency. Thus, the OctArm VI design of 0.87 m and a configuration of (6-6-3) is close to optimal in terms of load capacity, while having a better energy efficiency.

### 3.4.4 Effect of number of sections

Figure 3.6 shows the optimal pneumatic designs versus number of sections in a one meter long manipulator with (base diameter/length = 0.09). The load capacity at  $p_{test}$  and tube thickness  $t$  are plotted. The load capacity increases quickly at low number of sections and continues to grow up to the maximum of eight sections shown on the

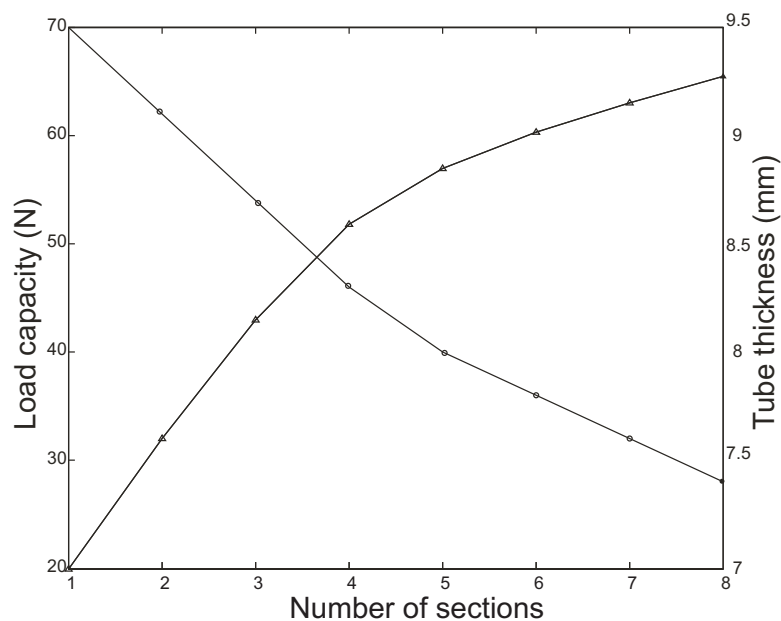


**Figure 3.6.** Hydraulic test case showing load capacity (triangles) and tube thickness (circles) as a function of number of sections.

plot. The configuration remains 3-tube per section for a length of one meter regardless of the number of sections. Increasing the number of sections increases dexterity and load capacity but results in an arm that is more complicated and expensive.

### 3.4.5 Effect of tube stiffness

Figure 3.7 shows how the load capacity and tube thickness change for the optimal three section hydraulic arm with increasing  $E$ . There is no optimal peak in the curve because as the tube becomes stiffer, the thickness becomes smaller. In the limit of infinite  $E$ , the tube thickness and self-weight go to zero and the load capacity asymptotically approaches a maximum value.

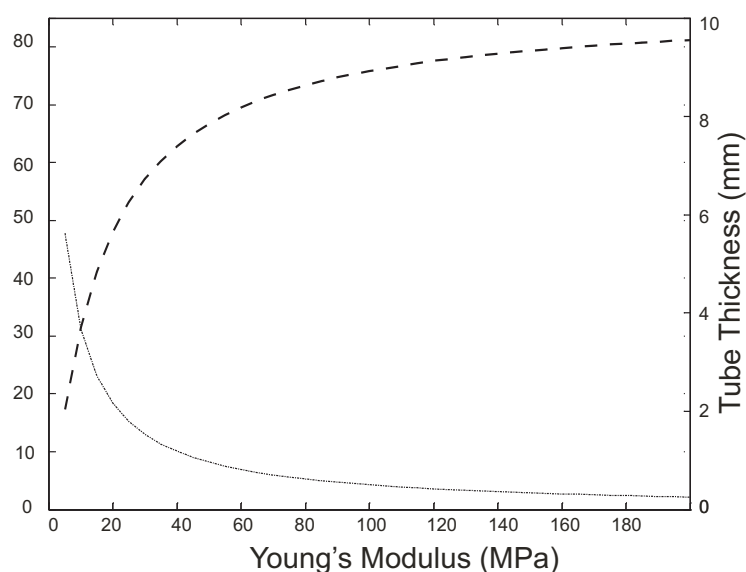


**Figure 3.7.** Load capacity (dashed) and tube thickness (solid) for the optimal three section hydraulic arm versus Young's modulus.

### 3.5 Conclusions

The design of OctArm soft robotic manipulators requires specification of a dexterity template with given wrap angles for each section. Then, for any given configuration of the manipulator, the tube thickness and section lengths can be calculated to provide the desired overall base diameter and total length. The actuator configuration depends upon the length of arm, and can be optimized to maximize load capacity. The optimal design depends on the  $p_{\max}/E$  ratio so a single optimal design exists for a family of constant  $p_{\max}/E$  manipulators. As the number of sections increases, the complexity of design and fabrication, dexterity, and load capacity increase, creating a trade-off between cost and performance. There are some limitations in the design approach presented in this thesis. First, the objective function maximizes the load capacity for a certain test pres-

sure, which may not lead to optimal performance for all pressures and loading conditions. Second, elastic stability, out-of-plane deformations and torsion are not addressed. Finally, inaccuracies in the manipulator model are reflected in the optimal design.

# Model-based shape estimation

## 4.1 Introduction

In traditional hard robots, the end effector is localized by measuring the position of each joint with a high resolution encoder as shown in Figure 1.1(a). Assuming rigid links, the joint positions can be processed by the forward kinematics to accurately determine the shape and tip position of the robot. Similarly, the inverse kinematics can be used to determine the joint positions that provide a desired tip position. The joint positions measured by the encoders are compared to the desired positions calculated from the inverse kinematics and the actuators then servo the errors to zero. This servo action is typically quite fast and forces the joints to precisely track their desired positions. The environment applies loads to the structure either through distributed loading (*e.g.*, gravity) or by contact. In a rigid-linked robot, Figure 1.1(d) shows that loading causes the soft joints to change position while the rigid links remain straight. The encoders

measure the position change and the controller can either compensate for the loading or understand that the robot has contacted the surroundings. In either case, the shape and tip position can be exactly determined.

Soft robots interact with the environment differently from their hard counterparts. They have a continuum structure instead of well defined joints, and they articulate by means of material compliance. Gravity and contact loading cause continuous deformation in a soft robot that may not be observable or controllable from the limited number of sensors or actuators, respectively. This motivates the development of techniques for estimating the shape of the manipulator using a finite number of measurements.

One common approach to shape estimation for continuum manipulators is strain measurement along the manipulator axis, either by surface attaching sensors to the structure or by embedding them in the structural material [167, 168]. Dynamical models of the manipulator are then used to predict the shape of the manipulator based on the strain measurements. This approach often suffers from issues of scalability and modeling inaccuracies [169]. Additionally, fiber optic sensors [170, 171, 172, 173, 174] exhibit propagation losses when they are bent. Typically, these losses rise very quickly once a certain critical curvature is reached [175].

Another approach to measure the shape of flexible structure is to use vision. Hannan and Walker [124] use a single high-speed camera to track distinct bands on a planar continuum manipulator and estimate curvatures for each section. This method assumes constant curvatures, which can be inaccurate if nonlinear, large deformation, and grav-

itational loading effects are present [176]. Chitrakaran *et al.* [123] extend this method to 3-D by tracking coplanar points on a continuum manipulator using a single camera and determining the pose of that plane by exploiting its projective homography relative to a reference plane. Matsuno *et al.* [177] make this approach more robust using a three-camera system that eliminates the difficulties caused by occultations. A major disadvantage of vision-based systems is the requirement for cameras, limiting applications.

This chapter presents three shape-estimation methods for soft robotic manipulators based on a geometrically-exact dynamic model. The manipulator model is based on Cosserat rod theory, accounts for large curvatures, extensions, and shear strains, and is coupled to a nonlinear constitutive model for the actuator. OctArm VI, an elephant trunk manipulator is used as an example to demonstrate the methods [2, 178].

The details of the models used for developing the shape estimation methods are given in Chapter 2.

## 4.2 Shape Estimation Techniques

Table 4.1 summarizes the four shape estimation techniques studied. First, one can use the model presented in the Chapter 2. All of the model parameters must be known and the boundary conditions, including the base orientation and payload mass. Thus, at least one inclinometer is required at the base.

The load cell method requires exact knowledge of fewer parameters but requires a 3-axis load cell and inclinometer at the base. The payload mass is not required to

**Table 4.1.** Summary of the shape estimation methods for a three section manipulator in planar operation

Method	Sensors	Known parameters	Known payload	Algorithm complexity
Load cell	6-axis load cell and inclinometer at base	$L, EA_t, GA_t, W_g, EI, p, \alpha$	No	First order initial value problem in $\eta, v$ and $\mu$ .
Inclinometer	Inclinometers at base and each endplate	$L, w/g, a, g, \alpha, p$	Yes (3 inclinometers), No (4 inclinometers)	Third order boundary value problem in $\theta$ .
Encoders	Inclinometer at base, two cable encoders	$L, R, w/g, a, g, p, \alpha$	No, but improves accuracy.	Third order boundary value problem in $\theta$ .
Model	Inclinometer at base	$L, \gamma, k, EI, EA_t, GA_t, p, \alpha$	Yes	First order boundary value problem in $\eta, v$ and $\mu$ .

be known. The inclinometer method has similar model knowledge requirements but inclinometers are mounted at the base and the end of each section. The final method uses two cable encoders in each section.

#### 4.2.1 Shape Estimation using Load Cells

In this approach (Fig. 4.1), the two-point boundary value problem given by Eqs. (2.55)-(2.57) is converted to an initial value problem that can be numerically integrated. The “initial” conditions at  $s = 0$  are obtained from a six-axis force/torque sensor mounted at the manipulator base that measures the axial ( $v_0$ ) and shear ( $\eta_0$ ) forces and moment ( $M_0$ ) on the manipulator. An inclinometer measures the base orientation ( $\theta_0$ ). The initial

conditions are

$$v(0) = v_0, \eta(0) = \eta_0, \mu(0) = \mu_0, \quad (4.1)$$

$$x(0) = 0, y(0) = 0, \theta(0) = \theta_0. \quad (4.2)$$

The manipulator tip position is then found by integrating the equilibrium equations from  $s = 0$  to  $s = L$ . Assuming perfect sensing and model, this estimation method gives the exact shape of the manipulator. The method requires three sensors for the planar problem that measure axial and transverse load and base orientation. Integration of the governing equations (Eqs. (2.55) -(2.57)) requires knowledge of all parameters:  $L$ ,  $EA_t$ ,  $GA_t$ ,  $W_g$  and  $EI$ . In addition, the actuator parameters in Eq (2.10) must also be known. An unknown point mass that is attached to the tip can be accommodated by subtracting known arm weight from the load measured at the base.

In practice, the accuracy of the tip position depends on the accuracies of the measurements. Robust shape measurement requires low sensitivity to sensor noise. The sensitivity of tip position estimation is obtained by taking derivatives of the field equations with respect to the measurements

$$\psi_{1i,s} = g\eta\psi_{3i} + g\mu\psi_{2i} + w\cos\theta\psi_{6i} \quad (4.3)$$

$$\psi_{2i,s} = \left( \frac{1}{g}(v-1) + \frac{\pi}{ag} \right) \psi_{3i} + \frac{\mu}{g}\psi_{2i} - \frac{w}{g}\sin\theta\psi_{6i} \quad (4.4)$$

$$\psi_{3i,s} = (a(1-g)v - a - \pi)\psi_{2i} + a(1-g)\eta\psi_{1i} \quad (4.5)$$

$$\psi_{4i,s} = \psi_{1i} \cos \theta - \psi_{2i} \sin \theta - (v \sin \theta + \eta \cos \theta) \psi_{6i} \quad (4.6)$$

$$\psi_{5i,s} = \psi_{1i} \sin \theta + \psi_{2i} \cos \theta + (v \cos \theta - \eta \sin \theta) \psi_{6i} \quad (4.7)$$

$$\psi_{6i,s} = \psi_{3i} \quad (4.8)$$

where

$$1 \leq i \leq 6, \quad (4.9)$$

$$\psi_{ij} = \frac{\partial \chi_i}{\partial \chi_j(0)} \quad (4.10)$$

and

$$\chi = [v, \eta, \mu, x, y, \theta]^T. \quad (4.11)$$

The initial conditions are  $\psi_{ij}(0) = \delta_{ij}$ , the Kronecker delta. Jump conditions for  $\psi_{ij}$  between the sections are similarly derived by differentiating the jump conditions for the field variables (Eqs. 2.64 - 2.63).

The maximum error in the tip position is

$$E = \sqrt{\sum_{i=1}^6 \Delta \chi_i \left( (\psi_{4i}(1))^2 + (\psi_{5i}(1))^2 \right)}, \quad (4.12)$$

where  $\Delta \chi_i$  are the sensing errors of  $\chi_i(0)$ .

### 4.2.2 Shape Estimation using Encoders

In this method (See Fig. 4.2), cable encoders are mounted along the length of the manipulator at chosen circumferential locations and an inclinometer measures the orientation of the base. Manipulator bending and extension change the length of the encoder cables. These measurements are used to estimate the shape of the manipulator.

The extension of each section is assumed to be caused purely by pressurization, neglecting the effects of external loading. Under these assumptions, Eqs. (2.55) - (2.57) become

$$\eta_{,s} = c_1 \mu + \frac{w}{g} \cos \theta, \quad (4.13)$$

$$\mu_{,s} = c_2 \eta, \quad (4.14)$$

where

$$c_1 = \frac{1}{g} (\nu - 1) + \frac{\pi}{ag}, \quad (4.15)$$

$$c_2 = a(1 - g)\nu - a - \pi. \quad (4.16)$$

Differentiating Eq. (4.14) and substituting Eq. (4.13) and Eq. (2.27), we get

$$\theta_{,sss} = c_2 \left( c_1 \theta_{,s} + \frac{w}{g} \cos \theta \right). \quad (4.17)$$

This third order ordinary differential equation is solved by measuring three boundary conditions in  $\theta$  using the cable encoders and the inclinometer.

To obtain the boundary conditions, we find the extension of the encoders for an arbitrarily shaped backbone curve. The backbone curve of the manipulator is defined by a position vector  $\mathbf{r}(s)$  and the position vector for the cable is given by

$$\hat{\mathbf{r}} = \mathbf{r} + R \cos \phi \mathbf{n} + R \sin \phi \mathbf{b}, \quad (4.18)$$

where  $R$  is the constant distance between the backbone curve of the manipulator and the cable,  $\phi$  is the circumferential location of the cable encoder on the manipulator cross section with respect to the neutral plane,  $\mathbf{n}$  is the vector normal to the backbone curve, and  $\mathbf{b}$  is the binormal vector. Differentiation produces

$$\frac{d\hat{\mathbf{r}}}{d\hat{s}} \frac{d\hat{s}}{d\sigma} = \frac{d\mathbf{r}}{d\sigma} + R \cos \phi \frac{d\mathbf{n}}{d\sigma} + R \sin \phi \frac{d\mathbf{b}}{d\sigma} \quad (4.19)$$

where  $\hat{s}$  parametrizes the cable arc length and  $\sigma$  is the arc length of the backbone after extension. Using Frenet-Serret formulas, we obtain

$$\frac{d\hat{\mathbf{r}}}{d\hat{s}} \frac{d\hat{s}}{d\sigma} = (1 - \kappa R \cos \phi) \frac{d\mathbf{r}}{d\sigma} - \tau R \sin \phi \mathbf{n} + \tau R \cos \phi \mathbf{b}, \quad (4.20)$$

where  $\kappa$  is the curvature and  $\tau$  is the torsion of the backbone curve. The Euclidean norm

of Eq. (4.20) is

$$\left( \sqrt{\frac{d\hat{\mathbf{r}}}{d\hat{s}} \cdot \frac{d\hat{\mathbf{r}}}{d\hat{s}}} \right) \frac{d\hat{s}}{d\sigma} = \sqrt{(1 - \kappa R \cos \phi)^2 + \tau^2 R^2} \quad (4.21)$$

The length of the cable encoder is

$$l = \int_0^\Lambda \sqrt{\frac{d\hat{\mathbf{r}}}{d\hat{s}} \cdot \frac{d\hat{\mathbf{r}}}{d\hat{s}}} d\hat{s} \quad (4.22)$$

$$= \int_0^L \sqrt{(1 - \kappa R \cos \phi)^2 + \tau^2 R^2} d\sigma \quad (4.23)$$

Using  $d\sigma = v ds$ , and changing the limits of integration, we have

$$l = \int_0^{L_0} v \sqrt{(1 - \kappa R \cos \phi)^2 + \tau^2 R^2} ds \quad (4.24)$$

Under the assumptions of planar deformation ( $\kappa = \theta_{,s}$ ), constant extension ( $v_{,s} = 0$ ) and no torsion ( $\tau = 0$ ), this reduces to

$$l = v \int_0^{L_0} |1 - \theta_{,s} R \cos \phi| ds_0 \quad (4.25)$$

We place the first cable at  $\phi_1 = \frac{\pi}{2}$ . Thus, its length

$$l_1 = L_0 v \quad (4.26)$$

and,

$$v = l_1/L_0. \quad (4.27)$$

The constants  $c_1$  and  $c_2$  in Eqs. (4.15) and (4.16) are determined using this value of  $v$ .

In practice,  $\kappa < \frac{1}{R \cos \phi_i}$ , so the absolute value in Eq. (4.25) is dropped, and the integral can be performed in closed form,

$$l_i = \frac{l_1}{L_0} (L - R \cos \phi (\theta(L) - \theta(0))). \quad (4.28)$$

The second encoder is placed at  $\phi_2 = 0$ , leading to the length of the second cable

$$l_2 = \frac{l_1}{L_0} (L_0 - R \Delta \theta). \quad (4.29)$$

From Eqs. (4.26) and (4.29),

$$\Delta \theta = \frac{L_0}{R} \left( 1 - \frac{l_2}{l_1} \right). \quad (4.30)$$

Eq. (4.30) suggests that the cable length is directly related to the orientation of the end effector and is independent of the actual shape taken by the manipulator backbone. This fact is consistent with the conclusion in [125] that the orientations at the ends of sections of continuum robots are directly controllable.

Equation (4.17) is solved with the boundary conditions

$$\theta(0) = \theta_0, \quad (4.31)$$

$$\theta(L) = \theta_0 + \Delta\theta \quad (4.32)$$

and

$$\theta_{,s}(L) = M_3. \quad (4.33)$$

The nonlinear differential equations and boundary conditions are solved using the collocation method routine provided in Matlab (bvp4c). The backbone curve is calculated by integrating the kinematic eqs. (2.26) using the calculated  $\theta(s)$ , with the assumption of no shear ( $\eta = 0$ ).

This method requires exact knowledge of fewer parameters. Geometric parameters  $L_0$  and  $R$  are used in Eq. (4.30). The ratio  $w/g = LW_g/GA_t$  in Eq. (4.17) must also be known. Significantly, the actuator parameters and Young's modulus do not need to be known. The measurement method is independent of an applied point load or payload at the tip.

In order to determine the accuracy of the estimated tip position taking into account sensor noise, sensitivity to measurement errors is calculated by numerically differentiating the tip position with respect to the measured cable encoder lengths and measured inclinometer rotations as in the previous section.

### 4.2.3 Shape Estimation using Inclinometers

In this method (Fig. 4.3), inclinometers are mounted at the base and at the end of each section of the manipulator. The assumptions involved in this method are identical to those in the load cell method. The extension of each section is assumed to be caused purely by pressurization, neglecting the effects of external loading. Under these assumptions, the rotation of the manipulator backbone is given by Eq. (4.17). This third order ordinary differential equation is solved by measuring three boundary conditions in  $\theta$  for each section using inclinometers. These rotation boundary conditions are

$$\theta(0) = \theta_0, \quad (4.34)$$

$$\theta(s_1^-) = \theta(s_1^+) = \theta_1, \quad (4.35)$$

$$\theta(s_2^-) = \theta(s_2^+) = \theta_2, \quad (4.36)$$

and

$$\theta(s_3^-) = \theta_3. \quad (4.37)$$

The curvature boundary conditions are

$$\theta_{,s}(s_1^-) = \epsilon_1 (\theta_{,s}(s_1^+) - M_2) + M_1, \quad (4.38)$$

$$\theta_{,s}(s_2^-) = \epsilon_2 (\theta_{,s}(s_2^+) - M_3) + M_2 \quad (4.39)$$

and

$$\theta_{,s}(s_3^-) = M_3 \quad (4.40)$$

where the value of  $\varepsilon_i$  is given by Eq. (2.45). If the payload, assumed to be applied at the tip of the manipulator, is known, then three inclinometers are sufficient to perform planar shape estimation for a three section soft robotic manipulator. Eq. (4.37) is replaced by the shear force boundary condition

$$\theta_{,ss}(s_3^-) = \zeta_3 F_3 \quad (4.41)$$

at the tip of the manipulator, where the value of  $\zeta_i$  is given by Eq. (2.46).

The nonlinear differential equations and boundary conditions are solved using the collocation method routine provided in Matlab (bvp4c). The backbone curve is calculated by integrating the kinematic Eqs. (2.26) using the calculated  $\theta(s)$ , with the assumption of no shear ( $\eta = 0$ ).

This method requires exact knowledge of the same parameters as the cable encoder method and is independent of an applied point load at the tip. The sensitivity of the estimated tip position to sensor noise is calculated by numerically differentiating the tip position with respect to the measured inclinometer rotations as in Section 4.2.1.

**Table 4.2.** Design parameters for the OctArm VI manipulator

<b>Design Parameter</b>	<b>Value</b>
$EA_1, EA_2$	2.584 kN
$EA_3$	1.292 kN
$GA_i$	$EA_i/3$
$EI_1, EI_2$	0.3225 Nm <sup>2</sup>
$EI_3$	0.1613 Nm <sup>2</sup>
$\alpha$	78°
$R$	42.9 mm
$L_1$	280 mm
$L_2$	265 mm
$L_3$	325 mm

### 4.3 Simulation results

To validate the accuracy of the proposed cable encoder and inclinometer shape estimation methods, the OctArm VI manipulator [176] is simulated for pressures ranging from 0 to 90 psi (See Table 4.2 for parameters). Control channels II and III are actuated simultaneously to achieve planar motion. For each actuation pressure, there are 64 on/off permutations of the six actuator inputs, coded from 000000 (all actuators off) to 111111 (all actuators on). For each permutation at each pressure, the RMS difference between the simulated tip position of the manipulator and the estimated tip position is plotted for vertical and horizontal base orientations. Figures 4.4 and 4.5 compare the measurement error for the cable encoder method averaged in a root mean squared sense over the 64 configurations with and without the constant curvature assumption. The plots show that the constant curvature assumption is accurate in the vertical orientation with low actuation pressures, but the error increases rapidly with increased pressures.

Tables 4.4 and 4.5 list the configurations with maximum and minimum tip position

**Table 4.3.** Sensor resolution values for experimental validation

<b>Sensor</b>	<b>Resolution</b>
$l_i$ (Cable encoder)	3 cm
$\theta_i$ (Inclinometer)	2.5°
$\eta_0$ (Load cell)	1/200N
$\nu_0$ (Load cell)	1/100N
$\mu_0$ (Load cell)	1/800Nm

estimation errors for the constant curvature and the full order cable encoder methods, the inclinometer method, and the load cell method at different pressures with horizontal and vertical orientations respectively. The assumed sensor resolution values are given in Table 4.3. In general, the maximum error in the constant curvature model occurs in configurations with long horizontal spans that maximize gravitational loading. At low pressures, the maximum error is realized if all the sections are curved upward (010101) in horizontal orientations or all the sections are curved in the same direction (101010 or 010101) in vertical orientations. At high pressures, the manipulator curves back towards the base, reducing the horizontal span and gravitational effect. For the horizontally oriented base, the error in the constant curvature assumption is maximum at zero pressure because the horizontal span is large. In both orientations, the average error approaches  $L/2$  at high actuation pressures.

Shape estimation with cable encoders using the full model leads to a decrease of more than one order of magnitude in tip position error. The average estimation errors for this method peak at  $0.026L$  for moderate pressures (20 - 40 psi) assuming no measurement errors. In the vertical orientation, the error is zero at zero pressure, corresponding to the case of an unloaded manipulator. In horizontal orientation, the error at

**Table 4.4.** Configurations with minimum and maximum tip position estimation errors for horizontal orientation.

$p$ (psi)	Const curvature		Cable encoder		Inclinometer		Load cell	
	Min	Max	Min	Max	Min	Max	Min	Max
0	101010	010101	100101	011010	100101	011001	101010	111111
10	101010	010101	010110	011010	100101	011001	101010	111111
20	101110	010101	000001	011010	000101	011010	101000	111111
30	100100	010001	000001	101010	010000	011010	010101	111111
40	011010	010000	000000	011001	010000	010111	100110	111111
50	100100	000000	000000	110111	010000	110111	101010	111111
60	010110	000000	000000	110110	010000	110110	101010	111111
70	011010	100000	001010	010111	010000	000111	010101	111111
80	100100	010000	000100	011110	010000	110110	010101	111111
90	010101	000000	001010	110111	110100	110110	000101	111111

**Table 4.5.** Configurations with minimum and maximum tip position estimation errors for vertical orientation.

$p$ (psi)	Const. curvature		Cable encoder		Inclinometer		Load cell	
	Min	Max	Min	Max	Min	Max	Min	Max
0	000000	101010	000000	011010	000000	101011	010101	111111
10	000000	101010	000000	011010	000000	101011	010101	111111
20	000000	101010	000000	100111	000000	100111	010101	111111
30	000000	101110	000000	101010	000000	010110	010101	111111
40	000000	011111	000000	101010	000000	010110	101010	111111
50	000000	111111	000000	111011	000000	011010	101010	111111
60	000000	111111	000000	110110	000000	111010	101010	111111
70	000000	101111	000000	010111	000000	000101	101010	111111
80	000000	111111	000000	111010	000000	111011	101010	111111
90	000000	111111	000000	110111	000000	011110	101010	111111

zero pressure is also small. Including the sensor resolution errors from Table 4.3 leads to a maximum average error of about  $0.1L$  in Figs. 4.4 and 4.5.

The load cell method bases on the full order model and provides the exact shape if one neglects sensor noise. To estimate the error associated with this technique, noise values  $\Delta\chi_i$  are assigned to the measured forces and bending moments at the base. For the planar problem, two forces (shear and axial) and one moment are measured. For OctArm VI, an ATI-Mini40 SI-20-1 load cell could be used with uncertainties shown in Table

4.3. For inclination measurement, a USD-T2 inclinometer would work well. Using the OctArm VI parameters, the uncertainties  $\Delta\chi_1 = 2.2 \times 10^{-6}$ ,  $\Delta\chi_2 = 3.3 \times 10^{-6}$ ,  $\Delta\chi_3 = 9.0 \times 10^{-5}$ ,  $\Delta\chi_4 = \Delta\chi_5 = 0$  and  $\Delta\chi_6 = 8.7 \times 10^{-4}$ , the tip position error is calculated using Eq. (4.12). The average tip position error caused by the measurement uncertainties remains fairly constant at moderate and high pressures, at around  $0.007L$ . However, the average error is as high as  $0.012L$  at low pressure for the vertical configuration and  $0.01L$  for the horizontal configuration. In the experiment described in the next section, the sensing errors are an order of magnitude higher. Figures 4.4 and 4.5 show the average tip position error for the OctArm VI manipulator, with uncertainties  $\Delta\chi_1 = 2.2 \times 10^{-5}$ ,  $\Delta\chi_2 = 3.3 \times 10^{-5}$ ,  $\Delta\chi_3 = 9.0 \times 10^{-4}$ ,  $\Delta\chi_4 = \Delta\chi_5 = 0$  and  $\Delta\chi_6 = 8.7 \times 10^{-3}$ .

Tables 4.4 and 4.5 show that for the load cell method, the error is maximum for configurations with low shear ( $\chi_2(s)$ ), *e.g.*, 111111, and is minimum for configurations with high shear (*e.g.*, 010101 at low and moderate pressures). This is because  $\chi_2(s)$  is comparatively small in magnitude in all configurations, and a small absolute error  $\Delta\chi_2$  in its measurement leads to a large relative error,  $\Delta\chi_2/\chi_2$ , and thus, a comparatively larger error in shape estimation.

The average tip position error for the inclinometer method, assuming perfect measurement of rotations is lower than the cable encoder method. The maximum average error peaks at  $0.015L$  between 40 and 60 psi. Including the sensor error from Table 4.3 in the measurement of rotation increases the maximum average error to about  $0.08L$  around 60 psi in Figs. 4.4 and 4.5.

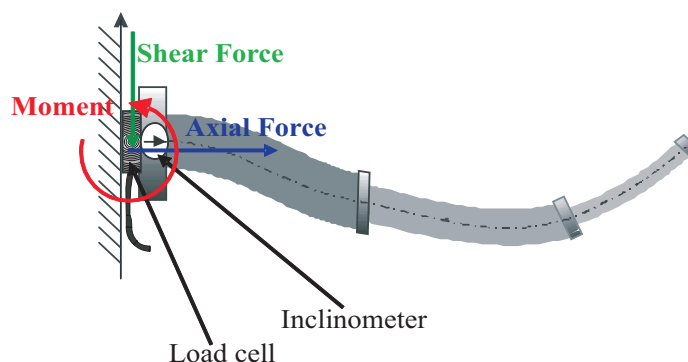


**Figure 4.1.** Schematic showing the use of a base-mounted load cell for shape sensing of a three section soft robotic manipulator in planar operation. An inclinometer is also mounted on the base.

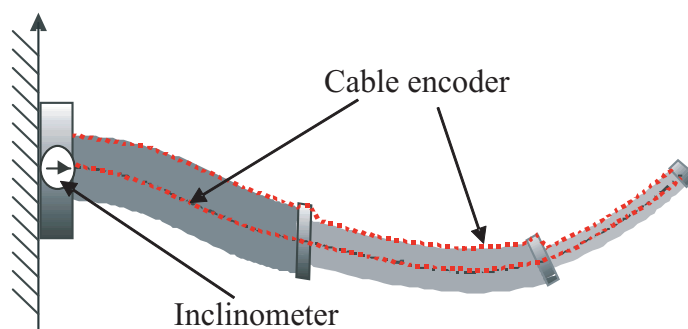


**Figure 4.2.** Schematic showing the use of cable encoders (–) for shape sensing of a three section soft robotic manipulator in planar operation. An inclinometer is also mounted on the base.

## 4.4 Experimental validation

The three shape sensing methods are validated experimentally using the OctArm VI manipulator. In order to simplify the validation procedure, the manipulator is hinged at the base using a roller bearing. This eliminates the reaction moment at the base, thereby making the base force and moment boundary conditions known. For input pressures ranging from 0 to 90 psi (10 steps), 64 on/off configurations are generated, and photographed. Edge detection and marker recognition are used to estimate encoder lengths

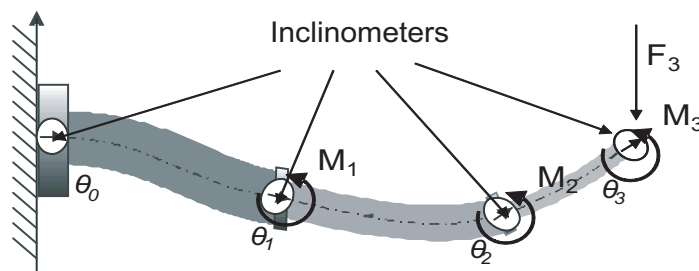


**Figure 4.3.** Schematic showing the use inclinometers for shape sensing of a three section soft robotic manipulator in planar operation. If the weight of the tip payload is known, an inclinometer at the tip is not required.

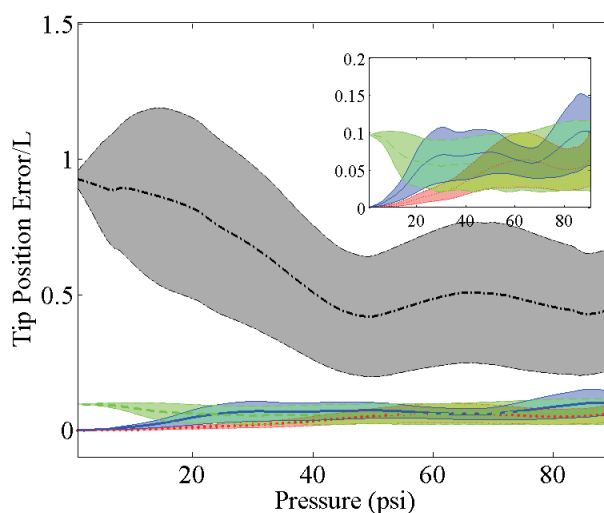


**Figure 4.4.** Error in manipulator tip position estimation averaged (RMS) over 64 configurations in the horizontal base orientation using cable encoders with a constant curvature model (dash-dotted), cable encoders with the full model (solid) and the load cell method (dashed). The inset shows details of the tip position estimation error for the cable encoder method with full model (solid) and the load cell method (dashed). The area representing one standard deviation around the average error is shaded.

and rotations at the end of each section. This approach does not provide the accuracy that could be obtained using actual sensors, but are sufficient for validation. The experiment is repeated with and without a payload 10 N or 7.5% of the weight of the setup including counterweight). Figure 4.6 (a) shows the average error over 64 configurations for the

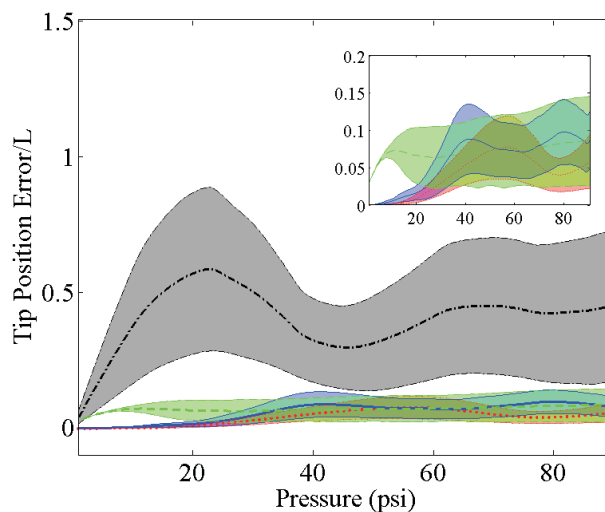


**Figure 4.5.** Error in manipulator tip position estimation averaged (RMS) over 64 configurations in the vertical base orientation using cable encoders with a constant curvature model (dash-dotted), cable encoders with the full model (solid) and the load cell method (dashed). The inset shows details of the tip position estimation error for the cable encoder method with full model (solid) and the load cell method (dashed). The area representing one standard deviation around the average error is shaded.

three methods for the manipulator without a payload. Figure 4.6 (b) shows these errors for manipulator with a payload. The error in shape estimation using only the model is included for reference. The payload is assumed to be unknown during estimation.

In absence of a payload, shape estimation with sensors have an error comparable to shape estimation without sensors, with a maximum average error of  $0.12L$ . This error is an order of magnitude higher than the estimated error using actual encoders and sensors, because the image processing method of simulating sensor measurements is prone to noise and errors. However, the benefits of sensing become clear when an unknown payload is added. Shape estimation without sensing is unable to account for the effect of an unknown payload, while the three shape sensing methods are able to

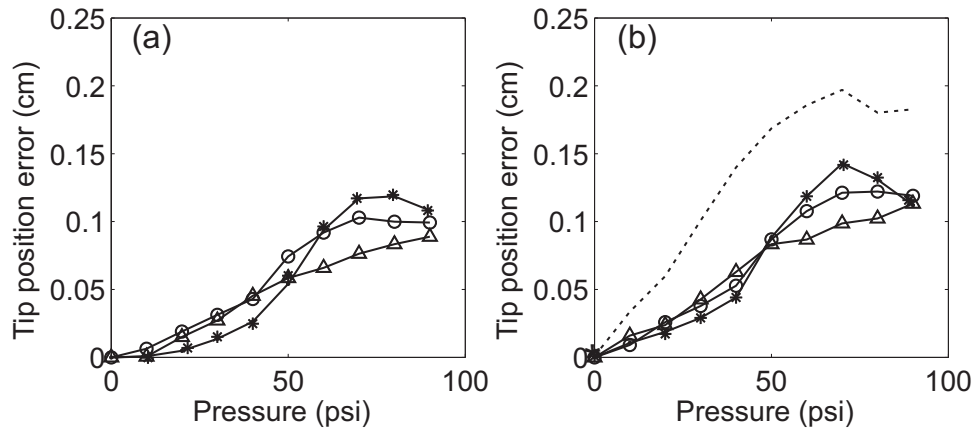


**Figure 4.6.** Average error in tip position estimation for the inclinometer method (circles), cable encoder method (asterisks) and the load cell method (triangles) without payload (a) and with a payload of 10 N (b). For the hinged boundary condition in absence of payload, shape estimation without sensing coincides with the load cell method. In presence of a payload, shape estimation without sensing (dashed) shows high error if the payload weight is unknown.

take the resulting displacement into account.

## 4.5 Conclusions

Three shape estimation methods for soft robotic manipulators are presented and compared. The maximum average tip localization error for the cable encoder method, assuming perfect measurements and using the geometrically exact (full) model is  $0.026L$ , while the error in the constant curvature model is  $L/2$ . In this method, the error peaks at a pressure between 20 - 40 psi. For the load cell method, the maximum average error for a typical commercially available load cell (ATI-Mini40) is  $0.012L$ . The error is larger at low pressure, but does not vary significantly at moderate to high pressure. Error in measurement of shear loading is the largest contributor to the total tip positioning error. The

average error for the inclinometer method is within  $0.01L$  with an inclinometer resolution of  $0.05^\circ$ . Experimental testing is conducted to validate the shape sensing methods. The tests show the benefit of sensing in improving the accuracy of shape estimation when an unknown payload is applied to the tip of the manipulator.

# Dexterity and Workspace Analysis

## 5.1 Introduction

OctArm design is complicated due to the presence of endplates with complex manifolds and internal pressurizing lines (See Fig. 1.9(c)). In addition to making the manipulator expensive to fabricate, end plates add passive mass to the manipulator, which reduces its load capacity.

We propose the cost effective soft robotic manipulator design shown in Fig. 5.1. Unlike the OctArm series of robot arms, the extensor actuators in this Continuous Tube (CT) design do not extend only within one section. The three innermost actuators extend from the base to the tip of the arm. The outer layer of actuators extend roughly half way down the arm and then are capped off. By pressurizing different combinations of actuators, one can bend each section of the arm in two directions and/or extend the section. The beauty of the CT design is that all of the arm complexity is at the base.

Unlike the OctArm series of arms, there are no endplates with complex manifolds or internal pressurizing lines. All of the pressurized air and manifolding is provided at the base. Thus, compared to the OctArm series of robots, the CT arm is less expensive to manufacture and has increased load capacity without the passive weight of the end plates.

For given maximum pressure constraints on the actuators, however, the CT manipulator design may have a smaller and less dexterous workspace as compared to OctArm. For example, it is not possible to generate the maximum clockwise moment on the base section simultaneously with the maximum counterclockwise moment on the distal section. In OctArm, the moments for each section were concentrated at the ends of the section. Moments applied to the end of the distal section in the new design, however, are countered by moments at the base. Thus, the curvatures of the distal sections in the new design propagate to the base. Hence, the range of motion that could be produced by the CT manipulator is restricted, limiting its workspace. This may be countered, on the other hand, by an increase in workspace due to reduced gravitational loading. The coupling between the two sections also affects dexterity of the manipulator. This chapter investigates the differences in dexterity and reachable workspace between the new low-cost design and the OctArm-type design.

Dexterity is defined as the relative ease with which the manipulator end effector can move in all directions starting from a given pose. Several measures of dexterity have been defined in past research that use the singular values of the manipulator Jacobian.

Manipulability is proportional to the volume of the manipulability ellipsoid [179] and represents an average mobility over all directions at the end-effector. The condition number is the ratio of the largest to the smallest singular value and measures the eccentricity of the manipulability ellipsoid, and indicates the relative sensitivity of movement to applied pressure. The condition number is a nondimensional measure and thus independent of the scale of a manipulator, with a minimum (best) value of unity. Isotropy [180] is another dexterity measure, defined as a ratio of the geometric mean and the arithmetic mean of the singular values of the Jacobian. This dimensional ratio is easier to obtain in closed form, and is maximum (equal to one) when all singular values are the same (isotropic), and minimum (equal to zero) at a kinematic singularity.

The smallest singular value of the Jacobian matrix represents the worst case scaling of the mapping from pressure to end effector velocity, the maximum force transmission ratio, and the best accuracy (large changes in pressure create small movements). If the smallest singular value is zero then the matrix is singular. The largest singular value of the Jacobian, represents the maximum velocity transmission ratio, the minimum force transmission ratio, and the worst accuracy. In the new robot design, the only change is the application of the moments so the same modeling approach applies. In this chapter, the two manipulator designs are compared with respect to these five dexterity measures.

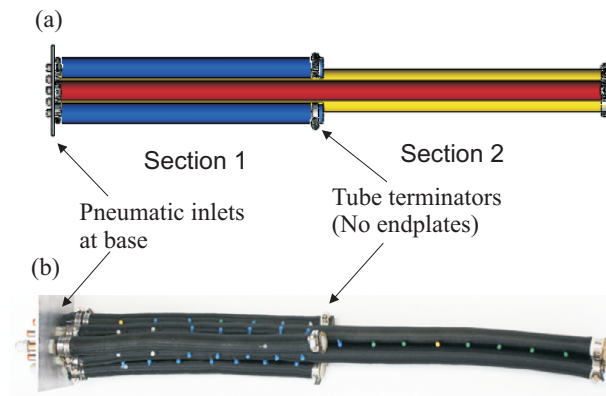


**Figure 5.1.** Continuous Tube (CT) manipulator: (a) 3D schematic (b) Photograph of fabricated arm.

### 5.1.1 Manipulator mechanics

The fully 3-D spatial manipulator mechanics including shear, bending, and extension are derived in Chapter 2. This chapter focuses on planar motion to compare the two manipulator designs without the complexity of the 3-D model. The results obtained can be extended to 3-D using the same approaches described herein. To maintain the arm in the  $XY$  plane, we actuate control channels 2 and 3 (See Fig. 5.2) together using the control inputs simultaneously:  $p_1$  and  $p_{23}$  to provide  $\pm$  bending and extension. There are two control channels for each section, giving a total of four control channels for two section planar manipulation. We model the arm as a Cosserat rod with the planar displacement of the backbone curve defined by  $\mathbf{r}(s) = x(s)\mathbf{i} + y(s)\mathbf{j}$ , where  $s$  is the arc length coordinate along the deformed arm (see Fig. 5.3) [165]. The kinematic differential equations are given by Eqs. (2.26).

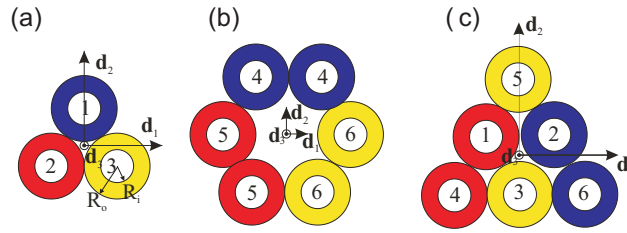


**Figure 5.2.** Cross-sectional view of the (a) six- and (b) three- extensor sections in the OctArm manipulator and the base section of the CT manipulator (c), showing three independent control channels in red, yellow and blue. The three-tube section of the continuous tube manipulator is identical to (c) with tubes 4,5 and 6 removed.

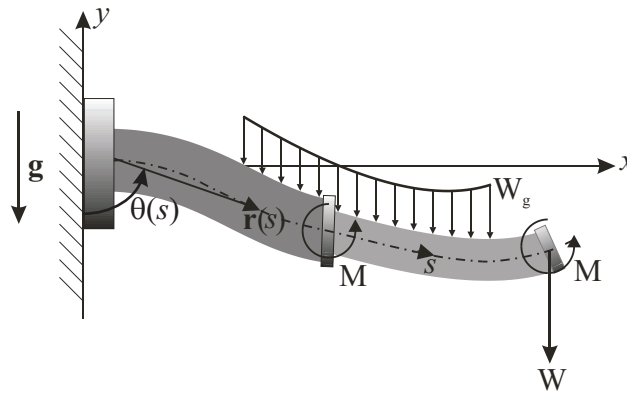


**Figure 5.3.** Model for a two-section soft robotic manipulator.

The kinematic boundary conditions are

$$x(0) = 0, \quad y(0) = 0, \quad \theta(0) = \theta_0, \quad (5.1)$$

where  $\theta_0$  indicates the orientation of the base of the manipulator. The axial, shear, and moment balance laws in component form yield Eqs. (2.55)-(2.57). The total cross sectional area  $A_{T,i}$  and moment of inertia,  $I_{T,i}$  for each section of the two manipulators is given in Table 5.1. At the end of each section, the displacement and rotation are continuous but the tube pressure acts to produce step changes in axial and shear strain

**Table 5.1.** End section moments and moments of inertia for the OctArm and CT manipulators.

Parameter	OctArm	Continuous Tube
$\frac{M_{1x}}{EA_t R_o}$	$2 \begin{pmatrix} \Delta\lambda_2 + \Delta\lambda_3 \\ -2\Delta\lambda_1 \end{pmatrix}$	$\frac{\sqrt{3}}{3} \begin{pmatrix} \Delta\lambda_1 + \Delta\lambda_2 \\ -2\Delta\lambda_3 - 2\Delta\lambda_4 \\ +4\Delta\lambda_5 - 2\Delta\lambda_6 \end{pmatrix}$
$\frac{M_{1y}}{EA_t R_o}$	$2(\Delta\lambda_3 - \Delta\lambda_2)$	$\begin{pmatrix} \Delta\lambda_1 - \Delta\lambda_2 \\ +2\Delta\lambda_4 - 2\Delta\lambda_6 \end{pmatrix}$
$\frac{M_{2x}}{EA_t R_o}$	$2 \begin{pmatrix} \Delta\lambda_5 + \Delta\lambda_6 \\ -\frac{2}{\sqrt{3}}\Delta\lambda_4 \end{pmatrix}$	$\frac{\sqrt{3}}{3} (\Delta\lambda_1 + \Delta\lambda_2 - 2\Delta\lambda_3)$
$\frac{M_{2y}}{EA_t R_o}$	$\frac{2}{\sqrt{3}} (\Delta\lambda_6 - \Delta\lambda_5)$	$(\Delta\lambda_1 - \Delta\lambda_2)$
$I_{1xx} = I_{1yy}$	$6(I + A_t R_o^2/2)$	$6I + 5A_t R_o^2/2$
$I_{2xx} = I_{2yy}$	$3(I + A_t R_o^2/2)$	$3(I + A_t R_o^2/2)$
$A_{T,1}$	$6A_t$	$6A_t$
$A_{T,2}$	$3A_t$	$3A_t$
Planar operation condition	$\Delta\lambda_I = \Delta\lambda_1, \Delta\lambda_{II} = \Delta\lambda_3 = \Delta\lambda_2, \Delta\lambda_{III} = \Delta\lambda_4$ and $\Delta\lambda_{IV} = \Delta\lambda_6 = \Delta\lambda_5$	$\Delta\lambda_I = \Delta\lambda_1 = \Delta\lambda_2, \Delta\lambda_{II} = \Delta\lambda_3, \Delta\lambda_{III} = \Delta\lambda_5$ and $\Delta\lambda_{IV} = \Delta\lambda_4 = \Delta\lambda_6$

and curvature [176]. The applied moment,  $M_i$ , at the end of each section is listed in Table 5.1.

These equations are simplified by assuming that the extension of each section is constant and is caused purely by pressurization, neglecting the effects of external loading. Under these assumptions, Eqs. (2.55) - (2.57) simplifies to Eq. (4.17). This nonlinear boundary value problem can be solved in closed form, by approximating  $\cos \theta$  by  $\cos(\theta_0 + ks)$  in Eq. (4.17). The solution is

$$\begin{aligned} \theta_1 = & \theta_0 + \psi_1 s + \psi_2 s^2 \\ & + \frac{b_1}{M_1^3} (\sin(\theta_0 + M_1 s) - \sin \theta_0) \end{aligned} \quad (5.2)$$

$$\begin{aligned}\theta_2 &= \theta_1(1) + \psi_3 s + \psi_4 s^2 \\ &\quad + \frac{b_2}{M_2^3} (\sin(\theta_0 + M_1 + M_2 s) - \sin(\theta_0 + M_1))\end{aligned}\quad (5.3)$$

The constants  $\psi_i$  are shown in Appendix C.

The end effector position  $\mathbf{x} = \{x, y\}^T$  can be obtained by integrating Eqs 2.25 - 2.26, with the assumption of no shear deformation.

$$x(1) = \int_0^1 v \cos \theta ds \quad (5.4)$$

$$y(1) = \int_0^1 v \sin \theta ds \quad (5.5)$$

At equilibrium pose, the relationship between a small perturbation in input pressure  $\tilde{\mathbf{p}} = \{\tilde{p}_1, \tilde{p}_2, \tilde{p}_3, \tilde{p}_4\}^T$  and the resulting displacement  $\tilde{\mathbf{x}}$  of the end effector is

$$\tilde{\mathbf{x}} = \mathbf{J}\tilde{\mathbf{p}} \quad (5.6)$$

where the Jacobian,  $\mathbf{J} \in \mathbb{R}^{m \times n}$ , is

$$\mathbf{J} = \begin{bmatrix} \frac{\partial x(1)}{\partial p_1} & \frac{\partial x(1)}{\partial p_2} & \frac{\partial x(1)}{\partial p_3} & \frac{\partial x(1)}{\partial p_4} \\ \frac{\partial y(1)}{\partial p_1} & \frac{\partial y(1)}{\partial p_2} & \frac{\partial y(1)}{\partial p_3} & \frac{\partial y(1)}{\partial p_4} \end{bmatrix} \quad (5.7)$$

The terms of the Jacobian are obtained in closed form by differentiating Eqs. (5.4)-(5.5) with respect to the input pressures  $p_i$  and are shown in Appendix C.

## 5.2 Manipulability Analysis

The Jacobian  $\mathbf{J}$  may be decomposed using the singular value decomposition ,

$$\mathbf{J} = \mathbf{U}\Sigma\mathbf{V}^T, \quad (5.8)$$

where  $\mathbf{U} \in \mathbb{R}^{m \times m}$  and  $\mathbf{V} \in \mathbb{R}^{n \times n}$  are orthogonal matrices and  $\Sigma \in \mathbb{R}^{m \times n}$  is a diagonal matrix consisting of singular values. Substituting Eq. (5.8) into Eq. (5.6), we get

$$\mathbf{U}^T \tilde{\mathbf{x}} = \Sigma (\mathbf{V}^T \tilde{\mathbf{p}}) \quad (5.9)$$

The singular values define the magnitude of the end effector motions of the end effector resulting from applied pressure of unit magnitude. The larger (smaller) singular value corresponds to highest (lowest) manipulability. The right singular vectors,  $\tilde{\mathbf{v}}_i$ , describe the normalized linear combination of pressure inputs that cause a motion of norm  $\sigma_i$  in the left singular vector direction  $\tilde{\mathbf{u}}_i$ .

## 5.3 Results

### 5.3.1 Workspace

Figure 5.4 shows a comparison of the workspaces of the OctArm and the CT manipulators mounted in a vertical configuration, hanging downwards. The theoretical plots

(Figs 5.4(a and c)) are obtained by solving Eqs. (5.4)-(5.5) and plotting tip position of the manipulator for all 2401 permutations of input pressure ranging from 0 to 70 psi (discretized into 7 levels) on the four control channels for the planar case. To obtain the workspace plots experimentally (Figs 5.4(b and d)), the manipulator is photographed for each pressure input, and the shape and tip position are measured. Significant differences in the workspace envelopes of the two designs are observed. In the CT design, it is not possible to simultaneously apply the largest (smallest) possible moment  $M_2$  in section 2 and smallest (largest) possible moment  $M_1$  in section 1. Also, a nonzero  $M_2$  cannot be generated without producing extension in section 1. This restricts the workspace of the new design such that the nonreachable region around the manipulator base extends radially further outwards. On the other hand, the OctArm design allows independent inputs in all sections, so, this restriction is not present (See Fig. 5.4(a) and (b)). The plot shows that the absence of endplates on the CT manipulator reduces the gravitational loads on it, raising the highest point in the workspace from  $(\pm 0.31, -0.02)$  in the case of the OctArm-type manipulator to  $(\pm 0.37, 0.11)$ . This gives the CT manipulator a workspace area slightly larger than that of the OctArm-type manipulator ( $0.6\pi L^2$  compared to  $0.5\pi L^2$ ). The contours in the workspace plots show the density of reachable points ( $/\text{cm}^2$ ). The two manipulators show a similar trend with highest density close to the unactuated tip position of the manipulator,  $(0, -L)$ .

### 5.3.2 Dexterity

Figure 5.5 compares the five dexterity measures described in Section 1, for the OctArm and CT manipulators. The minimum singular values,  $\sigma_2$ , of the Jacobian (Fig. 5.5(a)) and isotropy (Fig. 5.5(d)) are the highest in the interior of the workspace, and decrease rapidly towards the workspace boundary for both the manipulators. Figure 5.6 plots the workspace area versus minimum singular value threshold. OctArm and CT manipulators have higher workspace areas at low and high singular value thresholds, respectively. This reflects the higher dexterity of the Octarm but larger workspace of the CT manipulator. Figure 5.5(c) compares the manipulability of the two manipulators using the product of the two singular values of the Jacobian ( $\sigma_1 \sigma_2$ ). Areas with small  $\sigma_2$  (Fig. 5.5(a)), also have a low manipulability. The shape of the manipulability contours is relatively complex because there are many regions in the workspace that have low manipulability, namely the regions where  $\sigma_2$  is small. Figure 5.5(b) suggests that these are the regions where one or both of the manipulator sections are highly curved. The region near  $(0, -0.5)$ , for example, has high  $\sigma_2$  and low manipulability in the OctArm workspace in the vicinity of  $(0, -0.5)$ . This region can be reached by maximally curving section 2 of the OctArm, and leaving section 1 unactuated. This configuration is unattainable by the CT manipulator. The condition number (Fig. 5.5(e)) for the workspace is the ratio  $\sigma_1/\sigma_2$ . The condition number is large in places where either  $\sigma_1$  is large (*e.g.*, around  $(0, -0.6)$ , where it is easiest to produce circumferential displacement) or where  $\sigma_2$  is small (*e.g.*, at the boundaries of the workspace, where the configurations become almost

singular).

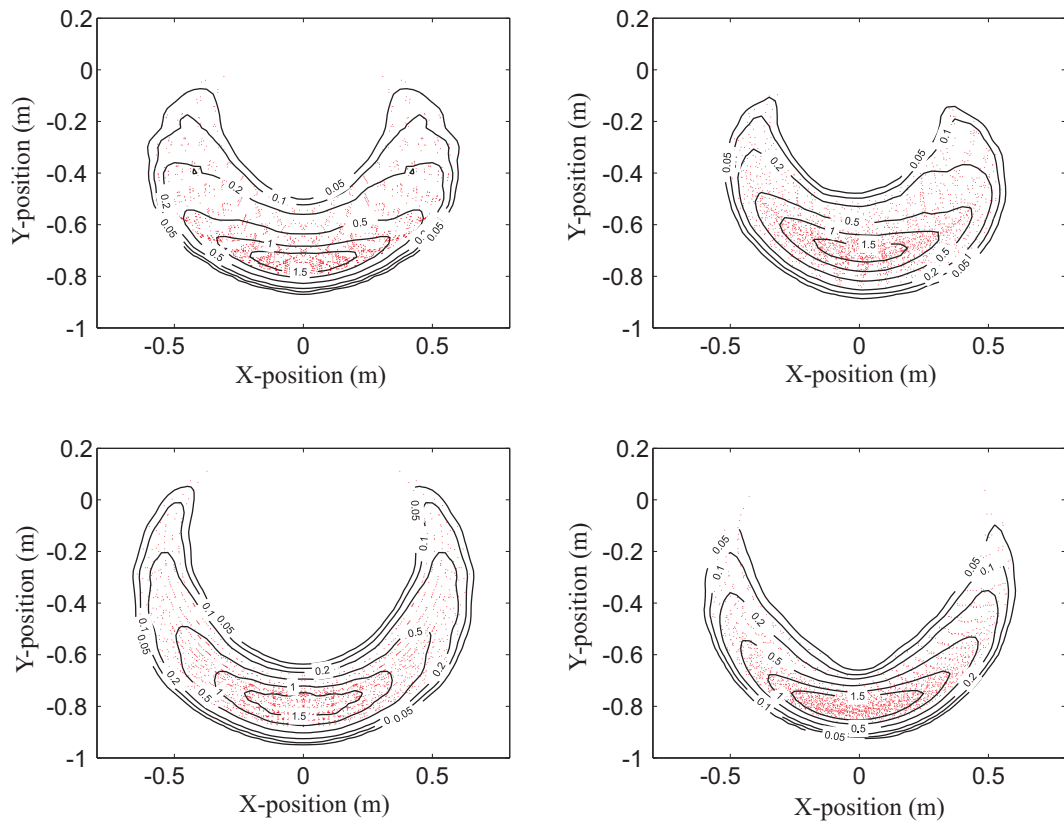


**Figure 5.4.** Theoretical (left) and experimental (right) workspace for the OctArm (top) and CT (bottom) manipulators: Endpoint positions (red dots) and workspace density contours (points/cm<sup>2</sup>).

## 5.4 Conclusions

A cost-effective soft robotic manipulator design that uses continuous tubes instead of endplates and pneumatic supply lines is presented, and its workspace is compared with an OctArm manipulator. The absence of endplates increases the workspace in some regions, but constraints are imposed on the range of moments that could be produced

by the actuators, leading to loss of workspace in other regions. On the whole, there is a marginal increase in the workspace with the CT design. The quality of the workspace is compared using the notions of dexterity and manipulability. The design simplifications introduced in the CT design compromise its dexterity almost throughout the workspace, such that more actuation effort is required to move the manipulator tip along the minor axis of the manipulability ellipse. However, the continuous tube design is much more cost-effective, making it attractive for many applications.

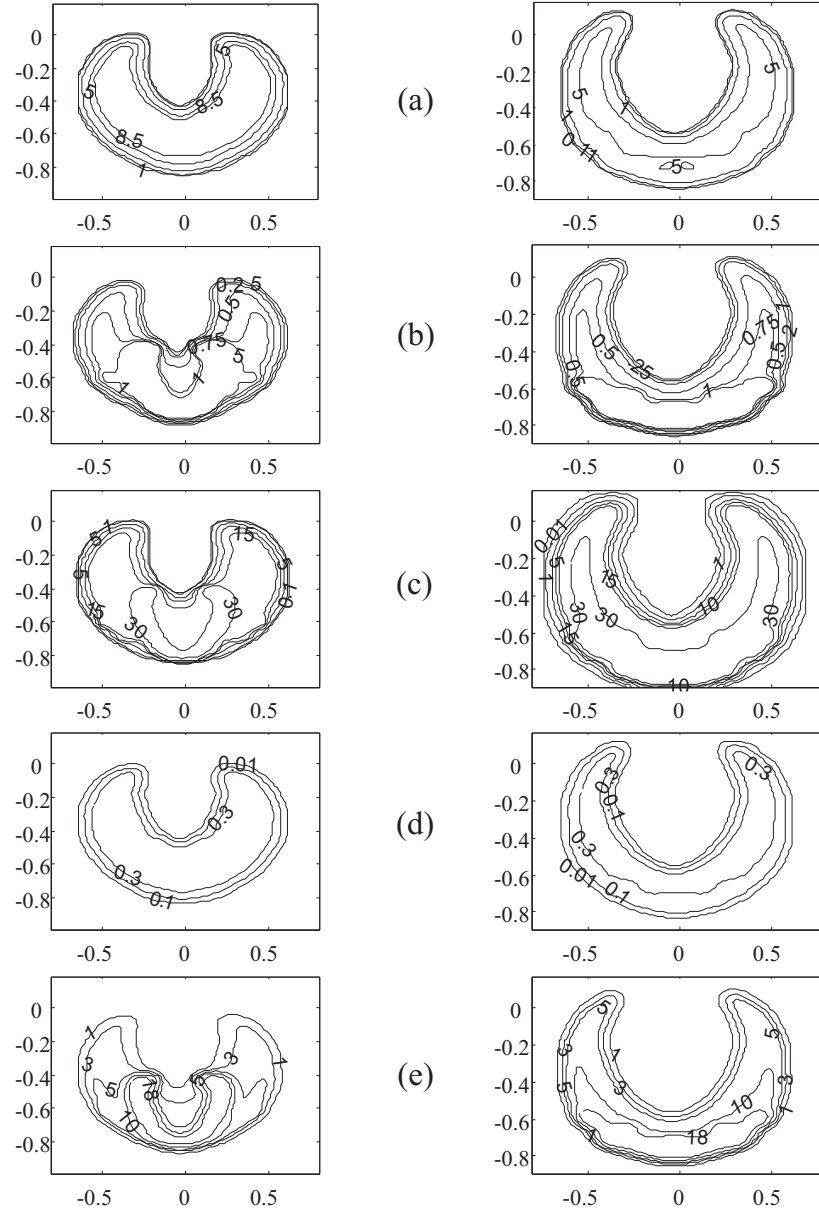


**Figure 5.5.** Dexterity measures for the OctArm (left) and continuous-tube (CT) (right) manipulators: (a) minimum singular value,  $\sigma_2$  ( $10^{-8}$  m/Pa), (b) maximum singular value  $\sigma_1$  ( $10^{-6}$  m/Pa), (c) manipulability,  $\sqrt{\sigma_1 \sigma_2}$  ( $10^{-8}$  m/Pa), (d) isotropy,  $\sqrt{\frac{\sigma_1 \sigma_2}{\sigma_1 + \sigma_2}}$  and (e) condition number,  $\frac{\sigma_1}{\sigma_2}$ .

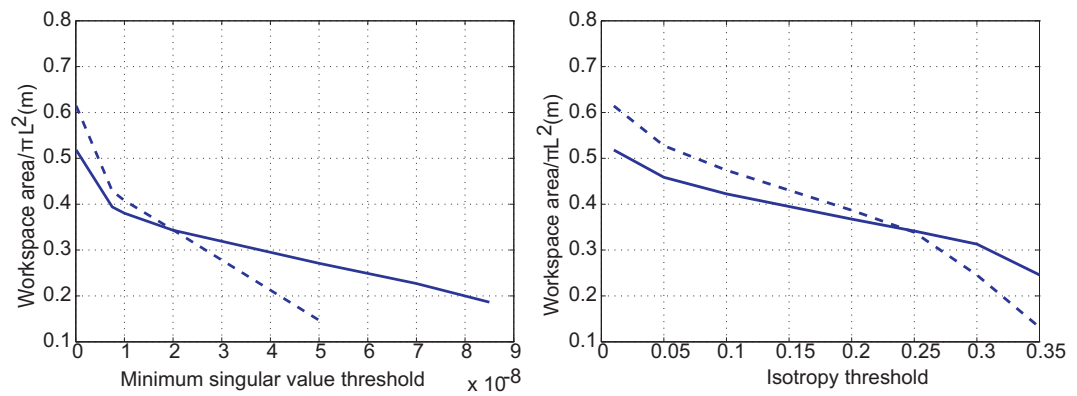


**Figure 5.6.** Dexterous workspace area fraction versus dexterity threshold for the OctArm (solid) and CT (dashed) manipulators.

# Chapter 6

## Conclusions

Researchers have been inspired by biology to design and build soft robots. With a soft structure and redundant degrees of freedom, these robots can be used for delicate tasks in cluttered and/or unstructured environments. In this research, the state of the art of soft robotics, including their biological inspiration and novel capabilities is surveyed and existing challenges are outlined. A geometrically exact model for soft robotic manipulator is developed. This model is found to be an order of magnitude more accurate than the constant-curvature models used by previous researchers. The model is used for design optimization, workspace analysis, and shape estimation.

The design of soft robotic manipulators requires specification of a dexterity template with given wrap angles for each section. Then, for any given configuration of the manipulator, the tube thickness and section lengths can be calculated to provide the desired overall base diameter and total length. The actuator configuration depends on the length of the manipulator, and can be optimized to maximize load capacity. The

optimal design depends on the  $p_{\max}/E$  ratio so a single optimal design exists for a family of constant  $p_{\max}/E$  manipulators. As the number of sections increases, the complexity of design and fabrication, dexterity, and load capacity increase, creating a trade-off between cost and performance.

The model is used to develop three shape estimation methods for soft robotic manipulators. The load cell method uses an inclinometer to measure base rotation and a load cell that measures axial and shear forces and moment at the base. Equilibrium equations are then integrated from base to tip to predict the shape of the manipulator. The cable encoder method uses an inclinometer at the base, and cable encoders along the length of the manipulator. The inclinometer method uses an inclinometer mounted at base and at the end of each section. Experimental testing with low resolution sensors indicates a maximum average tip position error of about 1/8 of the manipulator length. Simulation with typical commercially available encoders and sensors predict a maximum average tip position error of 1/40 of the manipulator length.

Based on the model, dexterity and manipulability of a cost-effective continuous tube soft robotic manipulator design is compared with an OctArm manipulator. The absence of endplates increases the workspace in some regions, but constraints are imposed on the range of moments that could be produced by the actuators, leading to loss of workspace in other regions. On the whole, there is a marginal increase in the workspace with the CT design. The quality of the workspace is compared using the notions of dexterity and manipulability. The design simplifications introduced in the CT design compromise

its dexterity in most of the workspace, meaning that more actuation effort is required to move the manipulator tip along the minor axis of the manipulability ellipse. However, the continuous tube design is more cost-effective, making it attractive for many applications.

## 6.1 Future Work

Full solution of the dynamics equations of the soft robotic manipulators based on the model described in preceding chapters will provide insight and predict performance for dynamic tasks. Standard methods for time integration like Runge-Kutta, Crank-Nicholson, or those from the Newmark-Wilson family cannot directly be applied to solve the dynamics equations in case of rods undergoing finite rotations because of differential nature of the rotational manifold. If used directly, these methods can fail due to instabilities caused by energy overshoot [181]. Numerical methods for geometrically nonlinear beams have been investigated by several researchers. Simo and Vu-Quoc, [182, 183], for example, develop an implicit, second order accurate numerical method for solving the long-term dynamic response of non-linear geometrically exact rods undergoing finite extension, shear and bending, accompanied by large overall motions.

The dynamic models can be used in the design process and to implement feedforward and feedback control and develop algorithms for accurate path planning. The dynamics solution could also be used to calculate inverse manipulator kinematics and dynamics for feedforward control.

Finally, the grasp stability of soft robotic manipulators in whole arm manipulation also needs to be analyzed. Grasping objects using whole arm manipulation requires the grasp to be stable in some sense, although this stability has been defined in various ways in literature. According to Fearing [151], the three desired properties for stable grasp are static equilibrium, no slippage, and the ability of resisting disturbances in all directions. Stability could be hard to analyze and ensure for soft robotic manipulators because of their high compliance and continuous deformation. Path planning and control algorithms should take into account the stability of all intermediate configurations that the manipulator passes through. Field trials on the OctArm series of robots indicate that in some configurations, objects cannot be manipulated properly by the OctArm and are dropped due to a combination of lack of grip strength/grasp stability [184]. Conditions for stable grasping and manipulations that could be incorporated into path planning and control mechanisms should be formulated.

# Appendix A

## Matlab code

This appendix lists the MATLAB code for the geometrically exact soft robotic manipulator model.

### A.1 Actuator model

```
function residue = PvsF(lambda1, alpha, Ri,Ro, L, E, A,p)
% Pressure vs. Force relation
C1 = E./6;
EA = E.*A;

function residue = PvsF(lambda1, alpha, Ri,Ro, L, E, A,p)
% Pressure vs. Force relation
C1 = E./6;
EA = E.*A;

residue = - 2.*( - 2.*cos(alpha).^6.*C1.*lambda1.^2 + C1 +
4.*cos(alpha).^4.*C1.*lambda1.^2 - cos(alpha).^4.*C1.*lambda1.^8 +
2.*cos(alpha).^2.*C1.*lambda1.^6 - 2.*cos(alpha).^2.*C1 -
C1.*lambda1.^4 - 2.*cos(alpha).^2.*C1.*lambda1.^2 +
2.*cos(alpha).^6.*C1.*lambda1.^8 - 4.*cos(alpha).^4.*C1.*lambda1.^6 +
2.*cos(alpha).^2.*C1.*lambda1.^4 + cos(alpha).^4.*C1).*( -
Ro.^2 + Ri.^2)./Ri.^2./lambda1.^3./( - 1 +
5.*lambda1.^2.*cos(alpha).^2 - 7.*lambda1.^4.*cos(alpha).^4 +
3.*lambda1.^6.*cos(alpha).^6) - p;
```

## A.2 Spatial model

### A.2.1 Main script

```

function pos = getendptN(g,e,w,l,M,p,er,lr,pointld,gravangle,L,Nsect);

N=30;                %No. of points
% Initial guesses

v1 = zeros(1,6*Nsect);
for i = 1:Nsect
    v1(i) = 1;                %nu1
    v1(Nsect+i) = 0;         %eta1
    v1(2*Nsect+i) = M(i);    %mu1
    v1(3*Nsect+i) = 0;      %x
    v1(4*Nsect+i) = 0;      %y
    v1(5*Nsect+i) = 0;      %theta
end

x1 = linspace(0,1,N);
options = bvpset('RelTol', 1e-4, 'AbsTol', 1e-4, 'Nmax', 30);
solinit1 = bvpinit(x1,v1);

% Solution with applied load
try,
    solg = bvp4c(@diffeqs2DNnd,@allbcs2DNnd,solinit1,options,...
        g,e,w,l,M,p,er,lr,pointld,gravangle,Nsect);
    sol = bvp4c(@diffeqs2DNnd,@allbcs2DNnd,solinit1,options,...
        g,e,w,l,M,p,er,lr,0*pointld,gravangle,Nsect);
catch,
    st = 1000;
    return;
end

Msize=length(solg.x);

%Solution with gravity
sg.nu = solg.y(1:Nsect,:);
sg.eta = solg.y(Nsect+1:2*Nsect,:);
sg.mu = solg.y(2*Nsect+1:3*Nsect,:);
sg.x = solg.y(3*Nsect+1:4*Nsect,:);
sg.y = solg.y(4*Nsect+1:5*Nsect,:);
sg.theta = solg.y(5*Nsect+1:6*Nsect,:);

sg.ss = [];
sg.x = [];
sg.y = [];
Lsum = 0;
for i = 1:Nsect
    sg.ss = [sg.ss Lsum+ L(i)*solg.x];
    sg.x = [sg.x L(i)*solg.y(3*Nsect+i,:)];
    sg.y = [sg.y L(i)*solg.y(4*Nsect+i,:)];
    Lsum = Lsum + L(i);
end

sg.nu = sg.nu(:);
sg.eta = sg.eta(:);

```

```

sg.mu = sg.mu(:);
sg.theta = sg.theta(:);
sg.ss = sg.ss';sg.ss = sg.ss(:);
t1=sg.ss/sum(L)*2*pi;
stgy = (sg.y(end));
stgx = (sg.x(end));

%Solution without gravity
s.nu = sol.y(1:Nsect,:);
s.eta = sol.y(Nsect+1:2*Nsect,:);
s.mu = sol.y(2*Nsect+1:3*Nsect,:);
%s.x = sol.y(3*Nsect+1:4*Nsect,:);
%s.y = sol.y(4*Nsect+1:5*Nsect,:);
s.theta = sol.y(5*Nsect+1:6*Nsect,:);

s.ss = [];
s.x = [];
s.y = [];
Lsum = 0;
for i = 1:Nsect
    s.ss = [s.ss Lsum+ L(i)*sol.x];
    s.x = [s.x L(i)*sol.y(3*Nsect+i,:)];
    s.y = [s.y L(i)*sol.y(4*Nsect+i,:)];
    Lsum = Lsum + L(i);
end

s.nu = s.nu(:);
s.eta = s.eta(:);
s.mu = s.mu(:);
%s.x = s.x(:);
%s.y = s.y(:);
s.theta = s.theta(:);
s.ss = s.ss';s.ss = s.ss(:);
t1=s.ss/sum(L)*2*pi;

sty = (s.y(end));
stx = (s.x(end));

st = (sqrt((stgx - Lsum)^2 + (stgy - 0)^2))/Lsum;
pos = [stgx,stgy,sg.theta(end)];

flag1=0;
if (flag1== 1)
    figure(1)
    hold on
    stt=2;
    plot(sg.x(1:stt:end),sg.y(1:stt:end));
    hold
    %patch([-1;-1;1;1],[-1;1; 1; -1],[0; 0; 0; 0],'g');
    %patch([-1;-1;1;1],[0; 0; 0; 0],[-1;1; 1; -1],'g');
    %patch(0.2*[-1;-1;1;1],0.2*[-1;1; 1; -1],[0; 0; 0; 0],'g');
    axis equal;

    figure(2)
    color1='b';
    color2 = 'r';
    subplot(2,3,1)
    hold on
    plot(sg.ss,sg.nu,color1)
    plot(s.ss,s.nu,color2)
    title('nu');
    subplot(2,3,2)
    hold on

```

```

    plot(sg.ss,sg.eta,color1)
    plot(s.ss,s.eta,color2)
    title('eta');
    subplot(2,3,3)
    hold on
    plot(sg.ss,sg.mu,color1)
    plot(s.ss,s.mu,color2)
    title('mu');
end

```

## A.2.2 Differential equations

```

function xdot = diffeqs2D(s,x,g,e,f,l,M,p,er,lr,pointld,gravangle,Nsect)
nu = x(1:Nsect,:);
eta = x(Nsect+1:2*Nsect,:);
mu = x(2*Nsect+1:3*Nsect,:);
theta = x(5*Nsect+1:6*Nsect,:);
f = f'*ones(1,size(theta,2));
e = e'*ones(1,size(theta,2));
g = g'*ones(1,size(theta,2));
l = l'*ones(1,size(theta,2));
p = p'*ones(1,size(theta,2));
fa = f.*sin(theta);
fb = f.*cos(theta);
nud = g.*mu.*eta -fa;
etad = -mu.*1./g.*(nu-1) - fb./g +mu.*p./e./g;
mud = e.*(1-g).*eta.*nu -e.*eta - l - p.*eta;
xd = nu.*cos(theta) - eta.*sin(theta);
yd = nu.*sin(theta)+eta.*cos(theta);
thetad = mu;
xdot=[nud;etad;mud;xd;yd;thetad];

```

## A.2.3 Boundary conditions

```

function res = allbcs2D(ya, yb,g,e,f,l,F,M,p,er,lr,gravangle)
g1 = g(1);g2 = g(2);g3 = g(3);
e1 = e(1);e2 = e(2);e3 = e(3);
l1 = l(1);l2 = l(2);l3 = l(3);
F1 = F(1);F2 = F(2);F3 = F(3);
M1 = M(1);M2 = M(2);M3 = M(3);
p1 = p(1);p2 = p(2);p3 = p(3);
res = [yb(1)-(ya(7)-1 - p2/e2)*er(1)-p1/e1-1-F1*sin(yb(6)+gravangle); ...
    yb(2)-ya(8)*g2*er(1)/g1 - F1*cos(yb(6)+gravangle)/g1; ...
    yb(3)-M1-(ya(9)-M2)*e1/e2*er(1)*lr(1); ...
    ya(4)-0; ...
    ya(5)-0; ...
    ya(6)-0;...
    yb(7)-(ya(13)-1 - p3/e3)*er(2)-p2/e2-1-F2*sin(yb(12)+gravangle); ...
    yb(8)-ya(14)*g3*er(2)/g2-F1*cos(yb(12)+gravangle)/g2; ...
    yb(9)-M2-(ya(15)-M3)*e2/e3*er(2)*lr(2); ...
    ya(10)-yb(4)/lr(1); ...
    ya(11)-yb(5)/lr(1); ...
    ya(12)-yb(6);...
    yb(13)-F3*sin(yb(18)+gravangle)-p3/e3-1; ...

```

```

    yb(14)-F3*cos(yb(18)+gravangle)/g3; ...
    yb(15)-M3; ...
    ya(16)-yb(10)/lr(2); ...
    ya(17)-yb(11)/lr(2); ...
    ya(18)-yb(12)];
res;

```

## A.3 Planar model

### A.3.1 Main script

```

options = bvpset('RelTol', 1e-4,'Nmax',100)
N=20;           %No. of points
EI = 9
GA = 2000
EA = 7500
f = 0.05
m = 0;
F = 1
M = 4
v1= [1 0 M/EI 0 0 0];
x1 = linspace(0,1,N);
solinit1 = bvpinit(x1,v1);
sol1 = bvp4c(@diffeqs2D,@allbcs2D,solinit1,options,EI,GA,EA,f,m,F,M)
plot(sol1.y(4,:),sol1.y(5,:));

```

### A.3.2 Differential equations

```

function xdot = diffeqs2D(s,Xa,EI,GA,EA,f,m,F,M)
nu = Xa(1);
eta = Xa(2);
mu = Xa(3);
x = Xa(4);
y = Xa(5);
theta = Xa(6);
g = GA/EA;
fa = f*sin(theta)/EA;
fb = f*cos(theta)/GA;
ga = GA/EI;
ea = EA/EI;
l = m/EI;
ei = EI/GA;
nud = g*mu*eta -fa;
etad = -ei*nu - fb;
mud = (ea-ga)*eta*nu - l;
xd = nu*cos(theta) - eta*sin(theta);
yd = nu*sin(theta)-eta*cos(theta);
thetad = mu;
xdot=[nud,etad,mud,xd,yd,thetad]';

```

### A.3.3 Boundary conditions

```
function res = allbcs2D(ya, yb,EI,GA,EA,f,m,F,M)
res = [(yb(1)-F*sin(yb(6))/EA), ...
      (yb(2)-F*cos(yb(6))/GA), ...
      (yb(3)-M/EI), ...
      (ya(4)-0), ...
      (ya(5)-0), ...
      (ya(6)-0)];
res = res';
```

## Test cases

This appendix presents results of design optimization for soft robotic manipulators under different constraints on the tube diameter.

### **B.1 Test case 1: Fixed overall diameter**

First we constrain the overall diameter of the manipulator so it can pass through openings of specified size. It can be seen that for same values of moment and stiffness, a three-tube section is the lightest. Hence, short manipulators tend to have three tubes in all sections. Since we use the same tube dimensions in all the sections, manipulators with only three-tube sections do not have any taper. For longer manipulators, the self-weight of the distal sections becomes a disadvantage. At a certain length, the optimal solution transitions from an all-three-tube solution to a solution with six tubes throughout except the distal section, which has three tubes. The distal section is always the

longest because it is required to be the most dexterous. In this case, the load capacity decreases with increasing manipulator length and decreasing number of sections (see Fig. B.3). The tube thickness increases with manipulator length, but there are downward jumps when transitions in section configuration occur. After a certain length, the manipulator is incapable of lifting its own weight.

## **B.2 Test case 2: Fixed tube diameter**

If the tube diameter, instead of the overall manipulator diameter is fixed, the actuating moment is maximized by having 12 tubes in each section. However, with increasing length, self-weight becomes important and 12-tube distal sections become unsupported. The optimal solution thus transitions first to a nine-tube distal section, and then to a six tube distal section. Eventually, more tapered solutions such as 12-9-6 and 12-9-9-3 are obtained. As before, tube thickness increases with length, but shows sudden downward jumps at configuration transitions. Load capacity decreases with length and increases with number of sections.

## **B.3 Test case 4: Fixed gripping radius**

Sometimes, it is desirable to fix the length of the distal section, in order to ensure that the manipulator is capable of gripping objects of a given size. For a given distal section length, the load capacity decreases with increasing number of sections. Also, the load

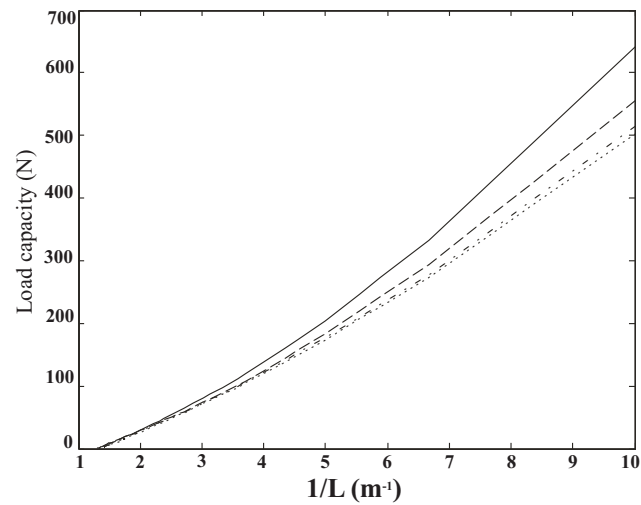


**Figure B.1.** Load capacity versus last section length for optimal hydraulic two section (solid), three section (dashed), four section (dash-dotted) and five section (dotted) arms.

capacity decreases with increasing distal section length (Figs. B.2 and B.1). Solutions with short lengths are not tapered, but with increasing length, the solutions become increasingly tapered.

## B.4 Test case 5: Compromised dexterity

In all these cases, the load capacity of the manipulators can be increased by compromising dexterity. For example, Fig. B.4 shows that by halving the dexterity requirement on the distal section for a fixed outer diameter case, we observe similar trends with increased load capacity.

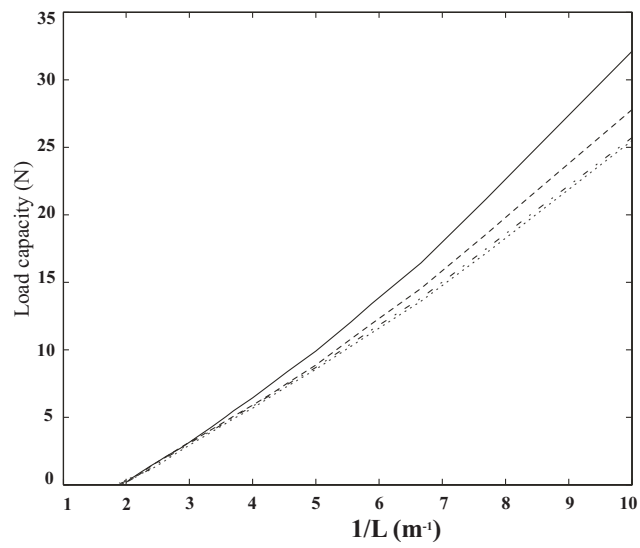


**Figure B.2.** Load capacity versus last section length for optimal pneumatic two section (solid), three section (dashed), four section (dash-dotted) and five section (dotted) arms.

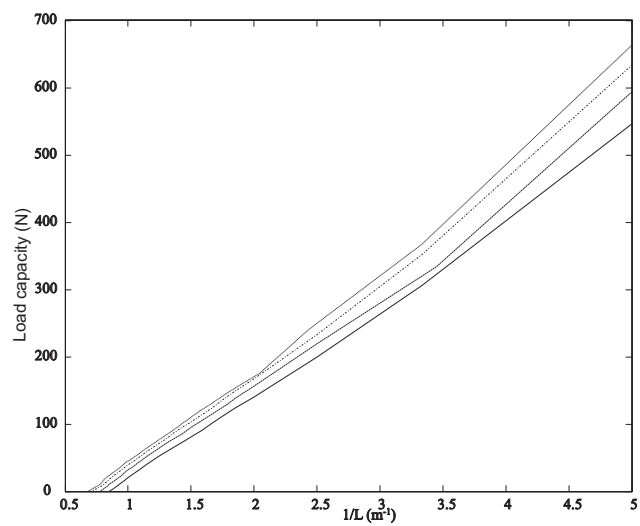


**Figure B.3.** Load capacity versus arm length for optimal hydraulic two section (solid), three section (dashed), four section (dash-dotted) and five section (dotted) arms for the case of fixed overall diameter.

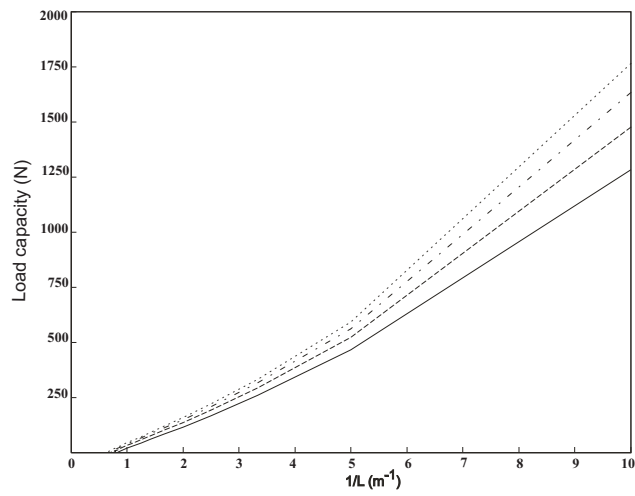


**Figure B.4.** Load capacity versus arm length for optimal hydraulic two section (solid), three section (dashed), four section (dash-dotted) and five section (dotted) arms for the case of fixed overall diameter, and a last section bending of 180 degrees.

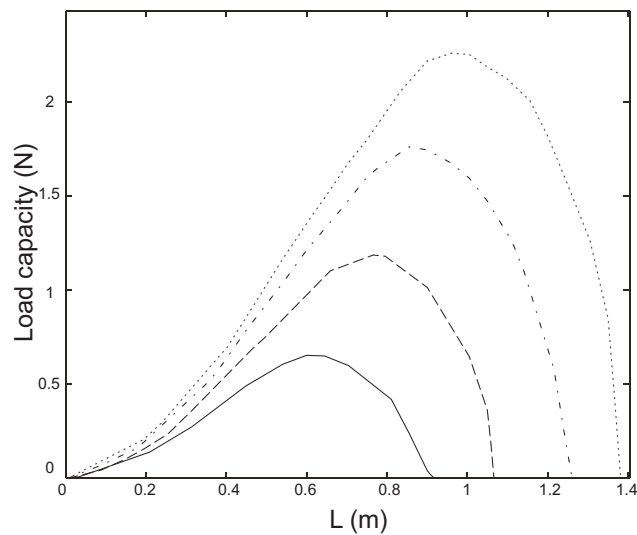


**Figure B.5.** Load capacity versus arm length for optimal pneumatic two section (solid), three section (dashed), four section (dash-dotted) and five section (dotted) arms for an overall diameter/length ratio of 0.09.

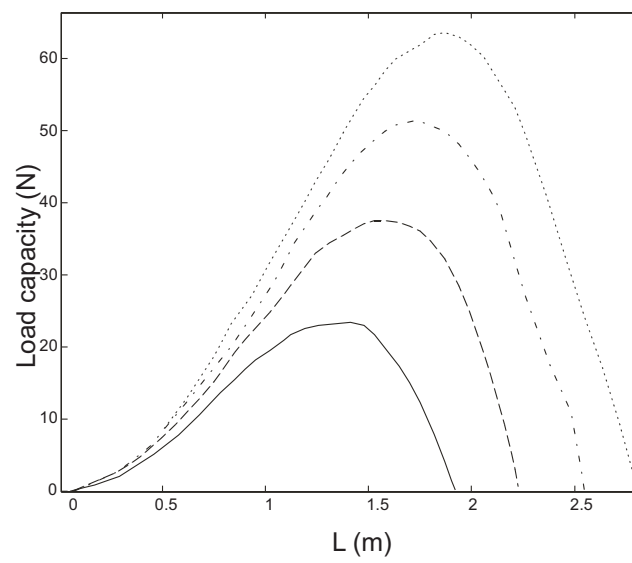


**Figure B.6.** Load capacity versus arm length for optimal hydraulic two section (solid), three section (dashed), four section (dash-dotted) and five section (dotted) arms for an overall diameter/length ratio of 0.09.

# Appendix C

## Constants

The constants  $\psi_i$  in Eqs. (5.2)-(5.3) are

$$\psi_1 = M_1 - \frac{\left( \begin{aligned} &((c_3 + c_1) F_{ib} M_2^2 + c_1 b_2) M_1^2 \times \\ &\quad \cos(\theta_0 + M_1 + M_2) \\ &+ b_2 M_1^2 M_2 (c_3 + c_1) \times \\ &\quad \sin(\theta_0 + M_1 + M_2) \\ &+ (-M_1^2 c_1 b_2 + b_1 M_2^2) \times \\ &\quad \cos(\theta_0 + M_1) \\ &+ (M_2^2 M_1 b_1 - M_1^2 M_2 b_2 c_3) \times \\ &\quad \sin(\theta_0 + M_1) \end{aligned} \right)}{M_1^2 M_2^2} \quad (\text{C.1})$$



where,

$$\frac{\partial \theta}{\partial p_i} = \begin{cases} \frac{\partial \theta_1}{\partial p_i} & \text{for section 1} \\ \frac{\partial \theta_2}{\partial p_i} & \text{for section 2} \end{cases} \quad (\text{C.7})$$

is obtained by differentiating Eqs. (5.2)-(5.3), yielding

$$\begin{aligned} \frac{\partial \theta_1}{\partial p_i} = & \frac{\partial \psi_1}{\partial p_i} + \frac{\partial \psi_2}{\partial p_i} \\ & + \frac{\sin(\theta_0 + M_1)}{M_1^3} \frac{\partial b_1}{\partial p_i} \\ & + b_1 \left( \begin{array}{c} \frac{\cos(\theta_0 + M_1)}{M_1^3} \\ -\frac{3(\sin(\theta_0 + M_1) - \sin \theta_0)}{M_1^4} \end{array} \right) \frac{\partial M_1}{\partial p_i} \end{aligned} \quad (\text{C.8})$$

and

$$\begin{aligned} \frac{\partial \theta_2}{\partial p_i} = & \frac{\partial \theta_1(1)}{\partial p_i} + \frac{\partial \psi_3}{\partial p_i} + \frac{\partial \psi_4}{\partial p_i} \\ & + M_2^{-3} \left( \begin{array}{c} \sin(\theta_0 + M_1 + M_2) \\ -\sin(\theta_0 + M_1) \end{array} \right) \frac{\partial b_1}{\partial p_i} \\ & + b_2 M_2^{-3} \left( \begin{array}{c} \cos(\theta_0 + M_1 + M_2) \\ -\cos(\theta_0 + M_1) \end{array} \right) \frac{\partial M_1}{\partial p_i} \\ & + b_2 M_2^{-4} \left( \begin{array}{c} -3 \sin(\theta_0 + M_1 + M_2) \\ +3 \sin(\theta_0 + M_1) \\ +M_2 \cos(\theta_0 + M_1 + M_2) \end{array} \right) \frac{\partial M_2}{\partial p_i} \end{aligned} \quad (\text{C.9})$$

The partial derivatives of the actuator moments with respect to the input pressures

are

$$\frac{\partial M_1}{\partial p_i} = EAR_o \left(1 + \frac{1}{\sin \frac{\pi}{3}}\right) \left(2 \frac{\partial \lambda_1}{\partial p_i} - \frac{\partial \lambda_2}{\partial p_i}\right) \quad (\text{C.10})$$

and

$$\frac{\partial M_2}{\partial p_i} = EAR_o \left(1 + \frac{1}{\sin \frac{\pi}{6}}\right) \left(2 \frac{\partial \lambda_3}{\partial p_i} - \frac{\partial \lambda_4}{\partial p_i}\right) \quad (\text{C.11})$$

The derivative of  $b_j$  is

$$\frac{\partial b_j}{\partial p_i} = -\frac{wa_j}{g_j} (g_j - 2) n_j \frac{\partial \lambda_k}{\partial p_i} \delta_{ij}. \quad (\text{C.12})$$

where  $n_j$  is the number of tubes in the control channel (2 or 4) and  $\delta_{ij}$  is the Kronecker delta. Finally, the sensitivity of actuator extension to pressure change is

$$\frac{\partial \lambda_j}{\partial p_i} = \frac{3/4 (\lambda_j \cos \alpha - 1)^3 \lambda_j^4 (\lambda_j \cos \alpha + 1)^3 \times (\lambda_j^2 (\cos \alpha)^2 - 1/3)^2 C_1^{-1} R_i^2 (R_i^2 - R_o^2)^{-1}}{\left( \begin{array}{l} (-7\lambda_j^6 + \lambda_j^{12}) \cos^{10} \alpha \\ + \left( -8/3 \lambda_j^{10} + \frac{55}{6} \lambda_j^4 \right) \cos^8 \alpha \\ + \left( 2 \lambda_j^8 + 4/3 \lambda_j^{10} \right. \\ \left. -7\lambda_j^6 - 4\lambda_j^2 - \frac{55}{3} \lambda_j^4 \right) \cos^6 \alpha \\ + \left( 1/2 + \frac{55}{6} \lambda_j^4 + 8\lambda_j^2 - \lambda_j^8 \right) \cos^4 \alpha \\ + \left( -1 - 1/3 \lambda_j^4 - 4\lambda_j^2 \right) \cos^2 \alpha \\ \left. + 1/6 \lambda_j^4 + 1/2 \right)} \delta_{ij} \quad (\text{C.13})$$

# Bibliography

- [1] OTAKE, M., Y. KAGAMI, M. INABA, and H. INOUE (2002) “Motion design of a starfish-shaped gel robot made of electro-active polymer gel,” *Robotics and Autonomous Systems*, **40**, pp. 185–191.
- [2] DIENNO, D. V. (2006) *Design and Analysis of a Soft Robotic Manipulator with Base Rotation*, Master’s thesis, The Pennsylvania State University.
- [3] CHAPMAN, G. (1958) “The hydrostatic skeleton in the invertebrates,” *Biological Reviews of the Cambridge Philosophical Society*, **33**, pp. 338–371.
- [4] ——— (1975) “Versatility of hydraulic systems,” *Journal of Experimental Zoology*, **194**, pp. 249–270.
- [5] CLARK, R. B. (1964) *Dynamics in Metazoan Evolution. The Origin of the Coelom and Segments*, Oxford: Clarendon Press.
- [6] GUTMANN, W. F. (1981) “Relationships between invertebrate phyla based on functional-mechanical analysis of the hydrostatic skeleton,” *American Zoologist*, **21**, pp. 63–81.

- [7] TAYLOR, J. R. A. and W. M. KIER (2003) "Switching skeletons: hydrostatic support in molting crabs," *Science*, **301**, pp. 209–210.
- [8] ——— (2006) "A pneumo-hydrostatic skeleton in land crabs," *Nature*, **440**, p. 1005.
- [9] WAINWRIGHT, S. A., F. VOSBURGH, and J. H. HEBRANK (1978) "Shark skin: function in locomotion," *Science*, **202**, pp. 747–749.
- [10] WAINWRIGHT, S. A. (1982) *Structural systems: hydrostats and frameworks. In Companion to Animal Physiology*, New York: Cambridge University Press.
- [11] ——— (1988) *Axis and Circumference*, Cambridge, MA: Harvard University Press.
- [12] CLARK, R. B. and J. B. COWEY (1958) "Factors controlling the change of shape of certain nemertean and turbellarian worms." *Journal of Experimental Zoology*, **35**, pp. 731–748.
- [13] HARRIS, J. E. and H. D. CROFTON (1957) "Structure and function in the nematodes: internal pressure and cuticular structure in *Ascaris*," *Journal of Experimental Biology*, **34**, pp. 116–130.
- [14] MCCURLEY, R. S. and W. M. KIER (1995) "The functional morphology of starfish tube feet: the role of a crossed-fiber helical array in movement," *Biological Bulletin*, **188**, pp. 197–209.
- [15] KIER, W. M. and K. K. SMITH (1985) "Tongues, tentacles, and trunks: the biomechanics of movement in muscular-hydrostats," *Zoological Journal of the Linnean Society*, **83**, pp. 307–324.

- [16] KIER, W. M. (1989) “The fin musculature of cuttlefish and squid (Mollusca, Cephalopoda): Morphology and mechanics.” *Journal of Zoology (London)*, **217**, pp. 23–38.
- [17] ——— (1987) *The functional morphology of the tentacle musculature of Nautilus pompilius*, Plenum Publishing Corporation.
- [18] KIER, W. M. and A. M. SMITH (1990) “The Morphology and Mechanics of Octopus Suckers,” *The Biological Bulletin*, **178**, pp. 126–136.
- [19] HERREL, A., J. J. MEYERS, P. AERTS, and K. C. NISHIKAWA (2001) “Functional implications of supercontracting muscle in the chameleon tongue retractors,” *The Journal of Experimental Biology*, **204**, pp. 3621–3627.
- [20] MEYERS, J. J., J. C. O’REILLY, J. A. MONROY, and K. C. NISHIKAWA (1999) “Mechanism of tongue protraction in microhylid frogs,” *The Journal of Experimental Biology*, **207**, pp. 21–31.
- [21] NAPADOW, V. J., R. D. KAMM, and R. J. GILBERT (2002) “A biomechanical model of sagittal tongue bending,” *Journal of Biomechanical Engineering*, **124**, pp. 547–556.
- [22] NISHIKAWA, K. C., W. M. KIER, and K. K. SMITH (1999) “Morphology and mechanics of tongue movement in the African pig-nosed frog *Hemissus marmoratum*: a muscular hydrostatic model,” *Journal of Experimental Biology*, **202**, pp. 771–780.
- [23] MEIJER, K., Y. BAR-COHEN, and R. J. FULL (2003) “Biological inspiration for musclelike actuators of Robots and Biologically Inspired Intelligent Robots,” *SPIE Press*, pp. 25–46.

- [24] HUNTER, I. W. and S. LAFONTAINE (1992) "Comparison of muscle with artificial actuators," *IEEE Solid-State Sensor and Actuator Workshop*, pp. 178–185.
- [25] KIER, W. M. and N. A. CURTIN (2002) "Fast muscle in squid (*Loligo pealei*): contractile properties of a specialized muscle fibre type," *The Journal of Experimental Biology*, **205**, pp. 1907–1916.
- [26] VAN LEEUWEN, J. and W. KIER (1997) "Functional design of tentacles in squid: linking sarcomere ultrastructure to gross morphological dynamics," *Philosophical Transactions of the Royal Society of London B: Biological Sciences*, **352**, pp. 551–571.
- [27] KIER, W. M. and J. T. THOMPSON (2003) "Muscle arrangement and function, and specialization in recent coleoids," *Berliner Palobiologische Abhandlungen*, **3**, pp. 141–162.
- [28] HETHERINGTON, A. (2001) "Guard cells," *Current Biology*, **11**(15), p. R588.
- [29] TAKAGI, S. (2002) "Actin-based photo-orientation movement of chloroplasts in plant cells," *Journal of Experimental Biology*, **206**, pp. 1963–1969.
- [30] HODICK, D. and A. SIEVERS (1989) "On the mechanism of trap closure of Venus flytrap (*Dionaea muscipula* Ellis)," *Planta*, **179**, pp. 32–42.
- [31] KANZAWA, N., Y. HOSHINO, M. CHIBA, D. HOSHINO, H. KOBAYASHI, N. KAMASAWA, Y. KISHI, M. OSUMI, M. SAMESHIMA, and T. TSUCHIYA (2006) "Change in the Actin Cytoskeleton during Seismonastic Movement of *Mimosa pudica*," *Plant Cell Physiology*, **47**, pp. 531–539.

- [32] OSTROWSKI, J. and J. BURDICK (1998) “The geometric mechanics of undulatory robotic locomotion,” *International Journal of Robotics Research*, **17**(7), pp. 683–701.
- [33] WRIGHT, C., A. JOHNSON, A. PECK, Z. MCCORD, A. NAAKTGEBOREN, P. GIANFORTONI, M. GONZALEZ-RIVERO, R. HATTON, and H. CHOSET (2007) “Design of a modular snake robot,” *Intelligent Robots and Systems, 2007. IROS 2007. IEEE/RSJ International Conference on*, pp. 2609–2614.
- [34] MILLER, G. (2007), “Snake Robots by Dr. Gavin Miller,” .  
URL [www.snakerobots.com](http://www.snakerobots.com)
- [35] ROBOTUNA (2001), “MIT Ocean Engineering, RoboTuna,” .  
URL <http://web.mit.edu/towtank/www/Tuna/tuna.html>
- [36] GEORGIADES, C., A. GERMAN, A. HOGUE, H. LID, C. PRAHACS, A. RIPS-  
MAN, R. SIMIT, L.-A. TOMSTI, P. ZHANGT, M. BUEHLER, G. DUDEK,  
M. JENKIN, and E. MILIOS (2004) “AQUA: an aquatic walking robot,” in *Proceedings of the 2005 IEEE International Conference on Intelligent Robots and Systems, Sendai, Japan*, pp. 3525–3531.
- [37] LIU, J., H. HU, and D. GU (2006) “A layered control architecture for autonomous robotic fish,” in *Proc. IEEE/RSJ Intl. Conf. on Intelligent Robots and Systems, Beijing, China, 9-15 October 2006*, pp. 312–317.
- [38] DENG, X. and S. AVADHANULA (2005) “Biomimetic Micro Underwater Vehicle with Oscillating Fin Propulsion: System Design and Force Measurement,” in *Proceedings of the 2005 IEEE International Conference on Robotics and Automation Barcelona, Spain, April 2005*, pp. 3312–3317.

- [39] CRESPI, A. and A. J. IJSPEERT (2006) “AmphiBot II: An amphibious snake robot that crawls and swims using a central pattern generator,” in *9th International Conference on Climbing and Walking Robots (CLAWAR 2006)*, pp. 19–27.
- [40] LACHAT, D., A. CRESPI, and A. J. IJSPEERT (2006) “Boxybot: a swimming and crawling fish robot controlled by a central pattern generator,” in *Proceedings of The first IEEE / RAS-EMBS International Conference on Biomedical Robotics and Biomechatronics (BioRob 2006)*, pp. 643–648.
- [41] GUO, S., T. FUKUDA, and K. ASAKA (2003) “A New Type of Fish-Like Underwater Microrobot,” *IEEE/ASME Trans. on Mechatronics*, **8**, pp. 136–141.
- [42] DAUGELA, A., H. F. C. E. JERONYMO, and A. MISAKI (1995) “Piezo Ceramic Based Locomotive Drive,” in *Sixth IEEE International Symposium on Micro Machine and Human Science*, pp. 187–192.
- [43] TAKANOBU, H., T. TANDAI, and H. MIURA (2004) “Multi-DOF Flexible Robot Based on Tongue,” in *IEEE International Conference on Robotics and Automation and New Orleans*, pp. 2673–2678.
- [44] CIESLAK, R. and A. MORECKI (1999) “Elephant trunk type elastic manipulator - a tool for bulk and liquid materials transportation,” *Robotica*, **17**, pp. 11–16.
- [45] HANNAN, M. and I. D. WALKER (2001) “Analysis and experiments with an elephant’s trunk robot,” *Advanced Robotics*, **15**, pp. 847–858.
- [46] SAMATHAM, R., K. KIM, D. DOGRUER, H. CHOI, M. KONYO, J. MADDEN, Y. NAKABO, J. NAM, J. SU, S. TADOKORO, W. YIM, and M. YAMAKITA (2007) *Electroactive Polymers for Robotic Applications, Chapter 1: Active Polymers: An Overview*, Springer, London.

- [47] BAR-COHEN, Y. (2000) “Electro-active polymers as artificial muscles — Capabilities, potentials and challenges,” *Handbook on Biomimetics*, Y. Osada, Ed. Peachtree City, GA: NTS Inc, **8**, p. 134.
- [48] MEIJER, K., M. ROSENTHAL, and R. J. FULL (2001) “Muscle-like actuators? A comparison between three electroactive polymers,” in *Proceedings of the SPIE - The International Society for Optical Engineering*, vol. 4329, pp. 7–15.
- [49] PELRINE, R., R. KORNBLUH, Q. PEI, S. STANFORD, S. OH, J. ECKERLE, R. FULL, M. ROSENTHAL, and K. MEIJER (2002) “Dielectric Elastomer Artificial Muscle Actuators: Toward Biomimetic Motion,” in *Smart Structures and Materials 2002: Electroactive Polymer Actuators and Devices (EAPAD) and Yoseph Bar-Cohen and Editor and Proceedings of SPIE*, vol. 4695, pp. 126–137.
- [50] ZHANG, X., C. LOWE, C. M. WISSLER, B. JAHNE, and G. KOVACS (2005) “Dielectric Elastomers in Actuator Technology,” *Advanced Engineering Materials*, **7**(5), pp. 361–367.
- [51] KORNBLUH, R., R. PELRINE, J. ECKERLE, and J. JOSEPH (1998) “Electrostrictive Polymer Artificial Muscle Actuators,” in *Proceedings of the 1998 IEEE International Conference on Robotics and Automation*, pp. 2147–2154.
- [52] ECKERLE, J., S. STANFORD, J. MARLOW, R. SCHMIDT, S. OH, T. LOW, and S. V. SHASTRI (2001) “Biologically inspired hexapedal robot using field-effect electroactive elastomer artificial muscles,” in *Smart Structures and Materials 2001: Industrial and Commercial Applications of Smart Structures Technologies*, Anna-Maria R. McGowan, Editor. *Proceedings of SPIE*, vol. 4332, pp. 269–280.
- [53] PEI, Q., R. PELRINE, M. ROSENTHAL, S. STANFORD, H. PRAHLAD, and R. KORNBLUH (2004) “Recent progress on electroelastomer artificial muscles

and their application for biomimetic robots,” in *Smart Structures and Materials 2004: Electroactive Polymer Actuators and Devices (EAPAD)*, edited by Yoseph Bar-Cohen, *Proceedings of SPIE*, vol. 5385, pp. 41–50.

- [54] JUNG, K., J. C. KOOI, J. DO NAM, Y. K. LEE, and H. R. CHOI (2007) “Artificial annelid robot driven by soft actuators,” *Bioinspiration and Biomimetics*, **2**, pp. S42–S49.
- [55] WINGERT, A., M. LICHTER, S. DUBOWSKY, and M. HAFEZ (2002) “Hyper-Redundant Robot Manipulators Actuated by Optimized Binary Dielectric Polymers,” in *Smart Structures and Materials 2002: Electroactive Polymer Actuators and Devices (EAPAD)*, Yoseph Bar-Cohen, Editor, *Proceedings of SPIE*, vol. 4695, pp. 415–423.
- [56] CORTÉS, M. T. and J. C. MORENO (2003) “Artificial muscles based on conducting polymers,” *e-Polymers 2003*, **41**, pp. 1–42.
- [57] NIE, L., D. LI, and S. GUO (2006) “Design and analysis of the dynamics of ICPF actuated tortoise-like lexible micro-robot,” in *Proceedings of SPIE - The International Society for Optical Engineering*, vol. 6357, pp. 6357571–6357576.
- [58] MICROMUSCLE (2007).  
URL [www.micromuscle.com](http://www.micromuscle.com)
- [59] ALICI, G. and N. N. HUYNH (2006) “A Robotic Gripper based on Conducting Polymer Actuators,” *AMC’06-Istanbul, Turkey*, pp. 472–477.
- [60] ——— (2007) “Performance Quantification of Conducting Polymer Actuators for Real Applications: A Microgripping System,” in *IEEE/ASME Transactions on Mechatronics*, vol. 12, pp. 73–84.

- [61] SHAHINPOOR, M., Y. BAR-COHEN, J. O. SIMPSON, and J. SMITH (1998) “Ionic polymer–metal composites (IPMCs) as biomimetic sensors and actuators and artificial muscles—a review,” *Smart Materials and Structures*, **7**, pp. R15–R30.
- [62] NAKABO, Y., T. MUKAI, and K. ASAKA (2005) “Kinematic Modeling and Visual Sensing of Multi-DOF Robot Manipulator with Patterned Artificial Muscle,” *Robotics and Automation, 2005. ICRA 2005. Proceedings of the 2005 IEEE International Conference on*, pp. 4315–4320.
- [63] SHAHINPOOR, M. and K. J. KIM (2001) “Ionic polymer–metal composites: I. Fundamentals,” *Smart Materials and Structures*, **10**, pp. 819–833.
- [64] ARENA, P., C. BONOMO, L. FORTUNA, M. FRASCA, and S. GRAZIANI (2006) “Design and Control of an IPMC Wormlike Robot,” *IEEE Transactions on Systems, Man, and Cybernetics — Part B: Cybernetics*, **36**(5), pp. 1044–1052.
- [65] PAK, N. N., S. SCAPELLATO, G. L. SPINA, G. PERNORIO, A. MENCIASSI, , and P. DARIO (2006) “Biomimetic Design of a Polychaete Robot Using IPMC Actuator,” in *Proceedings of the First International Conference on Biomedical Robotics and Biomechatronics*, vol. 1, pp. 666–671.
- [66] MOJARRAD, M. and M. SHAHINPOOR (1997) “Biomimetic robotic propulsion using polymeric artificial muscles,” *Proc. IEEE Int. Conf. on Robotics and Automation*, pp. 2152–2157.
- [67] KERREBROCK, P. A., J. M. ANDERSON, and J. R. PARRY (2001) “Application requirements of artificial muscles for swimming robots,” in *Proc. SPIE Vol. 4329, p. 364-374, Smart Structures and Materials 2001: Electroactive Polymer*

*Actuators and Devices, Yoseph Bar-Cohen; Ed. (Y. Bar-Cohen, ed.), vol. 4329 of Presented at the Society of Photo-Optical Instrumentation Engineers (SPIE) Conference, pp. 364–374.*

- [68] JUNG, J., Y. TAK, B. KIM, J.-O. PARK, S.-K. LEE, and J. PAK (2003) “Tadpole Robot (TadRob) using ionic polymer metal composite (IPMC) actuator,” in *Smart Structures and Materials 2003: Electroactive Polymer Actuators and Devices (EAPAD) and Proceedings of SPIE (Y. Bar-Cohen, ed.), vol. 5051, pp. 272–280.*
- [69] JALBERT, J., S. KASHIN, and J. AYERS (1995) “A biologically based undulatory lamprey-like AUV,” *Proc. of the Autonomous Vehicles in Mine Countermeasures Symposium*, pp. 39–52.
- [70] IJSPEERT, A. J. and J. KODJABACHIAN (1999) “Evolution and development of a central pattern generator for the swimming of a lamprey,” *Artificial Life*, **5**, p. 247.
- [71] KIM, B., J. RYU, Y. JEONG, Y. TAK, B. KIM, and J. O. PARK (2003) “A Ciliary Based 8-Legged Walking Micro Robot Using Cast IPMC Actuators,” in *Proceedings of the 2003 IEEE International Conference on Robotics and Automation, Taipei, Taiwan, September 2003.*
- [72] TADOKORO, S., S. YAMAGAMI, M. OZAWA, T. KIMURA, T. TAKAMORI, and K. OGURO (1999) “Multi-DOF device for soft micromanipulation consisting of soft gelactuator elements,” in *1999 IEEE International Conference on Robotics and Automation, Detroit, vol. 3, pp. 2177–2182.*
- [73] SHIGA, T., T., Y. HIROSE, A. OKADA, and T. KURAUCHI (1989) “Bending of ionic polymer gel caused by swelling under sinusoidally varying electric fields,” *Japanese Journal of Polymer Science and Technology*, **46**, p. 709.

- [74] TABATA, O., H. HIRASAWA, and S. AOKI (2001) “Ciliary motion on actuator using self-oscillating gel,” in *Proceedings of the IEEE Micro Electro Mechanical Systems (MEMS)*, pp. 405–408.
- [75] DAERDEN, F. and D. LEFEBER (2002) “Pneumatic Artificial Muscles: actuators for robotics and automation,” *European Journal of Mechanical and Environmental Engineering*, **47**(1), pp. 11–21.
- [76] KLUTE, G. K., J. M. CZERNIECKI, and B. HANNAFORD (1999) “McKibben artificial muscles: pneumatic actuators with biomechanical intelligence,” in *Proceedings of IEEE/ASME International Conference on Advanced Intelligent Mechatronics*, pp. 221–226.
- [77] YARLOTT, J. M. (1972) “Fluid actuator,” *US Patent No. 3645173*.
- [78] KUKOLJ, M. (1988) “Axially contractible actuator,” *US Patent No. 4733603*.
- [79] MORIN, A. H. (1953) “Elastic diaphragm,” *US Patent No. 2642091*.
- [80] PAYNTER, H. M. (1988) “High pressure fluid-driven tension actuators and methods for constructing them,” *US Patent No. 4751869*.
- [81] ——— (1988) “Hyperboloid of revolution fluid-driven tension actuators and methods of making,” *US Patent No. 4721030*, p. 1.
- [82] PRITTS, M. B. and C. D. RAHN (2004) “Design of an artificial muscle continuum robot,” in *Proceedings - IEEE International Conference on Robotics and Automation*, pp. 4742–4746.
- [83] IMMEGA, G. and K. ANTONELLI (1995) “The KSI Tentacle Manipulator,” in *IEEE International Conference on Robotics and Automation*, pp. 3149–3154.

- [84] SIMAAN, N., R. TAYLOR, and P. FLINT (2004) “Multi-DOF Flexible Robot Based on Tongue,” in *IEEE International Conference on Robotics and Automation and New Orleans*, pp. 351–357.
- [85] SUZUMORI, K., S. IIKURA, and H. TANAKA (1991) “Development of Flexible Microactuator and its application to Robotic Mechanisms,” in *IEEE International Conference on Robotics and Automation*, pp. 1622–1627.
- [86] WILSON, J. F., D. LI, Z. CHEN, and R. T. GEORGE (1993) “Flexible Robot Manipulators and Grippers: Relatives of Elephant Trunks and Squid Tentacles,” *Robots and Biological Systems: Toward a New Bionics?*, pp. 474–479.
- [87] TSUKAGOSHI, H., A. KITAGAWA, and M. SEGAWA (2001) “Active Hose: an Artificial Elephant’s Nose with Maneuverability for Rescue Operation,” in *IEEE International Conference on Robotics and Automation, Seoul and Korea*, pp. 2454–2459.
- [88] FESTO (2007), “Airacuda - The remote controlled, pneumatically driven fish,” .  
URL [http://www.festo.com/INetDomino/coorp\\\_sites/en/f1b00561e66a68b7c12571b9002b67c3.htm](http://www.festo.com/INetDomino/coorp\_sites/en/f1b00561e66a68b7c12571b9002b67c3.htm)
- [89] SUZUMORI, K., S. ENDO, T. KANDA, N. KATO, and H. SUZUKI (2007) “A Bending Pneumatic Rubber Actuator Realizing Soft-bodied Manta Swimming Robot,” in *IEEE International Conference on Robotics and Automation*, pp. 4975–4980.
- [90] SKIERCZYNSKI, B. A., R. J. A. WILSON, W. B. KRISTAN, and R. SKALAK (1996) “A model of the hydrostatic skeleton of the leech,” *Journal of Theoretical Biology*, **181**, pp. 329–342.

- [91] LIANG, Y., R. MCMEEKING, and A. EVANS (2006) “A finite element simulation scheme for biological muscular hydrostats,” *Journal of Theoretical Biology*, **242**, pp. 142–150.
- [92] YEKUTIELI, Y., R. SAGIV-ZOHAR, R. AHARONOV, Y. ENGEL, B. HOCHNER, and T. FLASH (2005) “Dynamic Model of the Octopus Arm. I. Biomechanics of the Octopus Reaching Movement,” *Journal of Neurophysiology*, **94**, pp. 1443–1458.
- [93] CHIEL, H. J., P. E. CRAGO, J. M. MANSOUR, and K. HATHI (1992) “Biomechanics of a muscular hydrostat: a model of lapping by a reptilian tongue,” *Biological Cybernetics*, **67**, pp. 403–415.
- [94] GERARD (2003) “A 3D biomechanical tongue model to simulate speech movements,” *Archives of Physiology and Biochemistry*, **111**, pp. 1381–3455.
- [95] TRIMMER, B., A. TAKESIAN, and B. SWEET (2006) “Caterpillar locomotion: A new model for soft-bodied climbing and burrowing robots,” in *7th International Symposium on Technology and the Mine Problem, Monterey, CA*.
- [96] WILSON, J. F., U. MAHAJAN, S. A. WAINWIRGHT, and L. J. CRONER (1991) “A continuum model of elephant trunks,” *Journal of Biomechanical Engineering*, **113**, pp. 79–84.
- [97] TRIVEDI, D., A. LOTFI, and C. D. RAHN (2007) “Geometrically exact dynamic models for soft robotic manipulators,” in *Proceedings of the 2007 IEEE International Conference on Intelligent Robots and Systems, San Diego*.

- [98] CHIRIKJIAN, G. S. (1993) “Continuum approach to hyper-redundant manipulator dynamics,” in *Proceedings of International Conference on Intelligent Robotic Systems*, pp. 1059–1066.
- [99] ——— (1995) “Hyper-redundant manipulator dynamics: a continuum approximation,” *Advanced Robotics*, **9**(3), pp. 217–243.
- [100] ——— (1997) “Inverse kinematics of binary manipulators using a continuum model,” *Journal of Intelligent and Robotic Systems: Theory and Applications*, **19**, pp. 5–22.
- [101] MOCHIYAMA, H. and T. SUZUKI (2003) “Kinematics and dynamics of a cable-like hyper-flexible manipulator,” in *Proceedings - IEEE International Conference on Robotics and Automation*, vol. 3, pp. 3672–3677.
- [102] MOCHIYAMA, H. and H. KOBAYASHI (1999) “The shape Jacobian of a manipulator with hyper degrees of freedom flexible manipulator,” in *Proceedings - IEEE International Conference on Robotics and Automation*, pp. 2837–2842.
- [103] ——— (1998) “Shape correspondence between a spatial curve and a manipulator with hyper degrees of freedom,” in *Proc. IEEE/RSJ Int. Conf. Intelligent Robots and Systems (IROS), Victoria, BC, Canada, Oct. 1998*, pp. 161–166.
- [104] HIROSE, S. (1993) *Biologically Inspired Robots*, Oxford University Press, pp. 147–155.
- [105] HANNAN, M. and I. D. WALKER (2000) “Analysis and initial experiments for a novel elephants trunk robot,” *Proc. Int. Conf. on Intelligent Robots and System (IROS)*, pp. 330–337.

- [106] ——— (2000) “Novel kinematics for continuum robots,” in *7th Int. Symp. Advances in Robot Kinematics*, pp. 227–238.
- [107] ——— (2003) “Kinematics and the implementation of an elephant’s trunk manipulator and other continuum style robots,” *Journal of Robotic Systems*, **20**, pp. 45–63.
- [108] GRAVAGNE, I. and I. D. WALKER (2000) “On the kinematics of remotely-actuated continuum robots,” in *Proceedings - IEEE International Conference on Robotics and Automation*, vol. 3, pp. 2544–2550.
- [109] JONES, B. A. and I. D. WALKER (2006) “Kinematics for multisection continuum robots,” *IEEE Transactions on Robotics*, **22**, pp. 43–55.
- [110] GRAVAGNE, I. A., C. D. RAHN, and I. D. WALKER (2003) “Large deflection dynamics and control for planar continuum robots,” *IEEE/ASME Transactions on Mechatronics*, **8**, pp. 299–307.
- [111] TATLICIOGLU, E., I. WALKER, and D. DAWSON (2007) “New Dynamic Models for Planar Extensible Continuum Robot Manipulators,” in *Proceedings of the 2007 IEEE International Conference on Intelligent Robots and Systems, San Diego*, pp. 1485–1490.
- [112] BOYER, F., M. POREZ, and W. KHALIL (2006) “Macro-continuous computed torque algorithm for a three-dimensional eel-like robot,” *IEEE Transactions on Robotics*, **22**, pp. 763–775.
- [113] RAJAMANI, A., M. GRISSOM, C. RAHN, Y. MA, and Q. ZHANG (2005) “Wound Roll Dielectric Elastomer Actuators: Fabrication and Analysis and Experiments,” *IEEE/RSJ International Conference on Intelligent Robots and Sys-*

- tems, 2005. (International Conference on Intelligent Robots and Systems 2005),* **2**, pp. 1520–1525.
- [114] MADDEN, J., N.GENEREUX, K. SHKURATOFF, A. V. D. STAR, D. POON, D. IRWIN, P. CHENG, G. HSU, and L. FILIPOZZI (2007) “Electroactive polymer actuator online database,” in *Proceedings of SPIE - The International Society for Optical Engineering*, p. 65240P.
- [115] SUMBRE, G., Y. GUTFREUND, G. FIORITO, T. FLASH, and B. HOCHNER (2001) “Control of octopus arm extension by a peripheral motor program.” *Science*, **293**, pp. 1845–1848.
- [116] GUTFREUND, Y., T. FLASH, Y. YAROM, G. FIORITO, I. SEGEV, and B. HOCHNER (1996) “Organization of octopus arm movements: a model system for studying the control of flexible arms.” *Journal of Neuroscience*, **16**, pp. 7297–7307.
- [117] SUMBRE, G., G. FIORITO, T. FLASH, and B. HOCHNER (2005) “Precise motor control of flexible arms.” *Nature*, **433**, pp. 595–596.
- [118] ——— (2005) “Octopuses Use a Human-like Strategy to Control Precise Point-to-Point Arm Movements,” *Current Biology*, **16**, pp. 767–772.
- [119] LAURENT, G. and E. PIAT (2001) “Efficiency of Swimming Microrobots using Ionic Polymer Metal Composite Actuators,” in *Proceedings of the 2001 IEEE International Conference on Robotics and Automation, Seoul, Korea*, vol. 4, pp. 3914–3919.

- [120] SFAKIOTAKIS, M., D. M. LANE, and J. B. C. DAVIES (1999) “Review of Fish Swimming Modes for Aquatic Locomotion,” *IEEE Journal of Oceanic Engineering*, **24**(2), pp. 237–252.
- [121] MCISAAC, K. and J. OSTROWSKI (2003) “Motion planning for anguilliform locomotion,” *Robotics and Automation, IEEE Transactions on*, **19**(4), pp. 637–652.
- [122] ESKIIZMIRLILER, S., N. FORESTIER, B. TONDU, and C. DARLOT (2002) “A model of the cerebellar pathways applied to the control of a single-joint robot arm actuated by McKibben artificial muscles,” *Biological Cybernetics*, **86**(5), pp. 379–394.
- [123] CHITRAKARAN, V. K., A. BEHAL, D. M. DAWSON, and I. D. WALKER (2007) “Setpoint regulation of continuum robots using a fixed camera,” *Robotica*, **25**, pp. 581–586.
- [124] HANNAN, M. and I. D. WALKER (2005) “Real-time shape estimation for continuum robots using vision,” *Robotica*, **23**, pp. 645–651.
- [125] GRAVAGNE, I. A. and I. D. WALKER (2000) “Kinematic transformations for remotely actuated planar continuum robots,” *IEEE International Conference on Intelligent Robots and Systems, San Francisco, CA*, pp. 19–26.
- [126] ——— (2004) “Manipulability and force ellipsoids for continuum robot manipulators,” *IEEE International Conference on Intelligent Robots and Systems*, pp. 304–311.

- [127] ——— (2002) “Uniform regulation of a multi-section continuum manipulator,” *IEEE International Conference on Intelligent Robots and Systems, San Francisco, CA*, pp. 1519–1524.
- [128] BRAGANZA, D., D. M. DAWSON, I. D. WALKER, and N. NATH (2006) “Neural Network Grasping Controller for Continuum Robots,” in *45th IEEE Conference on Decision and Control*, pp. 6445–6449.
- [129] GRAVAGNE, I. A., C. D. RAHN, and I. D. WALKER (2001) “Good Vibrations: A Vibration Damping Setpoint Controller for Continuum Robots,” in *Proceedings of the 2001 IEEE International Conference on Robotics & Automation, Seoul, Korea . May 21-26, 2001*, pp. 3877–3884.
- [130] ——— (2003) “Large deflection dynamics and control for planar continuum robots,” *IEEE/ASME Transactions on Mechatronics*, **8**, pp. 299–307.
- [131] OTAKE, M., Y. KAGAMI, Y. KUNIYOSHI, M. INABA, and H. INOUE (2003) “Inverse Dynamics of Gel Robots made of Electro-Active Polymer Gel,” in *IEEE International Conference on Robotics and Automation, Taipei, Taiwan.*, pp. 2299–2304.
- [132] TOLMAN, E. C. (1948) “Cognitive Maps in Rats and Man,” *Psychological Review*, **55**, pp. 189–208.
- [133] HOOPER, S. L. (2006) “Motor Control: The Importance of Stiffness,” *Current Biology*, **16**(8), pp. R283–R285.
- [134] FLASH, T. and T. SEJNOWSKI (2001) “Computational approaches to motor control.” *Current Opinion in Neurobiology*, **11**, pp. 655–662.

- [135] WOLPERT, D. and Z. GHAHRAMANI (2000) “Computational principles of movement neuroscience,” *Nature Neuroscience supplement*, **3**, pp. 1212–1217.
- [136] SABES, P. (2000) “The planning and control of reaching movements.” *Current Opinion in Neurobiology*, **10**, pp. 740–746.
- [137] CONRU, A. (1994) “A Genetic Approach to the Cable Harness Routing Problem,” *Proceedings of the IEEE World Congress on Computation Intelligence*, **1**, pp. 200–205.
- [138] HOLLEMAN, C., L. E. KAVRAKI, and J. WARREN (1998) “Planning paths for a flexible surface patch,” *IEEE Int. Conf. on Robotics and Automation*, **1**, pp. 21–26.
- [139] LAMIRAUX, F. and L. KAVRAKI (2001) “Path planning for elastic objects under manipulation constraints,” *International Journal of Robotics Research*, **20**(2), pp. 188–208.
- [140] GUIBAS, L., C. HOLLEMAN, and L. KAVRAKI (1999) “A probabilistic roadmap planner for flexible objects with a workspace medial-axis-based sampling approach,” *International Conference on Intelligent Robots and Systems*.
- [141] ANSHELEVICH, E., S. OWENS, F. LAMIRAUX, and L. E. KAVRAKI (2000) “Deformable Volumes in Path Planning Applications,” *International Conference on Robotics and Automation*, **3**, pp. 2290–2295.
- [142] BAYAZIT, O. B., H. LIEN, and N. AMATO (2002) “Probabilistic roadmap motion planning for deformable objects,” *International Conference on Robotics and Automation*, **2**, pp. 2126–2133.

- [143] GAYLE, M. LIN, and D. MANOCHA (2005) “Constraint-Based Motion Planning of Deformable Robots,” *IEEE Conf. on Robotics and Automation*, pp. 1046–1053.
- [144] GAYLE, R., P. SEGARS, M. LIN, and D. MANOCHA (2005) “Path Planning for Deformable Robots in Complex Environments,” *Robotics: Systems and Science*.
- [145] MOLL, M. and L. E. KAVRAKI (2006) “Path Planning for Deformable Linear Objects,” *IEEE Transactions on Robotics*, **22**(4), pp. 625–636.
- [146] TRIVEDI, D., D. DIENNO, and C. D. RAHN (2007) “Optimal, model-based design of soft robotic manipulators,” in *Proceedings of the 2007 ASME International Design Engineering Technical Conference, Las Vegas*.
- [147] CSENCITS, M., B. JONES, W. MCMAHAN, and I. WALKER (2005) “User interfaces for continuum robot arms,” in *Proc. IEEE/RSJ Intl. Conf. on Intelligent Robots and Systems, Edmonton, Canada*, pp. 3011–3018.
- [148] JEN, F., M. SHOHAM, and R. W. LONGMAN (1996) “Liapunov Stability of Force-Controlled Grasps with a Multi-Fingered Hand,” *International Journal of Robotics Research*, **15**, pp. 137–154.
- [149] ISMAEIL, O. M. and R. E. ELLIS (1994) “Grasping Using the Whole Finger,” *International Conference on Robotics and Automation*, **4**, pp. 3111–3116.
- [150] XIONG, C.-H., M. Y. WANG, Y. TANG, and Y.-L. XIONG (2005) “Grasping Matrix – Compliant Grasping with Passive Forces,” *Journal of Robotic Systems*, **22**, pp. 271–285.
- [151] FEARING, R. S. (1986) “Simplified grasping and manipulation with dextrous robot hands,” *IEEE J. Robot. Automation*, **2**, pp. 188–195.

- [152] BAKER, B. S., S. FORTUNE, and E. GROSSE (1985) “Stable prehension with a multi-fingered hand,” in *Proc. IEEE Int. Conf. Robotics and Automation, St. Louis*, pp. 570–575.
- [153] MARKENSCOFF, X., L. NI, and C. H. PAPADIMITRIOU (1990) “The geometry of grasping,” *Int. J. Robot. Res.*, **9**, pp. 61–74.
- [154] BICCHI, A. (1993) “Force distribution in multiple whole limb manipulation,” in *Proceedings of the IEEE International Conference on Robotics and Automation*, pp. 228–233.
- [155] SALISBURY, K., W. TOWNSEND, B. EBRMAN, and D. DIPIETRO (1988) “Preliminary design of a whole-arm manipulation system (WAMS),” *Robotics and Automation, 1988. Proceedings., 1988 IEEE International Conference on*, pp. 254–260 vol.1.
- [156] TONDU, B. and P. LOPEZ (2000) “Modeling and control of McKibben Artificial Muscle Robot Actuators,” *IEEE Control Systems Magazine*.
- [157] TSAGARAKIS, N. and D. G. CALDWELL (2000) “Improved modeling and assessment of pneumatic muscle actuators,” in *Proceedings - IEEE International Conference on Robotics and Automation*, vol. 4, pp. 3641–3646.
- [158] CHOU, C.-P. and B. HANNAFORD (1996) “Measurement and modeling of McKibben pneumatic artificial muscles,” *IEEE Transactions on Robotics and Automation*, **12**, pp. 90–103.
- [159] KLUTE, G. K. and B. HANNAFORD (1998) “Fatigue characteristics of McKibben artificial muscle actuators,” in *Proceedings of IEEE International Conference on Intelligent Robots and Systems*, vol. 3, pp. 1776–1781.

- [160] LIU, W. and C. D. RAHN (2003) “Fiber-reinforced membrane models of McKibben actuators,” *Journal of Applied Mechanics, Transactions ASME*, **70**, pp. 853–859.
- [161] SHAN, Y. and C. E. BAKIS (2006) “Flexible Matrix Composite Actuators,” in *Proc. 20th Technical Conference and American Soc. Composites*, DEStech Publications, Lancaster and PA, p. 20.
- [162] REESE, S., T. RAIBLE, and P. WRIGGERS (2001) “Finite element modeling of orthotropic material behaviour in pneumatic membranes,” *International Journal of Solids and Structures*, **38**, pp. 9525–9544.
- [163] BERTETTO, A. M. and M. RUGGIU (2004) “Characterization and modeling of air muscles,” *Mechanics Research Communications*, **31**, pp. 185–194.
- [164] JONES, B. and I. D. WALKER (2006) “Kinematics for Real-Time Implementation of Continuum Robots,” in *Proceedings of the 2006 IEEE International Conference on Robotics and Automation (ICRA), Orlando, FL*, pp. 1840–1847.
- [165] ANTMAN, S. S. (2004) *Nonlinear Problems of Elasticity*, Springer-Verlag, New York.
- [166] THOMAS, J. C. and C. WIELGOSZ (2004) “Deflections of highly inflated fabric tubes,” *Thin-Walled Structures*, **42**, pp. 1049–1066.
- [167] LELEU, S., H. ABOU-KANDIL, and Y. BONNASSIEUX (2001) “Piezoelectric actuators and sensors location for active control of flexible structures,” *Instrumentation and Measurement, IEEE Transactions on*, **50**(6), pp. 1577–1582.
- [168] LYSHEVSKI, S. (2003) “Data-intensive analysis and control of flexible pointing systems with PZT actuators,” *Frequency control symposium and pda exhibition*

*jointly with the 17th european frequency and time forum, 2003. proceedings of the 2003 ieee international*, pp. 948–956.

- [169] CAMARILLO, D., K. LOEWKE, C. CARLSON, and J. SALISBURY (2008) “Vision based 3-D shape sensing of flexible manipulators,” *Robotics and Automation, 2008. ICRA 2008. IEEE International Conference on*, pp. 2940–2947.
- [170] YI, X., J. QIAN, L. SHEN, Y. ZHANG, and Z. ZHANG (2007) “An Innovative 3D Colonoscope Shape Sensing Sensor Based on FBG Sensor Array,” *Information Acquisition, 2007. ICIA '07. International Conference on*, pp. 227–232.
- [171] MILLER, G. A., C. G. ASKINS, and E. J. FRIEBELE (2004) “Shape sensing using distributed fiber optic strain measurements,” *Second European Workshop on Optical Fibre Sensors, Proceedings of SPIE*, **5502**, pp. 528–531.
- [172] DUNCAN, R. G., M. E. FROGGATT, S. T. KREGER, R. J. SEELEY, D. K. GIFFORD, A. K. SANG, and M. S. WOLFE (2007) “High-Accuracy Fiber-Optic Shape Sensing,” *Sensor Systems and Networks: Phenomena, Technology, and Applications for NDE and Health Monitoring, Proc. of SPIE*, **6530**, pp. 576–587.
- [173] SAYEH, M. R., L. GUPTA, D. KAGARIS, R. VISWANATHAN, and B. CHUNG (2001) “Multiplexed fiber-optic strain sensors for distributed sensing,” *Proceedings of SPIE*, **4357**, pp. 125–129.
- [174] DAVIS, M. A., A. D. KERSEY, J. SIRKIS, and E. J. FRIEBELE (1996) “Shape and vibration mode sensing using a fiber optic Bragg grating array,” *Smart Materials and Structures*, **5**(6), pp. 759–765.
- [175] MARCUSE, D. (1976) “Curvature loss formula for optical fibers,” *J. Opt. Soc. Am.*, **66**(1), pp. 216–220.

- [176] TRIVEDI, D., A. LOTFI, and C. RAHN (2008) “Geometrically Exact Models for Soft Robotic Manipulators,” *Robotics, IEEE Transactions on*, **24**(4), pp. 773–780.
- [177] MATSUNO, T., T. FUKUDA, F. ARAI, and Y. HASEGAWA (2004) “Flexible Rope Manipulation Using Elastic Deformation Modeling by Dual Manipulator System with Vision Sensor,” *Journal of Robotics and Mechatronics*, **16**(1), pp. 31–38.
- [178] TRIVEDI, D., D. DIENNO, and C. D. RAHN (2008) “Optimal, Model-Based Design of Soft Robotic Manipulators,” *Journal of Mechanical Design*, **130**(9), p. 091402.
- [179] YOSHIKAWA, T. (1984) “Analysis and Control of Robot Manipulators with Redundancy,” in *Robotics Research, The first international symposium*, MIT Press, vol. 1, pp. 735–747.
- [180] KIM, J.-O. and K. KHOSLA (1991) “Dexterity measures for design and control of manipulators,” in *Intelligent Robots and Systems '91. 'Intelligence for Mechanical Systems, Proceedings IROS '91. IEEE/RSJ International Workshop on*, vol. 2, pp. 758–763.
- [181] TONDU, B., V. BOITIER, and P. LOPEZ (1994) “Naturally compliant robot-arms actuated by McKibben artificial muscles,” in *Proceedings of the IEEE International Conference on Systems and Man and Cybernetics*, vol. 3, pp. 2635–2640.
- [182] SIMO, J. C. and L. V. QUOC (1986) “On the dynamics in space of rods undergoing large motions – a geometrically exact approach,” *Computer methods in applied mechanics and engineering*, **66**, pp. 125–161.

- [183] SIMO, J. C. and L. VU-QUOC (1986) “A three-dimensional finite-strain rod model. part 2: computational aspects,” *Comp. Meth. Appl. Mech. Eng.*, **58**, pp. 79–116.
- [184] MCMAHAN, W., M. PRITTS, V. CHITRAKARA, D. DIENNO, B. J. B, M. GRIS-SOM, M. CSENCISITS, V. IYENGAR, I. D. WALKER, C. D. RAHN, and D. DAW-SON (2006) “Field Trials and Testing of the OctArm Continuum Manipulator,” *ICRA*, pp. 2336 – 2341.

# Vita

## Deepak Trivedi

### EDUCATION

- **August 2010** Ph. D in Mechanical Engineering with minor in Computational Science The Pennsylvania State University, University Park, PA
- **December 2007** M.S. in Mechanical Engineering The Pennsylvania State University, University Park, PA
- **May 2004** Bachelor of Technology in Mechanical Engineering, Indian Institute of Technology (IIT), Delhi, India.  
Exchange student at INSA de Lyon, France (Fall 2002, Spring 2003)

### RESEARCH INTERESTS

- My research interests include solid mechanics, structural dynamics, computational science, robotics, design and optimization.

### PROFESSIONAL EXPERIENCE

- Intern at Otis Elevator Company, Farmington, CT, Summer 2009
- Graduate Teaching Fellow at Penn State University, 2008-2009
- Intern at Bose Corporation, Framingham, MA, Summer 2008
- Graduate Research Assistant at Penn State University, 2005-2010
- Graduate Teaching Assistant at Penn State University, 2004-2007
- Intern at Aeronautical Development Establishment, Bangalore, Summer 2003
- Intern at IBM India Research Laboratory, Delhi, Summer 2002

### HONORS AND AWARDS

- Extra Mile Award (2009), Otis Worldwide Engineering Center
- Kulakowski Travel Award (2009), Penn State University.
- DAAD-Siemens Scholarship Program - Asia 21st Century (2004)
- Suresh Chandra Memorial Award(2004), Dechemical Engineering, IIT Delhi.
- Dean's certificate of merit for outstanding academic performance, 2001-2004, IIT Delhi.

### PUBLICATIONS

1. Trivedi D., Rahn C. D., "Shape sensing for soft robotic manipulators", ASME Int. Design Engineering Technical Conferences (Mechanisms and Robotics), 2009, San Diego.
2. Trivedi D., Rahn C. D., Kier W., Walker I.D., "Soft Robotics: Biological Inspiration, State of the Art, and Future Research", J. Applied Bionics and Biomechanics, 2008, Vol 5, No. 3, pp. 99-117.
3. Trivedi D., Dienno D., Rahn C.D., "Optimal Design of Soft Robotic Manipulators", ASME J. Mechanical Design, September 2008, Volume 130, Issue 9.
4. Trivedi D., Lotfi A., Rahn C.D., "Geometrically Exact Dynamics of Soft Robotic Manipulators", IEEE Journal of Robotics and Automation, Vol. 24, pp. 773-780, 2008.
5. Trivedi D., Dienno D., Rahn C.D., "Optimal, Model-based Design of Soft Robotic Manipulators", ASME Int. Design Engineering Technical Conferences, September 4-7, 2007, Las Vegas.
6. Trivedi D., Lotfi A., Rahn C.D., "Geometrically Exact Dynamic Models for Soft Robotic Manipulators", IEEE Int. Conference on Intelligent Robots and Systems, 2007, San Diego.
7. Basak J., Sudarshan A., Trivedi D., Santhanam M.S., "Weather Data Mining Using Independent Component Analysis", J. Machine Learning Research; MIT Press; 5(Mar):239-253, 2004.